Title

Improving the understanding of the spatiotemporal variability of hydrometeorology across the Sierra Nevada using a novel remote sensing reanalysis approach

Author

Huning, Laurie Susan

Publication Date

2017

Peer reviewed|Thesis/dissertation

UNIVERSITY OF CALIFORNIA

Los Angeles

Improving the understanding of the spatiotemporal variability of hydrometeorology across the Sierra Nevada using a novel remote sensing reanalysis approach

A dissertation submitted in partial satisfaction of the

requirements for the degree Doctor of Philosophy

in Civil Engineering

by

Laurie Susan Huning

2017

ABSTRACT OF THE DISSERTATION

Improving the understanding of the spatiotemporal variability of hydrometeorology across the Sierra Nevada using a novel remote sensing reanalysis approach

by

Laurie Susan Huning

Doctor of Philosophy in Civil Engineering

University of California, Los Angeles, 2017

Professor Steven Adam Margulis, Chair

While large populations worldwide depend on water derived from the seasonal snowpack, a detailed picture of the spatiotemporal variability of snowfall and snow water equivalent (SWE) across high-elevation mountain ranges remains a knowledge gap in understanding the hydrologic cycle. Previous studies relying on point-scale in situ measurements often yielded spatially incomplete characterizations of montane snow accumulation processes (e.g. orographic snowfall). These limitations were overcome in this dissertation by using a novel, high-resolution distributed snow reanalysis over Sierra Nevada, USA from 1985-2015. Across the 20 basins examined, over 50% of the integrated cumulative snowfall (CS) accumulated rapidly in less than or equal to six days or three snowstorms, on average, and the largest snowstorms yielded an average 27% of the seasonal CS. Results suggest that misrepresentation of a single snowstorm could lead to significant biases in CS. The hydroclimatology of the Sierra Nevada was found to be driven by extremes as manifested in the high inter-annual variability of

its seasonally-integrated CS, 4.4-41.3 km^3, over the record. Seasonal orographic CS gradients were shown to be highly variable, ranging from over 15 cm SWE/100 m to under 1 cm/100 m. Hence, the seasonal/elevational distribution of water storage can greatly vary with the western Sierra Nevada experiencing about twice as much orographic enhancement during wet years as in dry years. Among the largest winter snowstorms, moisture-rich atmospheric rivers (ARs) significantly contribute to the seasonal CS. Using both satellite-based integrated water vapor and reanalysis-based integrated vapor transport methods, AR-derived CS was found to be more orographically enhanced than non-AR derived CS above ~2200 m in the western Sierra Nevada; however, the understanding of the AR-derived CS distribution and enhancement is tightly coupled to the AR detection method applied. ARs were shown to contribute from ~33-56% of the seasonal CS, on average from 1998-2015, depending on the AR detection method utilized. Overall, more robust characterizations of the spatiotemporal variability and climatology of snowfall distributions, atmospheric drivers of snowfall, and accumulation rates than previously existed were provided. The resulting insight could be used for improving water resources management and hydrologic analysis as well as evaluating climate model snowpack estimates and improving their representation of subgrid snow processes (e.g. orographic snowfall).

The dissertation of Laurie Susan Huning is approved.

Dennis P. Lettenmaier

William W. Yeh

Yongkang Xue

Steven Adam Margulis, Committee Chair

University of California, Los Angeles

2017

To my family, for their never-ending support, encouragement, and wise words.

I will always be grateful.

Table of Contents

List of Figures

List of Tables

Acknowledgments

I am grateful for the continued support of my parents, Robert and Susan, who instilled a passion for knowledge and willingness to persevere with anything that I set out to accomplish. I am similarly indebted to my sister, Julie, and brother, Rob, who have always provided me with their wise words and have never failed to provide encouragement. Without the persistent support of my family, I would not be where I am today.

I would like to thank my advisor, Steve Margulis, who inspired me to pursue my graduate degrees. I am ever appreciative of the great insight, guidance, and mentorship he has shared with me throughout my studies at UCLA. I would also like to acknowledge my thesis committee members William Yeh, Dennis Lettenmaier, and Yongkang Xue for their guidance throughout my graduate studies. I would like to thank my good friends and colleagues as well as the many professors and teachers that have shared their knowledge with me along my journey.

I would also like to thank NASA for the financial support that they provided for this dissertation through the NASA Earth and Space Science Graduate Fellowship (NNX14AK75H). In addition, this dissertation was partially supported by the NASA NEWS Grant NNX15AD16G, NSF Grant EAR-1246473, and the NSF Blue Waters sustained petascale supercomputing project.

Laurie Susan Huning

EDUCATION

University of California, Los Angeles (UCLA) — **Los Angeles, CA**

Doctor of Philosophy in Civil Engineering — Expected June 2017
Master of Science in Civil Engineering — June 2011
Bachelor of Science in Civil Engineering, Summa Cum Laude — June 2009

Engineer-in-Training (EIT) — July 2008

PROFESSIONAL EXPERIENCE

- UCLA, Graduate Student Researcher — June 2011-Present
- UCLA, Teaching Assistant — September 2011-December 2015
    - Introduction to Hydrology (C&EE 150) — Fall 2015
    - Introduction to Hydrology (C&EE 150) — Fall 2014
    - Hydrologic Analysis and Design (C&EE 157L) — Spring 2013
    - Introduction to Hydrology (C&EE 150) — Fall 2012
    - Introduction to Water Resources Engineering (C&EE 151) — Winter 2012
    - Introduction to Hydrology (C&EE 150) — Fall 2011
- UCLA, Instructor — July 2013-August 2013
    - Differential and Integral Calculus (Calculus I) — Summer 2013
- Praad Geotechnical, Inc., Staff Engineer — February 2010-April 2011
- City of Los Angeles, Bureau of Engineering Intern — March 2008-September 2008

SELECTED HONORS, AWARDS, AND FELLOWSHIPS

- UCLA, Outstanding Doctor of Philosophy in Civil and Environmental Engineering Award — 2017
- UCSD Scripps Institution of Oceanography, 2016 International Atmospheric Rivers Conference Scholarship — 2016
- NASA, NASA Earth and Space Science Fellowship (NESSF) — 2014-Present
- UCLA, Charles F. Scott Fellowship — 2014-2016
- UCLA, UCLA Affiliates Fellowship — 2014-2015
- UCLA, Philip and Aida Siff Educational Foundation Fellowship — 2014-2015

REFEREED PUBLICATIONS

- Huning, L.S., S.A. Margulis, B. Guan, D.E. Waliser, and P.J. Neiman (2017), Implications of atmospheric river detection methods on characterizing their contribution to seasonal snowfall across the Sierra Nevada (USA), *Geophys. Res. Lett*., in review.
- Huning, L.S., and S.A. Margulis (2017), Investigating the spatiotemporal variability of high-elevation orographic snowfall enhancement and its drivers across Sierra Nevada, California, *J. Hydrometeor.*, in review.
- Huning, L.S., and S.A. Margulis (2017), Climatology of seasonal snowfall accumulation across the Sierra Nevada (USA): Accumulation rates, distributions, and variability, *Water Resour. Res.*, in review.
- Wrzesien, M.L., M.T. Durand, T.M. Pavelsky, I.M. Howat, S.A. Margulis, and L.S. Huning (2017), Comparison of methods to estimate snow water equivalent at the mountain range scale: A case study of the California Sierra Nevada, *J. Hydrometeor.*, 18, 1101-1119, doi:10.1175/JHM-D-16-0246.1.

- Margulis, S.A., G. Cortés, M. Girotto, L.S. Huning, D. Li, and M. Durand (2016), Characterizing the extreme 2015 snowpack deficit in the Sierra Nevada (USA) and the implications for drought recovery, *Geophys. Res. Lett.*, 43, 6341-6349, doi:10.1002/2016GL068520.
- Huning, L.S., and S.A. Margulis (2015), Watershed modeling applications with a modular physically-based and spatially-distributed watershed educational toolbox, *Environ. Modell. & Software*, 68, 55-69, doi:10.1016/j.envsoft.2015.02.008.

SELECTED CONFERENCE PAPERS AND INVITED TALKS

- Huning, L.S., S.A. Margulis, and P.J. Neiman (2017), Characterizing seasonal snowfall accumulation in the Sierra Nevada (USA): Inter-annual variability of snowstorms, atmospheric rivers, and orographic snowfall gradients, AMS 92nd Annual Meeting, 31st Conference on Hydrology, Seattle, WA, Jan. 22-26.
- Huning, L.S., S.A. Margulis, and P.J. Neiman (2016), Investigating the spatiotemporal variability of extreme orographic snowfall processes across Sierra Nevada, USA, Fall Meeting, AGU, San Francisco, CA, Dec. 12-16.
- Margulis, S.A., G. Cortés, M. Girotto, L.S. Huning, D. Li, and M. Durand (2016), Characterizing snowpack drought and drought recovery in the Sierra Nevada (USA), Fall Meeting, AGU, San Francisco, CA, Dec. 12-16.
- Huning, L.S., S.A. Margulis, and P.J. Neiman (2016), Investigating the climatological impact of atmospheric rivers on the Sierra Nevada (USA) seasonal snowpack, *2016 International Atmospheric Rivers Conference*, La Jolla, CA, Aug. 8-12.
- Girotto, M., S.A. Margulis, G. Cortés, L.S. Huning, D. Li, and M. Durand (2016), A Landsat-era (1985-2015) Sierra Nevada (USA) snow reanalysis dataset, *Eastern Snow Conference* (Invited), Columbus, OH, Jun. 14-16.
- Huning, L.S., S.A. Margulis, G. Cortés, M. Girotto, and M. Durand (2015), Spatiotemporal variability of orographic enhancement in the Sierra Nevada (USA): Results from a multi-decadal snow water equivalent reanalysis, Fall Meeting, AGU, San Francisco, CA, Dec. 14-18.
- Margulis, S.A., and L.S. Huning (2015), A coupled e-textbook and modular watershed model for hydrology education, *CUAHSI Virtual Workshop on Data-Driven Hydrology Education* (Invited), Sept. 8-29.
- Huning, L.S., and S.A. Margulis (2014), Watershed modeling applications with the open-access modular distributed watershed educational toolbox (MOD-WET) and introductory hydrology textbook, Fall Meeting, AGU, San Francisco, CA, Dec. 15-19.
- Huning, L.S., and S.A. Margulis (2013), Improving student comprehension of the interconnectivity of the hydrologic cycle with a novel "hydrology toolbox", integrated watershed model, and companion textbook, Fall Meeting, AGU, San Francisco, CA, Dec. 9-13.

DEVELOPER OF OPEN-ACCESS COMPUTER PROGRAM

- Huning, L.S., and S.A. Margulis (2016), MOdular Distributed Watershed Educational Toolbox (MOD-WET) User's Guide, 2016b Ed., 19 pp. and MOD-WET code available at http://aqua.seas.ucla.edu/margulis_intro_to_hydro_textbook.html.

Chapter 1: Introduction

1.1 Background and Motivation

With over one-sixth of the global population depending on seasonal snowmelt as their major source of water [*Barnett et al.,* 2005], hydrologically-significant snow-covered montane systems warrant further study. Large populations across the western United States greatly rely on snowmelt-derived streamflow from high-elevation basins for their water resources, especially during seasons with low amounts of precipitation [*Mote et al.,* 2005]. In particular, semiarid California, with a population approaching 40 million [*US Census Bureau,* 2017], derives over 60% of its developed water resources [*Downing,* 2015] and 75% of its water supply for agriculture from the Sierra Nevada [*Rosenthal and Dozier,* 1996].

Regions such as California that have a high dependence on seasonal snowmelt may be particularly susceptible to changes in the climate. For instance, studies have shown that the Sierra Nevada snowpack has shifted toward earlier melt with earlier peak streamflow due to a warming climate [*Mote et al.,* 2005; *Kapnick and Hall,* 2010]. Changes in the distribution and timing of snowfall, snowmelt, and streamflow have implications on water resources management and operational systems, which often rely on a combination of observations and model predictions to assess/forecast snowfall accumulation, snowpack size, and streamflow rates. An improved understanding of physical snow processes, snowfall distributions, and the variability of the montane snowpack at sub-seasonal, seasonal, and decadal scales would therefore have direct societal benefits.

Snow cover plays a critical role in both the water and energy budgets in many regions, impacting local and regional climate, atmospheric circulations, ecological systems, etc. In mountainous regions, snowfall or snow water equivalent (SWE) accumulates during the winter

and acts as a "water tower" [*Viviroli et al.,* 2007] that releases water as seasonal snowmelt in the spring. The montane snowpack accumulates from the combination of wintertime synoptic storms and orographic lifting. Simply described, as moist air is forced over a mountain barrier, it cools, water vapor condenses, clouds form, and orographic precipitation occurs along the windward side of a mountain. This can result in a rain shadow that yields distinct hydroclimatologies on the windward and leeward sides of a mountain range.

The snowfall that is delivered to the Sierra Nevada (Figure 1.1) each year is derived from relatively few snowstorms, leading to high inter-annual variability in snowfall and rapid accumulation rates across the range [*Serreze et al.,* 2001; *O'Hara et al.,* 2009; *Lundquist et al.,* 2015]. Among the storms that occur each season over the range, elongated moisture-rich low-level jets known as atmospheric rivers (ARs) are often among the largest [*Guan et al.*, 2010]. With their copious moisture and significant horizontal vapor transport, landfalling ARs promote orographic precipitation as they interact with mountainous terrain. Not only have ARs been estimated to yield ~30-40% of the total seasonal snowfall each winter in the Sierra Nevada [*Guan et al.,* 2010], but they are often associated with some of the most costly floods across California [e.g. *Ralph et al.,* 2006; *Dettinger et al.,* 2011].

1.2 Need for Detailed Distributed Snowfall Analysis and Existing Science Gaps

Though it is well-known that montane precipitation is highly variable, previous snowfall studies have often utilized point-scale measurements with relatively long temporal records, but incomplete spatial coverage [e.g. *Aguado,* 1990; *Dettinger et al.,* 2004; *Rutz and Steenburgh,* 2012; *Rutz et al.,* 2014; *Guan et al.,* 2012, 2016; *Lundquist et al.,* 2015]. Gridded datasets have been used to study montane snowfall over the Sierra Nevada [e.g. *Guan et al.,* 2010; *Kirchner et*

al., 2014], but were often relatively coarse (1 km or more) or were high-resolution, but temporally sparse. Global circulation models (GCMs) and regional climate models (RCMs) have also been utilized to simulate montane snow processes; however, they often severely smooth complex topography, resulting in poor representations of snowfall distributions and orographic processes across mountainous terrain [*Leung and Ghan,* 1995; *Cayan et al.,* 2008].

Conclusions drawn from montane studies are largely driven by the spatial scale used to represent the snowpack, whereby focusing on a limited spatial extent or coarsely sampling the snowpack may underestimate variability in highly heterogeneous complex terrain [*Clark et al.,* 2011]. Although the Sierra Nevada (Figure 1.1) is one of the most densely sampled mountain ranges across the globe [*Margulis et al.,* 2016], less than 1% of the range or about 1 in 700 km^2 is sampled by automated snow sensors [*Guan et al.,* 2013b]. Figure 1.1 shows the distribution of the in situ snow pillow sensors from the California Department of Water Resources (http://cdec.water.ca.gov/snow/current/snow/index.html), which were used for snowfall verification in Chapter 2. The large topographic variability (e.g. elevation, slope, and aspect) and heterogeneity of the surface conditions (e.g. roughness, vegetation, albedo, etc.) in complex mountainous areas can contribute to localized orographic effects and atmospheric circulations that result in highly variable precipitation patterns [*Dettinger et al.,* 2004; *Lundquist et al.,* 2010]. While synoptic atmospheric conditions often produce snowfall events, heterogeneous surface conditions and flow patterns impact snowfall accumulation, melt, and land-atmospheric feedbacks. Even through orographic snowfall/precipitation processes are known to be important in mountainous regions, many questions remain about the snowfall distribution (e.g. spatial/temporal/elevational), the cumulative snowfall (CS) volume, and snowfall variability at high-elevations across basins and entire mountain ranges [*Lehning,* 2013; *Kirchner et al.,* 2014].

While the source of the snowfall measurement itself was discussed above, it is also important to gain better insight into how a variety of sources of atmospheric information may influence the diagnosed contribution of specific meteorological events (e.g. ARs) to the seasonal snowfall. For instance, remote sensing and atmospheric reanalyses can each be used to diagnose when historic ARs occurred. However, since they utilize different physical variables and detection algorithms, questions exist about how an AR detection method may lead to differences in estimating AR contributions to orographic enhancement and the seasonal snowfall across a mountain range.

1.3 Science Questions

Although significant advancements continue to further the existing understanding of the seasonal snowpack accumulation in complex montane terrain, the following **overarching open science questions** motivate this dissertation:

- How is snowfall (depth and volume) distributed in space and time (e.g. inter-annually and climatologically) across a mountain range?
- To what extent do large-scale atmospheric features (e.g. moisture and wind fields) drive the orographic enhancement of snowfall across a mountain range?
- To what extent does the existing understanding of the importance of meteorological events to the seasonal snowfall distribution depend on the datasets and methodologies used to detect those events?

The primary thrust of this dissertation is to develop better physical insight into montane snow processes and snowfall distributions so that applications ranging from operational water resources management to regional climate modeling can ultimately be informed/improved from insight described herein. This work moves toward a more complete understanding of the

historical accumulation season, the reliability of snowfall estimates from a state-of-the-art snow reanalysis, and the sensitivity of AR-derived snowfall diagnoses to AR detection methods over the Sierra Nevada. To extend the current understanding of the spatiotemporal variability of snow processes (e.g. orographic snowfall) and states, this dissertation uses a novel, multi-decadal high-resolution distributed snow reanalysis over the Sierra Nevada [*Margulis et al.*, 2016] to yield better insight into snowfall distributions and climatology (Chapter 2), orographic enhancement processes (Chapter 3), and the importance of AR-derived snowfall (Chapter 4) than previously possible. One aim of the more comprehensive assessment of basin-scale to mountain range-scale processes provided herein is to fill the gap between the point-scale data-driven studies and the large-scale numerical studies with the use of the snow reanalysis across the major basins in the Sierra Nevada (Figure 1.1).

This dissertation is driven by the following **specific science questions**, which were grouped below by chapter. The primary aim of **Chapter 2** is to improve the characterization of the hydroclimatology of the Sierra Nevada by examining its snowfall distribution and accumulation rates to answer the following questions:

- What is the climatology (spatial/elevational/seasonal distribution and inter-annual variability) of snowfall events and the cumulative snowfall over the Sierra Nevada?
- When do the largest snowstorms occur during the accumulation season?
- What fraction of the seasonal cumulative snowfall do the largest snowstorms represent across the range?

Chapter 3 extends previous orographic analyses with the aim of better characterizing the inter-annual and spatial variability of orographically-driven snowfall gradients across the Sierra Nevada. The main thrust of this work is to answer:

- How is orographically-driven snowfall manifested across the windward (western) side of the Sierra Nevada?

In particular, this study also provides insight into the following:

- How can the shapes of the cumulative snowfall versus elevation curves be characterized (e.g. slope, maximum, etc.) and what factors influence their shapes?
- How and to what extent do orographic gradients vary spatially and inter-annually?
- What characterizes a "wet" versus "dry" year in the Sierra Nevada in terms of orographically-driven cumulative snowfall?

The overarching objective of **Chapter 4** is to better understand how diagnoses of ARs have hydrological implications by investigating:

- How does the selection of AR detection algorithms/methodologies, datasets, and physical quantities impact the understanding of snowfall processes and the relative importance of ARs across the Sierra Nevada?

Specifically, two AR catalogs were utilized to understand:

- How much snowfall is delivered to the Sierra Nevada during AR events (e.g. full snowfall volume, snowfall distribution, snowfall at high elevations, etc.)?
- Are there differences in orographic enhancement between AR and non-AR driven elevational snowfall distributions?

Improvements in the existing understanding of snowfall distributions, snowstorm contributions to snowfall, and inter-annual and climatic variability will not only yield valuable insight into unanswered questions and complement previous studies, but it will also generate historical databases of snowfall information for use in a variety of applications (e.g. informing water resources management/policy, model improvement/development for climate models, etc.).

1.4 Organization of Dissertation

This dissertation is organized into five chapters. **Chapter 2** verifies the distributed snowfall dataset utilized throughout this dissertation against in situ snow pillow observations. It also provides a detailed climatology of the snowfall distribution, accumulation rates, and snowfall variability across the Sierra Nevada. Chapter 2 provides the foundation for investigating storm-driven orographic cumulative snowfall gradients in **Chapter 3**. In Chapter 3, atmospheric drivers of wintertime orographic snowfall (e.g. moisture and wind fields) are examined across the mountain range during broadly defined snowstorm events. **Chapter 4** characterizes snowfall distributions derived from a specific type of storm (i.e. an atmospheric river) across the Sierra Nevada in the winter. This chapter provides insight into how the existing understanding of the importance of ARs to the seasonal snowfall in the Sierra Nevada is connected to the detection method that is used to diagnose these synoptic features. **Chapter 5** summarizes the originality of this dissertation and its key findings. It also provides insight into future work as an extension of this dissertation.

1.5 Figures

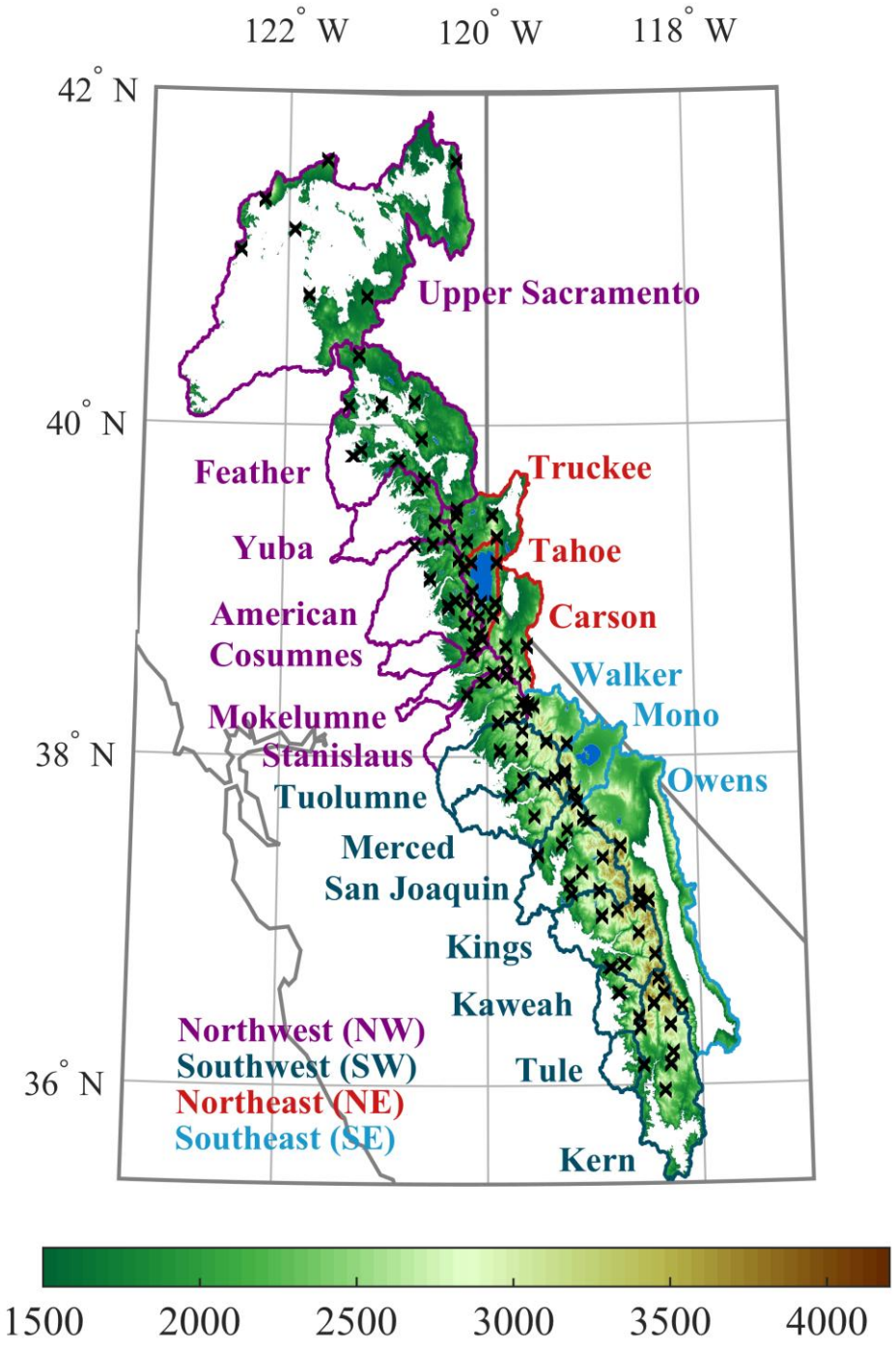

Figure 1.1. Distribution of elevation (in meters) across the Sierra Nevada above 1500 m. Twenty major watersheds analyzed herein are outlined. Snow pillow locations are demarcated by the '×' symbols.

1.6 Bibliography

Aguado, E. (1990), Elevational and latitudinal patterns of snow accumulation departures from normal in the Sierra Nevada, *Theor. Appl. Climatol.*, 42, 177-185.

Barnett, T. P., J. C. Adam, and D. P. Lettenmaier (2005), Potential impacts of a warming climate on water availability in snow-dominated regions, *Nature*, 438, 303-309, doi:10.1038/nature04141.

Cayan, D. R., E. P. Mauere, M. D. Dettinger, M. Tyree, and K. Hayhoe (2008), Climate change scenarios for the California region, *Climatic Change*, 87, S21-S42.

Clark, M. P., J. Hendrikx, A. G. Slater, D. Kavetski, B. Anderson, N. J. Cullen, T. Kerr, E. Ö. Hreinsson, and R. A. Woods (2011), Representing spatial variability of snow water equivalent in hydrologic and land-surface models: A review, *Water Resour. Res.*, 47, W07539, doi:10.1029/2011WR010745.

Dettinger, M. D., F. M. Ralph, T. Das, P. J. Neiman, and D. R. Cayan (2011), Atmospheric rivers, floods and the water resources of California, *Water*, 3, 445-478, doi:10.3390/w3020445.

Dettinger, M. D., K. Redmond, and D. Cayan (2004), Winter orographic precipitation ratios in the Sierra Nevada – Large-scale atmospheric circulations and hydrologic consequences, *J. Hydrometeor.*, 5, 1102-1116.

Downing, J. (2015), Forest thinning may increase water yield from the Sierra Nevada, *Calif. Agr.*, 69(1), 10-11.

Guan, B., N. P. Molotch, D. E. Waliser, E. J. Fetzer, and P. J. Neiman (2013a), The 2010/2011 snow season in California's Sierra Nevada: Role of atmospheric rivers and modes of large-scale variability, *Water Resour. Res.*, 49, 6731-6743, doi:10.1002/wrcr.20537.

Guan, B., N. P. Molotch, D. E. Waliser, E. J. Fetzer, and P. J. Neiman (2010), Extreme snowfall events linked to atmospheric rivers and surface air temperature via satellite measurements, *Geophys. Res. Lett.*, 37, L20401, doi:10.1029/2010GL044696.

Guan, B., N. P. Molotch, D. E. Waliser, S. M. Jepsen, T. H. Painter, and J. Dozier (2013b), Snow water equivalent in the Sierra Nevada: Blending snow sensor observations with snowmelt model simulations, *Water Resour. Res.*, 49, 5029-5046, doi:10.1002/wrcr.20387.

Guan, B., D. E. Waliser, N. P. Molotch, E. J. Fetzer, and P. J. Neiman (2012), Does the Madden-Julian Oscillation influence wintertime atmospheric rivers and snowpack in the Sierra Nevada? *Mon. Wea. Rev.*, 140, 325–342, doi: 10.1175/MWR-D-11-00087.1.

Guan, B., D. E. Waliser, F. M. Ralph, E. J. Fetzer, and P. J. Neiman (2016), Hydrometeorological characteristics of rain-on-snow events associated with atmospheric rivers, *Geophys. Res. Lett.*, doi:10.1002/2016GL067978.

Kapnick, S., and A. Hall (2010), Observed climate-snowpack relationships in California and their implications for the future, *J. Climate*, 23, 3446-3456, doi:10.1175/2010JCLI2903.1.

Kirchner, P. B., R. C. Bales, N. P. Molotch, J. Flanagan, and Q. Guo (2014), LiDAR measurement of seasonal snow accumulation along an elevation gradient in the southern Sierra Nevada, California, *Hydrol. Earth Syst. Sc.*, 18, 4261-4275, doi:10.5194/hess-18-4261-2014.

Lehning, M. (2013), Snow-atmosphere interactions and hydrological consequences, *Adv. Water Resour.*, 55, 1-3, doi:10.1016/j.advwatres.2013.02.001.

Leung, L. R., and S. J. Ghan (1995), Subgrid parameterization of orographic precipitation, *Theoretical and Applied Climatology*, 52, 95-118.

Lundquist, J., M. Hughes, B. Henn, E. Gutmann, B. Livenh, J. Dozier, and P. Neiman (2015), High-elevation precipitation patterns: Using snow measurements to assess daily gridded

datasets across the Sierra Nevada, California, *J. Hydrometeor.*, 16, 1773-1792 doi:10.1175/JHM-D-15-0019.1.

Lundquist, J. D., J. R. Minder, P. J. Neiman, E. Sukovich (2010), Relationships between barrier jet heights, orographic precipitation gradients, and streamflow in the Northern Sierra Nevada, *J. Hydrometeor.*, 11, 1141-1156, doi:10.1175/2010JHM1264.1.

Margulis, S., G. Cortés, M. Girotto, and M. Durand (2016), A Landsat-era Sierra Nevada (USA) snow reanalysis (1985-2015), *J. Hydrometeor.*, 17, 1203-1221, doi:10.1175/JHM-D-15-0177.1.

Mote, P. W., A. F. Hamlet, M. P. Clark, and D. Lettenmaier (2005), Declining mountain snowpack in Western North American, *Bull. Amer. Meteor. Soc.*, 86(1), 39-49, doi:10.1175/BAMS-86-1-39.

O'Hara, B. F., M. L. Kaplan, and S. J. Underwood (2009), Synoptic climatology analyses of extreme snowfalls in the Sierra Nevada, *Wea. Forecasting*, 24, 1610-1624, doi:10.1175/2009WAF2222249.1.

Ralph, F. M., P. J. Neiman, G. A. Wick, S. I. Gutman, M. D. Dettinger, D. R. Cayan, and A. B. White (2006), Flooding on California's Russian River: Role of atmospheric rivers, *Geophys. Res. Lett.*, 33, L13801, doi:10.1029/2006GL026689.

Rosenthal, W., and J. Dozier (1996), Automated mapping of montane snow cover at subpixel resolution from the Landsat Thematic Mapper, *Water Resour. Res.*, 32, 115-130, doi:10.1029/95WR02718.

Rutz, J. J., and W. J. Steenburgh (2012), Quantifying the role of atmospheric rivers in the interior western United States, *Atmos. Sci. Lett.*, 13, 257-261, doi:10.1002/asl.392.

Rutz, J. J., W. J. Steenburgh, and F. M. Ralph (2014), Climatological characteristics of atmospheric rivers and their inland penetration over the Western United States, *Mon. Wea. Rev.*, 142, 905-921, doi:10.1175/MWR-D-13-00168.1.

Serreze, M. C., M. P. Clark, and A. Frei (2001), Characteristics of large snowfall events in the montane western United States as examined using snowpack telemetry (SNOTEL) data, *Water Resour. Res.*, 37(3), 675-688.

United States Census Bureau (2017), *California QuickFacts from the US Census Bureau*, Accessed 4 May 2017, http://www.census.gov/quickfacts/table/PST045216/06,00.

Viviroli, D., H. H. Dürr, B. Messerli, M. Meybeck, and R. Weingartner (2007), Mountains of the world, water towers for humanity: Typology, mapping, and global significance, *Water Resour. Res.*, 43, W07447, doi:10.1029/2006WR005653.

Chapter 2: Climatology of Seasonal Snowfall Accumulation across the Sierra Nevada (USA): Accumulation Rates, Distributions, and Variability

2.1 Introduction

The western USA relies heavily on melt-derived streamflow from high-elevation basins especially during seasons of minimal precipitation [*Mote et al.,* 2005]. In particular, over 60% of the developed water resources [*Bales et al.,* 2011; *Downing,* 2015] and 75% of the agricultural water supply [*Rosenthal and Dozier,* 1996] across California are derived from the Sierra Nevada. Montane snowfall or snow water equivalent (SWE) accumulates from the combination of wintertime synoptic storms and orographic lifting. As SWE accumulates it acts as a reservoir, which releases water in the spring as air temperature and solar radiation increase and drive melt. With the high variability of the topography and surface characteristics in mountainous terrain, orographic effects and atmospheric circulation features contribute to significant variability in the spatial patterns of precipitation/snowfall accumulation across a range [*Dettinger et al.,* 2004; *Lundquist et al.,* 2010; *Huning and Margulis,* in review, hereafter *HM17*].

Since snowfall accumulation is highly variable across a mountain range, it is important to develop detailed insight into its distribution and accumulation rate. Previously *O'Hara et al.* [2009] presented a snowstorm climatology over the Sierra Nevada focusing on the atmospheric synoptic features that deliver snow to the range. The climatology characterized herein however is presented from a land surface perspective that focuses on the rate of snowfall accumulation and its distribution. Prior studies analyzing the accumulation rate of snowfall across the Sierra Nevada [*Serreze et al.,* 2001; *Lundquist et al.,* 2015] have shown that this range receives its

annual snowfall during an exceptionally short time period relative to other ranges in the western USA. However, such studies have generally relied on point-scale in situ measurements and were therefore unable to capture the full spatiotemporal variability of snowfall distributions across the range. While it is well-known that snowfall is highly variable in time and space, limited high-resolution spatially-distributed datasets have generally inhibited our ability to quantify the climatological rate of snowfall accumulation across an entire mountain range. Using distributed information, we aim to bridge the existing gap between spatially incomplete point-scale studies and large-scale numerical model-based studies that are often too coarse to adequately resolve important sub-grid processes during the accumulation season.

Recently there has been an increase in the number of snow studies that utilized spatially-distributed SWE datasets to quantify the peak SWE, 1 April SWE, or SWE melt volumes [e.g. *Dozier*, 2011; *Rice et al.*, 2011; *Dozier et al.*, 2016; *Margulis et al.*, 2016a and 2016b, hereafter *M16a* and *M16b*, respectively; etc.] as well as elevational distributions of SWE and cumulative snowfall (CS) during the accumulation season [e.g. *Kirchner et al.*, 2014; *HM17*]. These studies however did not focus on quantifying the CS volume, where CS is defined herein as the integrated amount of storm-driven snowfall accumulated throughout the accumulation season, nor on the rate of snowfall accumulation across this range. Nonetheless, they showed the added value of spatially continuous snow information over sparse point-scale observations. It is important to emphasize that CS is a temporally integrated quantity that indicates accumulated increases in SWE, while the amount of SWE present on the ground on a specific day t (e.g. 1 April) includes the net accumulation minus ablation. Hence, $CS(t) \geq SWE(t)$.

Questions still remain about the climatological rate of snowfall accumulation and its inter-annual variability across entire mountain ranges and individual basins. Thus, the primary thrust of this paper is to provide a more detailed characterization of the snowfall distribution and

the seasonality of large snowstorms (i.e. timing, magnitude, and duration) and their contributions to the wintertime CS than currently exists across the Sierra Nevada. Quantifying these factors is crucial for better managing water resources, hydropower, etc. This paper aims to answer the following questions: 1) What is the climatology (spatial/elevational/seasonal distribution and inter-annual variability) of snowfall events and the cumulative snowfall over the Sierra Nevada? 2) When do the largest snowstorms occur during the accumulation season? 3) What fraction of the seasonal cumulative snowfall do the largest snowstorms represent across the range? Using a spatially and temporally continuous SWE dataset [*M16a*] we provide more robust estimates of snowfall distributions at the basin and range scales, which have not been possible in previous studies over a mountain range, as well as additional insight into accumulation rates that complements existing literature.

2.2 Study Domain, Data, and Methods

2.2.1 Study Domain

The Sierra Nevada (Figure A.1) was subdivided into four geographic regions: northwest (NW), southwest (SW), northeast (NE), and southeast (SE) to elucidate the distinct precipitation regimes of the northern vs. southern and eastern vs. western Sierra Nevada. The subdivisions also help account for fluctuations in the storm track that contribute to regional snowfall variability across the 20 major watersheds in the range (Figure A.1a). The NW and SW Sierra Nevada each consist of seven basins, while the NE and SE regions each consist of three basins. In addition to the western (windward) basins, the Owens and Mono basins in the eastern Sierra Nevada also provide snowmelt-derived water to Southern California.

All analysis was performed above 1500 m, which typically represents the lowest elevation that is seasonally snow-covered (i.e. average snow line) [*Rice et al.,* 2011; *Guan et al.,*

2013], for land pixels shown in Figure A.1a. Above 1500 m, the average elevation across the Sierra Nevada is ~2200 m and the 20 basins examined herein span nearly 50,000 km^2. The northern Sierra Nevada has lower elevations than the southern basins (Figure A.1b) and the eastern basins have steeper slopes than the western basins. A strong rain shadow results in more forested areas on the western side of the range than on the eastern side with higher elevations being less vegetated. This range exhibits a maritime snowpack regime, which is characterized by the shortest accumulation seasons in the western USA [*Trujillo and Molotch,* 2014]. Traditionally, 1 April is taken to be the time of peak SWE; however, as *M16a* demonstrated, this assumption can lead to significant underestimation of the pixel-wise and basin-average peak SWE due to terrain variability, the timing of snowstorms, etc.

2.2.2 Snowfall Datasets

2.2.2.1 Sierra Nevada SWE Reanalysis

Without additional information or methods, snowfall volumes cannot be estimated directly from point-scale in situ observations. Depending on the size of the domain, density of measurements, complexity of the topography, etc., combining point-scale measurements with statistical methods can yield large errors in stored water [*Dozier et al.,* 2016]. Moreover, these observations cannot capture the detailed spatiotemporal variability of snowfall across mountainous terrain that is useful for water resources and hydrological applications. These limitations were overcome by characterizing the snowfall accumulation and identifying snowstorms over the Sierra Nevada using the 90-m gridded, daily SWE reanalysis from *M16a*.

The 90-m SWE reanalysis (Section A.2) was used herein to derive CS fields during 31 accumulation seasons spanning water years (WYs; 1 October-30 September) 1985-2015. The accumulation season was defined from November to the basin-average day-of-peak (DOP) SWE

and therefore varies inter-annually. The SWE dataset was previously utilized to investigate pixel-wise peak SWE [*M16a*] and range-wide peak SWE [*M16b*]. Herein, we used it to analyze the basin-average CS and investigate snowstorms and snowfall accumulation rates. CS was similarly used by *HM17*; however, they focused on characterizing seasonal orographically-driven CS and associated atmospheric synoptic features.

2.2.2.2 Snow Pillow Observations

M16a validated the posterior estimates of peak SWE against in situ observations across the Sierra Nevada. Since herein we investigate snowfall accumulation as opposed to peak SWE, we verified CS information derived from the SWE reanalysis (i.e. the posterior). The comparison was performed relative to over 100 snow pillows in the Sierra Nevada from the California Department of Water Resources Data Exchange Center (CDEC; http://cdec.water.ca.gov/snow/current/snow/index.html) over WYs 1985-2015. After performing quality control (described in Section B.3), over 3000 station years went into the daily median CS comparison and nearly 2700 station years were available for the seasonal CS verification (described below).

Not only do the snow pillow observations differ in spatial resolution relative to the 90-m snowfall dataset, but they do not adequately sample all elevations and physiographic conditions across the range because they are typically confined to low/mid-elevations located in cleared, flat terrain. In addition, <1% of the snow-dominated Sierra Nevada is sampled by this relatively "dense" snow pillow network [*Guan et al.,* 2013; *M16a*]. Nonetheless, these in situ observations provide a means for independently verifying SWE and snowfall estimates across the range since they were not used in the assimilation framework.

2.2.3 Wet and Dry Year Classification

While our primary focus is on the 31-year climatology, we also classified a subset of years as wet or dry based on the total integrated CS anomalies as a percent difference relative to the 31-year average. We identified wet and dry years as those with percent differences >20% and <-20%, respectively, following *M16a*. These distinctions promote a better understanding of inter-annual variability and thereby the differences among wet-year, dry-year, and long-term (31-year) climatologies of snowstorms, snowfall rates, and CS patterns. Herein, wet years include WYs 1986, 1993, 1995, 1998, 2005, 2006, 2008, and 2011 and dry years include WYs 1987, 1988, 1990, 1992, 1994, 2001, 2007, and 2012-2015. For consistency, these years were defined for the entire range and therefore are not basin-specific.

2.2.4 Snowstorm Definition and Metrics

To fully leverage the distributed nature of the snowfall (S) information, we developed a snowstorm definition based on the CS volume and applied it to each basin. The definition (as discussed below and depicted in Figure 2.1) differs from previous techniques that identified snowstorms of a given duration (e.g. 3-day or 5-day events, *Serreze et al.*, 2001, *Lundquist et al.*, 2015) and those that required a given fraction of stations to register a specified amount of snowfall [e.g. *O'Hara et al.,* 2009]. Instead we used daily increases in SWE, $S = \Delta SWE > 0$, at the highest elevations (elevations above the 75th-percentile of a basin or EL_{75}, Figure A.1b) as an indicator to define when basin-wide snowstorms occurred. A basin-relative elevation, rather than a fixed one, prevented basins from having a disproportionate number of pixels used to identify snowstorms (relative to other basins). These elevations were used because the largest snowstorms typically occur at the highest elevations and extend downslope with fluctuations in

the snow line. Using the daily increases in snowfall from pixels in the top quartile of the basin, the daily-integrated snowfall volume (V) was computed as follows:

$$V(t) = \Delta x \Delta y \sum_{i=1}^{N} S_i(t), \text{ for } \Delta SWE_i(t) > 0 \quad (2.1)$$

where the daily increase in SWE (i.e. snowfall) was computed for all pixels i above EL_{75} and N is the total number of pixels above EL_{75} within a basin. Each pixel has a uniform horizontal resolution (i.e. $\Delta x = \Delta y = 90\,\text{m}$). As shown in Figure 2.1a, only days contributing ≥1% of the seasonally-integrated CS volume at these elevations (V_{Tot}) were further considered (i.e. $V(t) \geq 0.01 V_{Tot}$), where V_{Tot} is given by:

$$V_{Tot} = \sum_{t=1\,Nov}^{DOP} V(t) \quad (2.2)$$

Consecutive days satisfying the above criterion were grouped into a single snowstorm "event". An event therefore can consist of a series of sequential days or a single day (shaded regions in Figure 2.1). The 1% threshold was defined to capture the largest snowfall events. It prevents negligible CS increases across a basin from being identified as an unrealistically long or continuous event. Integrating the CS accumulated only during snowstorms results in ≤100% of the seasonal CS as observable in Figure 2.1. During years when the snowstorm-derived CS was <100% of the seasonal CS, the remaining CS accumulated during small and/or localized snowfall events (Figure 2.1). The 1% threshold is conservative given that an estimated 10 snowstorms occur annually in the Sierra Nevada [*O'Hara et al.,* 2009], meaning that on average with everything equal, one snowstorm contributes 10% of the seasonal CS. After events were identified, further analysis was generalized to the entire basin to determine CS storm totals (numerals in Figure 2.1a). It is important to make the distinction that herein snowfall and CS were quantified in units of equivalent water depth, rather than snow depth.

In the Sierra Nevada, previous studies have shown that the largest or "leading" snowstorm is often an atmospheric river (AR) and provides a significant fraction of the CS [e.g. *Serreze et al.*, 2001; *Guan et al.*, 2010]. Although ARs (long, narrow low-level jets with high moisture and high horizontal vapor transport) deliver an average of 30-40% of the seasonal CS in the Sierra Nevada [*Guan et al.*, 2010], herein we investigate snowstorms including ARs, frontal systems, etc., but in a more general framework. Using in situ Snowpack Telemetry (SNOTEL) measurements, *Serreze et al.* [2001] estimated that the leading (3-day) snowstorm of a season yielded an average 17% of the total CS. Therefore to examine the contribution of the largest snowstorm using distributed data across the range, we defined a basin-wide leading event for a given year as the snowstorm that yielded the largest total integrated CS volume over the basin that year (Figure 2.1a). While storm events were quantified basin-wise, "storm snow days" were quantified pixel-wise during each event to capture the spatial heterogeneity in CS accumulation rates. A storm snow day (SSD) was defined for a specific pixel if $S_i = \Delta SWE_i > 0$ on a given storm day (i.e. for each pixel, days with increases in CS within shaded snowstorm periods in Figure 2.1b). Hence, the maximum possible number of $SSDs$ during a snowstorm would correspond to the total snowstorm duration. The size of a snowstorm was defined as the average increase in CS that the basin or pixel experienced during the event.

We quantified the seasonal snowfall accumulation rate with two approaches: 1) chronological and 2) ranked. During each season the chronological approach characterizes the rate of accumulation in a time-dependent, sequential daily manner (i.e. calendar days, CDs, or the day of the accumulation season starting 1 November), while the ranked method requires sorting and ranking the snowstorm data. Snowstorms were ranked based on their integrated CS from the leading storm to the smallest identified snowstorm volumes. $SSDs$ were similarly

sorted for each pixel and arranged in descending order based on (daily) $S_i(t) = \Delta SWE_i(t) > 0$. The ranking approach highlights how the largest events yield the greatest contribution to the CS, whereas the chronological approach provides information on the seasonality of events. They yield complementary insight into the seasonal accumulation rate and the length of the season itself. The number of CDs or $SSDs$ to accumulate at least p percent of the CS is denoted with a subscript (e.g. CD_p, where $p = 50$ corresponds to the number of CDs to accumulate $\geq 0.5CS$).

2.3 Verification, Results, and Discussion

2.3.1 CS Verification

Figure 2.2 compares the median CS time series between the snow pillows (observed, red) and the snowfall dataset (estimated, blue) across the pillow stations in the Sierra Nevada for the 31 study years. The median CS time series was constructed by taking the median of the individual station CS time series each year. If a consistent set of sensors existed throughout the season, the median CS time series would not exhibit any decreases. However, since a variable number of sensors resulted from missing data, the median CS curve can decrease (e.g. WY 1989) although the individual station time series monotonically increase.

Although the SWE reanalysis was generated to improve seasonal estimates of SWE, concurrent increases in the median CS estimated and observed time series in Figure 2.2 indicate that the snowfall dataset represents the timing of the observed snowfall events well. This is manifested in the strong positive correlations ($r \geq 0.97$, $p = 0.00$) between the two time series each year. The majority of years in Figure 2.2 exhibit relatively small differences between the daily observed and estimated CS. The time series show increases of comparable magnitudes particularly when large events are observed. This is further demonstrated in Figure 2.2 (bottom right), which shows that the estimated daily CS values from each of the 31 median CS time

series have a low root-mean-square error (RMSE) of 5 cm and mean error (ME) or bias of -3 cm relative to the observations. A negative ME value indicates that the snowfall dataset underestimates CS relative to observations. Although the two curves track one another during WYs such as 1998-1999 and 2012-2015, they exhibit larger biases throughout the majority of the accumulation season and increase the RMSE and ME values. Nonetheless, the RMSE and ME are relatively low as CS differences can be accumulated over the course of a season.

To further evaluate the SWE reanalysis as a snowfall dataset, the seasonally-integrated CS was examined at individual stations and at a larger scale with the median in Figure 2.3. Note that in situ observations were available in all basins except Cosumnes. As shown in Figure 2.3, the observed and estimated (reanalysis) CS values are strongly correlated with statistically significant correlation coefficients ranging from 0.90-0.98 across all watersheds. Due to scale disparities, it is expected that the CS observations ("point-scale" or ~3 m × 3 m) will vary from the estimates (90 m × 90 m). Differences are expected to be the largest at the individual station scale because snow pillows are generally located in flat clearings, while forest cover may be included in the 90-m pixel. Moreover, the pillows are subject to localized wind-blown snow that may not be represented at the 90-m scale. Hence, the grid-averaged 90-m reanalysis pixels should not be expected to represent the same values as observed at the pillows.

Considering all stations and years for each of the basins in Figure 2.3, the RMSE and ME range from 7 cm to 20 cm and from -1 cm to -16 cm, respectively. When all individual years and stations are considered ('o' symbols, bottom right), the RMSE and ME are 12 cm and -4 cm, respectively. These values are larger than the RMSE and ME of the median across all stations for each year ('+' symbols, bottom right), which are 4 cm and -2 cm, respectively. The RMSE and ME associated with the seasonal median CS computed over all years for each station ('×' symbols, bottom right) is also low (8 cm and -4 cm, respectively).

While a comparison of CS at the station-level is presented in Figure 2.3, the analysis utilizing the median across all stations provides a more robust comparison. The station analysis is subject to more spatial variability, resulting in higher RMSE and ME values. Despite the limitations in the SWE reanalysis (described in Section A.2, e.g. fixed rain-snow partitioning air temperature) and the inherent disparities between 90-m CS estimates and point-scale snow pillow observations, we find that the estimated snowfall dataset is capable of representing snowfall timing and snowstorm magnitudes. This is evidenced by the reanalysis-derived CS exhibiting strong positive correlation coefficients, low RMSE, and low ME values when compared to observations.

Note that for the verifications above, 1 April was taken as the end of the season for consistency with previous snowfall studies. However, for the snowfall analysis presented hereafter, the end of the accumulation season was taken to be the basin-average DOP SWE.

2.3.2 CS Distribution and Volume

Prior to analyzing snowstorms and rates of CS accumulation, it is worthwhile to develop an understanding of the climatology of the CS spatial distribution and its inter-annual variability across the range (as shown in Figure 2.4). Moreover, the amount of CS has not been thoroughly documented over the range due to limitations in data as well as the general emphasis of high-elevation snow studies to focus on SWE volumes at a given time [e.g. *Dozier,* 2011; *M16a-b*], instead of CS over the accumulation season. Across all three climatological CS maps in Figure 2.4a, the western basins accumulate a larger fraction of the CS than the eastern basins. The size of the rain shadow varies inter-annually with greater spillover onto the leeward (eastern) side observed during wet years (middle) than dry (right) years. Overall, higher elevations receive more CS than lower elevations, which was similarly demonstrated by the orographic CS quantified in *HM17*.

As the differences among the maps in Figure 2.4a suggest, there is substantial inter-annual variability in the CS depth (Figure 2.4b) across the range. The wet-year and dry-year average integrated CS are 35.0 km^3 and 13.0 km^3, respectively. The large difference in values is nearly equal to the 31-year average integrated CS, which illustrates the high variability of the hydroclimatology that exists across the Sierra Nevada. Similar to precipitation totals across California [*Dettinger et al.,* 2011; *Dettinger and Cayan,* 2014; *Dettinger,* 2016], the CS over the Sierra Nevada is often a story of extreme wet and dry years as shown in Figure 2.4. Across basins in Figure 2.4b, the CS depth ranges from an average 0.17 m (Tule) to 0.87 m (Yuba) with standard deviations of 0.34 m and 0.12 m, respectively. The high inter-annual variability that occurs across the 20 basins is reflected by the standard deviations for each basin representing 38.8-55.2% of their respective 31-year mean values. The range (Figure 2.4b, bottom row) has an average CS of 0.46 m with a standard deviation of 0.19 m (41.8% of mean). This corresponds to a 31-year average integrated CS volume of ~22.4 km^3 and a standard deviation of 9.4 km^3 at the range-scale. The large standard deviations further emphasize that the hydroclimate of the Sierra Nevada does not have a "normal" state; rather, it is dictated by extreme conditions.

As shown in Figure 2.4b, the integrated CS ranged from 0.09 m (or 4.4 km^3) in WY 2015 (19.7% of the 31-year average) amidst an exceptionally severe drought [*M16b*] to 0.85 m (or 41.3 km^3) in WY 1993 (184.7% of the 31-year average). The 31-year average CS, which intentionally excludes accumulation season melt, serves as a complement to the 31-year average estimates of pixel-wise peak SWE and range-wide peak SWE volumes of 20.0 km^3 [*M16a*] and 18.6 km^3 [*M16b*], respectively. Even with varying definitions of the accumulation season, the 31-year basin-average CS volume is larger than the SWE volumes estimated by *M16a-b*.

2.3.3 Range-scale Characteristics of Snowstorms and Storm Snow Days

On average, an estimated 11 snowstorms occur annually in the Sierra Nevada (Figure 2.5a) with an average of nine and thirteen events during dry (red) and wet (blue) years, respectively. Hence, dry years generally have approximately four fewer storms than wet years. As illustrated in Figure 2.5a, the average number of events ranged from about seven snowstorms in WY 2015 to more than double that (~16 snowstorms) in WYs 2002 and 2006. The average number of *SSDs* (Figure 2.5b) is ~21 days/year, with ~17 and 24 *SSDs* occurring on average during dry and wet years, respectively. As shown in Figure 2.5b, the average number of *SSDs* was the lowest in WY 2015 (driest in Figure 2.4b) with only about nine *SSDs*. In contrast, WY 1993 (wettest in Figure 2.4b) had the highest number of *SSDs* with ~30 (over three times as many as in 2015). Seven out of eight wet years (~88%) correspond to years with cool November-March range-wide air temperature anomalies, while eight out of eleven dry years (~73%) are associated with warm anomalies relative to the 31-year mean.

2.3.3.1 Descriptors of Integrated CS

Unlike the number of snowstorms, the number of *SSDs* more clearly differentiates the wettest and driest years over this record. In fact, the average number of *SSDs* explains ~70% of the variance in the integrated CS over the Sierra Nevada, while the average number of snowstorms per year explains only ~43% of the variance. Thus, the total number of *SSDs* (which represents the cumulative snowstorm duration) over a season, rather than the number of events, is a better indicator of whether a year will yield higher (or lower) snowfall accumulation over the range (i.e. a wet vs. dry year). This is demonstrated in Figure 2.5c, which depicts the relationships between the integrated CS and the average number of snowstorms (left) and *SSDs*

(right) each year. The relationship between CS and snowstorms (left) shows greater scatter (i.e. weaker relationships) than observed between CS and $SSDs$ (right).

Estimates of the integrated CS volume over the entire range serve as an important step in improving water resources management. While it is often difficult to estimate CS at high resolutions as done herein, it is generally more feasible to estimate the average number of $SSDs$ and/or snowstorms that occur across the range during a given year. Therefore, regression models were developed to estimate the integrated CS (in km^3) from the number of snowstorms (SS):

$$CS = 2.045SS \tag{2.3}$$

and the number of storm snow days (SSD):

$$CS = 0.045SSD^2 + 0.115SSD \tag{2.4}$$

as shown in Figure 2.5c in purple. Higher order polynomials and other functional forms exhibited a negligible gain in performance over the linear model (Eq. (2.3), left panel in Figure 2.5c) and its coefficient of determination ($R^2 = 0.43$) when SS was utilized as the predictor of CS. However, the quadratic model in Eq. (2.4) (Figure 2.5c, right) showed improvement over a linear fit for the CS-SSD data when comparing the sum of squared errors/residuals. The quadratic model explains ~72% of the observed variability in CS. These models could serve as valuable tools for water managers and hydrologic applications since they provide new methods for estimating the seasonally-integrated CS from more easily estimated quantities. They improve upon and complement traditional methods that simply rely on estimates of the 1 April SWE to indicate whether a given season was wetter or drier than average. Previous studies have shown that relying on 1 April SWE as a measure of peak SWE can introduce biases [*Montoya et al.*, 2014; *M16a*].

2.3.3.2 Distributions of Snowstorms, SSDs, and Leading Snowstorms

Both the average number of snowstorms per basin (not shown) and *SSDs* (Figure 2.6) are larger along the western slope than the eastern slope of the mountain range for the 31-year, wet-year, and dry-year averages. This coincides with higher CS across the western basins (Figure 2.4a), which results from the roughly perpendicular orientation of the terrain to the prevailing winds that promotes orographically-driven CS enhancement [*Grubišić et al.,* 2005; *HM17*]. As the snowstorms rise over the range, they may dissipate before (or while) descending the leeward side of the range resulting in lower CS and fewer *SSDs*. Synoptic features such as higher zonal wind speed at 700 hPa and larger vapor transport enhance CS gradients across the western basins during wet years [*HM17*], leading to the overall increase in CS across elevations as seen in Figure 2.4a.

While the number of snowstorms does not vary within a basin like *SSDs*, it does vary among basins. More snowstorms tend to occur across the northern basins (e.g. Upper Sacramento, Yuba, American, Carson, etc.) than in the southern Sierra Nevada (e.g. San Joaquin, Kings, Mono, Owens, Kern, etc.) (not shown). Variations in the number of snowstorms result from the movement and location of the storm track during the wintertime (discussed below). Correspondingly, the northern basins also have more *SSDs* than the southern basins (Figure 2.6). The total number of *SSDs* can be thought of as an analog to the length of the snow accumulation season as it varies with elevation and geographic location. Hence, Figure 2.6 shows that, on average, the southern basins have shorter accumulation seasons and faster accumulation rates. Also, lower elevations accumulate their CS more rapidly (i.e. fewer *SSDs*) than higher elevations. Low elevations are also most susceptible to temperature fluctuations that

shift the snow line and alter the duration of the accumulation season. *SSDs* are further discussed below to characterize the climatological rate of CS accumulation regionally and elevationally.

Since previous studies using (spatially) sparse in situ data often led to generalized range-wide conclusions, regional variability of snowstorms (Figure A.2) is discussed here. The NW has the longest duration snowstorms and the greatest number of snowstorms. As expected, the number of snowstorms decreases with duration across each region. Roughly two-thirds of all snowstorms last 1-2 days with ~93-96% of the storms lasting five days or less. In contrast, the duration of the leading snowstorms exhibits a distribution that more closely resembles a normal distribution. The leading snowstorms most frequently have durations of four days, except in the NW where 6-day leading events occur most often. On average, the duration of leading storms ranges from ~4.7 days (SW) to 5.7 days (NW). Snowstorms typically last ~2.4 days, while leading storms persist for ~5.1 days, on average, over the range. All basin-wide leading storms occurred for at least 2 days and tend to last longer than smaller snowstorms.

Strictly enforcing fixed storm durations (e.g. 3-day storms) would mainly misrepresent the leading storms of a season by breaking them up and thereby underestimating their total contribution to the seasonal CS (Figure A.2a). This provides one explanation for why our results show larger leading storm contributions to seasonal CS than *Serreze et al.* [2001] and *Lundquist et al.* [2015]. Furthermore, differences also arise from our ability to more adequately capture the high degree of heterogeneity of the CS distribution than in previous studies.

The smallest snowstorm sizes (average CS over basins during snowstorms, Figure A.2b) are the most prevalent. Regionally, ~36-64% of storms yield an average increase in CS of <2 cm, while 75-91% of snowstorms result in <6 cm. About 95% of all storms across the range result in an increase of CS <14 cm with ~66% of those storms having <4 cm of average accumulation across the range. The leeward basins (in particular the SE) have the highest percentages of small-

sized storms and leading snowstorms and the lowest snowfall intensities (not shown) when compared to the windward basins. These differences are indicative of the windward side enhancement of snowfall that contrasts the leeward side (i.e. the rain shadow effect). Since the regional distributions of all snowstorm intensities are similar to that of leading snowstorms, this indicates that the longer durations of leading snowstorms are the main driver of their larger CS accumulation/size. This also explains why the number of $SSDs$ serves as a better predictor of CS than snowstorms (Figure 2.5c).

2.3.4 Seasonality of Snowstorms and Leading Storm Contributions

Similar to previous literature the (largest) snowstorms occur most frequently from December-March across the range [e.g. *O'Hara et al.*, 2009], with ~17-24% occurring during each of these months. December-January-February (DJF) account for roughly two-thirds of the snowstorms that occur and there is a relatively uniform distribution of snowstorms spanning DJF. The majority of accumulation season storms happen during these three months since the storm track moves southward in the wintertime from its otherwise more northern location. As the storm track moves northward during the springtime, the number of large snowstorms diminishes and the accumulation season concludes. The storm track spends more time over the northern basins [*O'Hara et al.,* 2009], resulting in a larger fraction of leading snowstorms occurring late in the season in the north as well as more snowstorms and $SSDs$ in that region, on average (Figure 2.6).

Few studies have explored the regional distributions of basin-wide leading snowstorms and their contributions to CS across the range as presented herein because prior studies have largely quantified snowstorm events based on in situ measurements. While the seasonality of all storms exhibited a similar distribution across the range (not shown), the distribution of leading

storms (Figure 2.7) displays stronger regional variability. Leading storms in the NW generally exhibited a bimodal distribution with February, followed by December, having the largest fractions of leading storms. Historically, the largest storms in the NW have more frequently occurred earlier in the season during December (30.0%) than in the SW (22.6%), NE (23.7%), or SE (18.3%). It is important to recognize differences in leading storm timing across the range because if a very large storm occurs in one region, it does not necessarily mean that the entire range will similarly experience its largest snowstorm. The southern basins show an increasing number of leading storms November-February, after which the number decreases as the melt season approaches. The NE basins experienced the same number of leading storms in December and January, but nearly twice as many in February as in either of those months.

Understanding when snowstorms and specifically the leading snowstorms of each season occur is important since water managers are often interested in the 1 April snowpack, which is used to estimate the potential seasonal snowmelt contribution to streamflow [*Serreze et al.,* 2001]. As demonstrated in Figure 2.7, leading snowstorms tend to occur well before 1 April. Across the range, ~89% of the leading storms occurred during DJF, with ~41% of the leading storms occurring in February alone and contributing, on average, ~29% of the seasonal CS. Since March only accounted for ~8% of the leading storms, the likelihood that the largest storm of a season will occur very close to 1 April (i.e. after February) is low. Leading snowstorms that occurred in March generally contributed less to the CS than snowstorms occurring in February, with the largest difference in the SE at ~13% less. In the western and eastern basins, this amounts to ~3% and 10% less on average, respectively. Overall when snowstorms do occur in March, they should not be expected to yield the largest contribution to the seasonal CS. Also, relatively few leading snowstorms occurred in November; however, when they did occur, they yielded >20% of the seasonal CS, on average.

On average, DJF leading storm contributions are relatively uniform ~26.0-28.9% of the CS at the range-scale (Figure 2.7), but significant variability exists. For instance, of the leading events that occurred during December in the NW, the inter-decile range of contributions (not shown) was 28.2%, which is greater than the average leading snowstorm CS contribution during that month across the domain, excluding the SE. This again elucidates the importance of a single storm as well as how spatially and temporally variable snowstorm contributions and the regional hydroclimate can be.

2.3.5 Climatological Rate of Snowfall Accumulation and Inter-annual Variability

2.3.5.1 CS Cumulative Distribution Functions

Figure 2.8 presents the relationship between the number of snowstorms and $SSDs$ during a season and their relative contribution to the seasonal CS for each basin, respectively. While an average of 11 storms occurs annually across the range (Figure 2.8a, vertical line), the average number of snowstorms varies from ~9-12 for individual basins. Figure 2.8a was constructed similarly to a cumulative distribution function (CDF) where the average contribution of less than or equal to a given number of storms was considered up to the maximum number of basin-wide storms that occurred over the record (i.e. 13-23 storms). The CDFs in Figure 2.8b were similarly constructed for $SSDs$. Consequently, all years were considered at each point along the curves. As the number of snowstorms or $SSDs$ increases, its relative contribution to the seasonal CS decreases in Figure 2.8. Recall that the snowstorm definition herein was designed to identify the largest events of a season as opposed to all increases in CS (Figure 2.1). Therefore, the 31-year average CDFs in Figure 2.8 indicate that large snowstorms accounted for ~83-93% of the CS across basins, leaving smaller events to deposit the remaining ~7-17% of CS.

Despite significant variability among the watersheds (e.g. elevations, geographic locations, CS volume, etc.), the CDFs in Figure 2.8a demonstrate that the climatological rate of snowfall accumulation exhibits a similar response over the entire range. The leading storm typically contributes ~27% of the total CS volume during a season (Figure 2.8a), which ranges from ~23.4-34.6% across basins, on average. The inter-decile range for basin-wide leading snowstorm contributions is large with the most extreme 10^{th}/90^{th}-percentiles for basins being 13.4-60.6% (not shown). For comparison, *Lundquist et al.* [2015] estimated that the largest 3-day and 5-day events contributed about 9-25% (median 15%) and 12-29% (median 19%) of the annual snowfall, respectively. *Serreze et al.* [2001] estimated that leading 3-day snowstorms contributed an average 17% to the CS across the range, which is larger than their estimates of ~12% in the Pacific Northwest, ~11% in Utah, and ~10% in Colorado. Both of these previous studies used point-scale in situ measurements and 3-day or 5-day events. In addition, Figure 2.8 was constructed using the CS volume over each basin, which could not be directly quantified using sparse point-scale measurements alone. Therefore, our estimate provides a more robust representation of accumulation across the range.

Typically, the second largest storm of the season increases the snowstorm contribution to ~44% (Figure 2.8a). On average, all basins accumulate >50% of the CS within the largest three storms of a season, with basins accumulating as much as 65% of their CS within those three storms (31-year average). About five storms or fewer result in at least ~71% of the seasonal CS volume, on average, (Figure 2.8a) with this ranging from ~45-95% in the most extreme cases (10^{th}/90^{th}-percentiles, not shown). Not only are the 31-year basin averages similar in Figure 2.8a, but such relationships are also observed in Figure 2.8b.

The large contributions that a few storms make to the accumulation of snowfall over this range greatly elucidate the importance of each wintertime storm in the Sierra Nevada (Figures

2.7-2.8). The presence of one or a few larger/smaller storms than average can be the difference between a wet and a dry year. *Dettinger et al.* [2011] drew similar conclusions regarding precipitation patterns across California. Persistent atmospheric phenomena that alter the storm track could have a substantial impact on the CS over the Sierra Nevada. For instance, the resilient high pressure ridge that recently deflected the storm track north of the range [e.g. *Swain et al.,* 2014; *Seager et al.,* 2015], manifested itself in an exceptionally strong multi-year drought beginning in WY 2012 [*M16b*]. Hence during any given year, a shift in the storm track could greatly impact the amount of precipitation/snowfall and the water supply across California. *Dettinger* [2013] showed that one or two large storms in California could make a significant difference in drought recovery and local/regional water resources. Often the Sierra Nevada experiences one to a few exceptionally large snowstorms each year that make up the majority of the CS (Figure 2.8a).

The deflection of a few large snowstorms would also result in fewer $SSDs$ and lead to nonlinear decreases in the integrated CS volume (Eq. (2.4) and Figure 2.5c, right). When the $SSDs$ were ranked pixel-wise and the resulting CS was integrated across the basin for each year, the 31-year average CDFs in Figure 2.8b indicate that, on average, one SSD can result in 10.3-18.5% of the CS. Remarkably if the most extreme 10^{th}/90^{th}-percentile cases were considered, one SSD can yield 6.6-27.2% of the CS (not shown), where the 90^{th}-percentile value is on the order of the 31-year average leading snowstorm contribution. The largest five $SSDs$ yield 36.8-53.5% of the integrated CS across basins, on average. Although leading storms are typically five days long, each of these days may not be classified among the greatest five days of increases in CS for each pixel as represented in Figure 2.8b. Nonetheless, these values represent another metric for evaluating how rapidly the snowfall typically accumulates. Selecting any of the curves in Figure

2.8 and analyzing the rate of accumulation up to say 50% or 75%, would result in similar conclusions: few snowstorms and $SSDs$ result in the majority of the CS across the mountain range.

2.3.5.2 Spatial Distribution of Calendar Days and Storm Snow Days

Detailed maps of accumulation rates have not been previously available across an entire mountain range as shown in Figure 2.9. Figure 2.9a presents the 31-year average number of CDs it takes to accumulate 50, 75, and 100% of the CS, respectively, across the range. Recall that 1 November corresponds to one CD. The spatial average of the 31-year climatology CD_{50} maps corresponds to 85.2 days or 24 January and the CD_{50} accumulation rates vary from ~53.1-108.2 days across the entire domain shown in Figure 2.9a (left). Furthermore, the spatial averages of the climatology maps demonstrate that on average CD_{75} corresponds to 106.7 days or 15 February (~63.0-125.5 days) and CD_{100} corresponds to 129.2 days or 9 March (~67.5-142.8 days) across the Sierra Nevada, where the ranges of CDs in parentheses indicate the 31-year average minimum and maximum values observed across the domain in each map. *Cayan et al.* [2003] estimated that ~67% of the annual precipitation across California accumulates in ~90-120 days on average, which is shorter than any other state (~150-250 days/year). As demonstrated here, the Sierra Nevada often accumulates its CS faster than the total precipitation accumulation rates over the entire state.

The difference between the minimum and maximum values (presented above) across each of the climatological maps in Figure 2.9a represents substantial variability in the accumulation rates over the domain, ~55-75 days (or ~2-2.5 months). However, the standard deviations across the climatological maps in Figure 2.9a are small, 5.3-9.0 days (or <1-2 weeks). Since CDs are a measure of the length of the accumulation season and the seasonality or timing

of snowfall, the magnitude of the standard deviation is consistent with the concept of event coherence *Serreze et al.* [2001] identified across the range. The range in the 31-year average CD_{100} accumulation rates by the DOP (Figure 2.9a, right) illustrates that the accumulation season often ends significantly before 1 April, i.e. 152 days. While it takes ~85 days to accumulate 50% of the CS, it only takes an additional ~21.5 days to achieve 75% in mid-February and another ~22.5 days to reach 100% accumulation in early March, on average. This demonstrates that large CS increases (~50% of the CS), not simply leading storms, often occur in February.

When $SSDs$ are ranked pixel-wise to generate the climatological maps in Figure 2.9b, the rapid rate of accumulation is more clearly identified. Since $SSDs$ were defined during snowstorm events, Figure 2.9b does not provide a map of the time to achieve 100% accumulation for the same reasons that the CDFs do not reach 100% in Figure 2.8. The pixels across the range accumulate ≥50% of the CS, on average, in only ~6.4 $SSDs$ (long-term spatial average). *Lundquist et al.* [2015] estimated that it took ~10 days (median) to achieve 50% accumulation using station data across the Sierra Nevada. We further estimate that the 31-year spatial average of SSD_{75} corresponds to 12.4 days/year. As depicted in Figure 2.9, the leeward basins accumulate their CS in the fewest number of days compared to the rest of the range. Moreover, southern basins often accumulate their CS at a more rapid rate than northern basins (Figure 2.9b).

The brevity of the accumulation season is further exemplified by considering the maximum number of $SSDs$ across each of the maps in Figure 2.9b as these values still represent markedly few days. On average, all pixels across the domain achieve ≥50% and ≥75% of their CS in <13 $SSDs$ and <24 $SSDs$, respectively. Considering the larger context of the state of

California, *Dettinger et al.* [2011] estimated that ~33-50% of the annual precipitation over the state was achieved in ~5-10 wet days/year; however, their estimate included comparatively few data points over the Sierra Nevada. Our estimated average rate of 50% accumulation (~6.4 $SSDs$) is near the lower bound of their estimate for the entire state, while the maximum value of SSD_{50} (~13 $SSDs$) is close to the upper bound for the state.

As the percent accumulation increases from 50% to 75%, the SSD patterns in Figure 2.9b more closely resemble that of the 31-year average CS distribution (Figure 2.4a, left). Higher elevations with more CS also have higher values of SSD_p than lower elevations. While a high-elevation pixel takes longer to accumulate a given fraction of its CS, an increase of p % likely represents significantly more CS at higher elevations than at lower ones (Figure 2.4).

2.3.5.3 Elevational Distribution of Accumulation Rates

Since in situ measurements primarily sample low and mid-elevations, snowfall accumulation rates at the highest elevations remain largely unknown. Figure 2.10 aims to fill this gap by expanding upon the spatial distribution of accumulation rates shown in Figure 2.9 to more fully characterize how the rates vary with elevation. Figures 2.10a and 2.10b present the same percentages p, utilized in Figures 2.9a and 2.9b for CD_p and SSD_p, respectively. Since higher elevations tend to receive snowfall earlier in the season than lower elevations, the 31-year average CD_{50} curves (blue) indicate that ≥50% of the CS is reached earlier with increasing elevation (Figure 2.10a). However, the shape of the curves is altered from 50% to higher values of p since higher elevations receive snowfall over a longer fraction of the season than lower elevations.

Regional differences in accumulation rates as a function of elevation are apparent among the 31-year average curves (solid lines) in Figure 2.10. In Figure 2.10a for instance, the SW

typically accumulates CS at a relatively constant rate with elevation as opposed to regions such as the SE where CD_p exhibits a stronger elevational dependence. Similar relationships are also observed between the western and eastern basins, which reflect rain shadow features. Although high inter-annual variability exists (shaded areas), on average, windward basins tend to experience CS increases at similar times throughout the season regardless of the elevation. Since most snowfall events are due to westerlies, spillover results in snowfall accumulation on the eastern side of the mountain range, which means that the highest elevations often receive more CS and have more opportunities to experience increases in CS than the lowest ones (subject to warmer and drier atmospheric conditions). Thus, there is greater elevational variability exhibited by the 31-year average curves on the leeward side. While lower elevations have fewer CDs and $SSDs$ overall (Figure 2.10) due to fluctuations in the snow line, the fastest accumulation rates are observed among the eastern basins where negligible CS often occurs (Figure 2.4a).

With larger CS totals, higher elevations generally receive snowfall over a greater fraction of days during the season (Figure 2.10b). The shapes of the SSD_p curves resemble the shapes of the basin-wide orographic CS curves presented in *HM17* along the western slope: 1) increasing or 2) increasing to a maximum and then decreasing with elevation. These shapes are similarly observed for the regional accumulation rates in Figure 2.10b range-wide. It is not surprising that orographic snowfall processes are tightly coupled to accumulation rates. *HM17* hypothesized that declines in CS at the highest elevations resulted from gravitational and wind redistribution as well as atmospheric moisture exhaustion. These processes would similarly explain the decreasing SSD_p curves at the highest elevations in Figure 2.10b.

While the inter-annual variability of SSD_p increases with elevation (Figure 2.10b), it remains large throughout for CD_p (Figure 2.10a). Not only does Figure 2.10a show substantial

inter-annual variability (much greater than in Figure 2.10b), but the CD_{50} and CD_{75} interquartile ranges can largely overlap with one another. Thus, high variability is associated with the inter-annual timing of snowfall accumulation (often more than one month at a given elevation) as well as when the larger-sized storms occur. It also indicates that the length of the accumulation season can greatly vary inter-annually and elevationally across the range since the CD_{100} curves/interquartile ranges represent the end of the season (i.e. DOP SWE). The narrow inter-annual variability associated with SSD_p (Figure 2.10b) demonstrates that relatively few days are needed for the range to accumulate p% of the CS. In fact, across nearly all regions and elevations, the 75th-percentile of SSD_{50} is <10 days. The 75th-percentile of SSD_{75} is <25 days in all regions. The inter-annual variability is the largest for CD_{50} (Figure 2.10a), whereas it is the smallest for SSD_{50} (Figure 2.10b). The timing of when 50% of the CS accumulates will greatly vary from year-to-year while the largest accumulation always occurs very rapidly over the course of a few days and/or storms when ranked (Figures 2.8-2.10).

Although Figures 2.8-2.10 quantify the climatological rate of snowfall accumulation using different metrics (i.e. snowstorms, CDs, and $SSDs$), all approaches illustrate the brevity of the snowstorm-driven accumulation season despite regional and elevational heterogeneities. Furthermore, the relatively small number of storms and $SSDs$ that make up large fractions of the total CS elucidates the importance of accurate estimates of the CS and how rapidly the CS accumulates. Inaccurate forecasts of the storm track or poor estimation of a few (or even a single) snowstorm could result in large accumulation errors across the range causing significant water resources management implications.

2.4 Conclusion

Using a multi-decadal spatially-distributed SWE dataset, we provided a more detailed characterization of the climatological CS timing, distribution, and accumulation rate over the entire Sierra Nevada than previously existed. Insight into the occurrence of leading storms and the end of the accumulation season (generally before 1 April) as well as the development of models for estimating the integrated CS should lead to more informed water resources management decisions. Regardless of the metric used, the rapid rate CS accumulates was consistently observed across all elevations and regions in the Sierra Nevada. Given the fast accumulation rates and substantial contributions of the largest snowstorms, inadequately capturing the impact of a single snowstorm (or storm snow day) may result in poor representations of the seasonal CS. This is evidenced by the leading storm of a season yielding an average 27% of the CS annually.

With future climate projections indicating that there may be more frequent and long lasting droughts across the western USA, California may be particularly susceptible if several storms will be deflected north of the Sierra Nevada as in the case of the "Ridiculously Resilient Ridge" [*Swain et al.,* 2014]. With the deflection of a few large storms during a given season or multiple consecutive seasons, CS will likely be low. The recent drought could serve as a case study for understanding the potential implications on snowstorm-driven snowfall accumulation, reservoir operations (e.g. timing of releases), and water management.

With the climatology presented herein, and such efforts across other hydrologically relevant mountain ranges, we can work toward improving existing models and developing more robust parameterizations to describe seasonal snowfall. Results from this study can be used to evaluate how well climate models can represent the spatiotemporal variability of CS and its rate

of accumulation, the rain shadow effect, and elevational CS distributions. Such future work is important because climate models generally yield biased estimates of precipitation and snowfall. This work could provide guidance on physical constraints used in modeling accumulation rates, storm sizes, etc. Understanding the extent to which climate models can represent the historical CS is valuable for quantifying uncertainties in climate models and interpreting projections in the hydroclimate of snow-dominated montane regions.

2.5 Figures

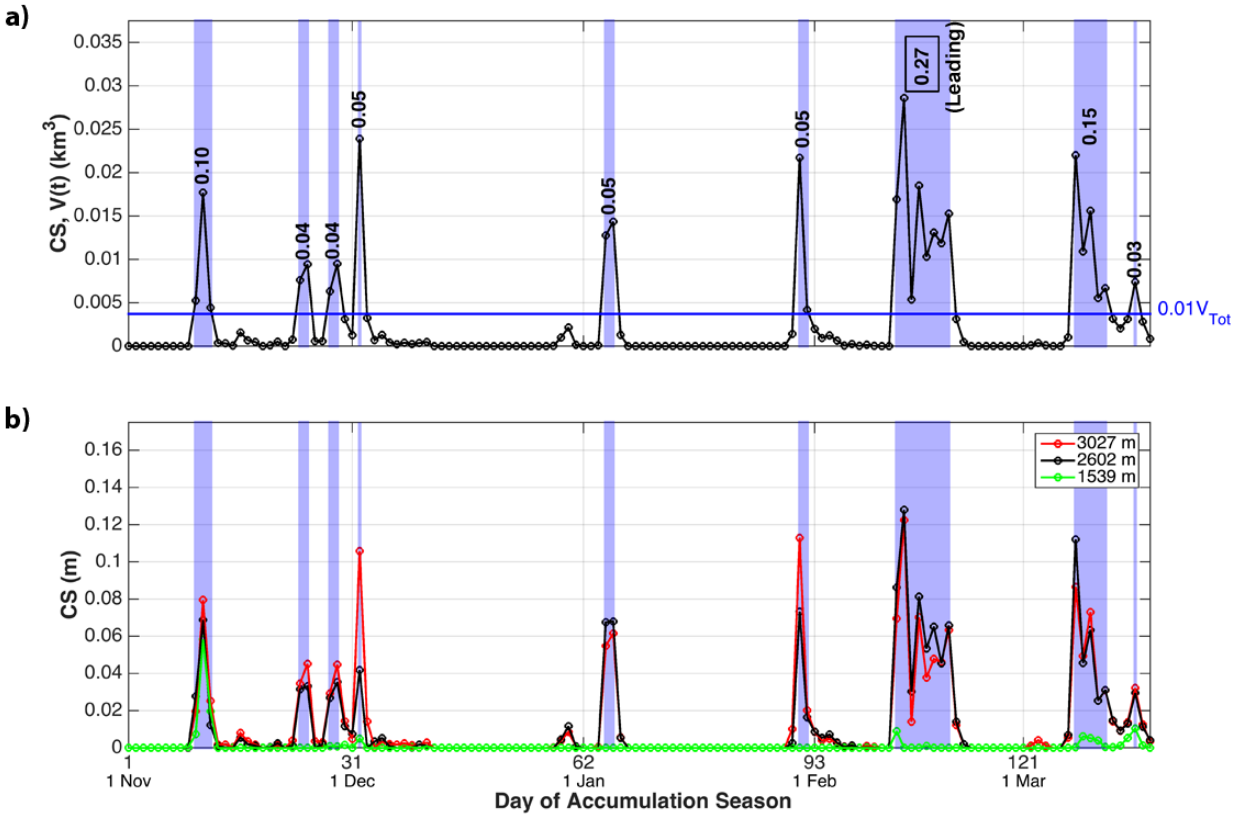

Figure 2.1. Illustration of snowstorm definition and metrics. a) Representative time series of the daily CS volume $V(t)$ accumulated at elevations above EL_{75} over the accumulation season for an example basin (Kaweah) and season (WY 1986). Snowstorm events (shaded) were defined for consecutive days where $V(t)$ was ≥1% of the seasonally-integrated CS above EL_{75} as demarcated by the horizontal line. Boldface numerals represent the integrated basin CS storm volumes (over all pixels) with the value of the leading storm event boxed. b) For the same basin and year, three pixels of differing elevations were selected to illustrate pixel-wise variability in the number of storm snow days.

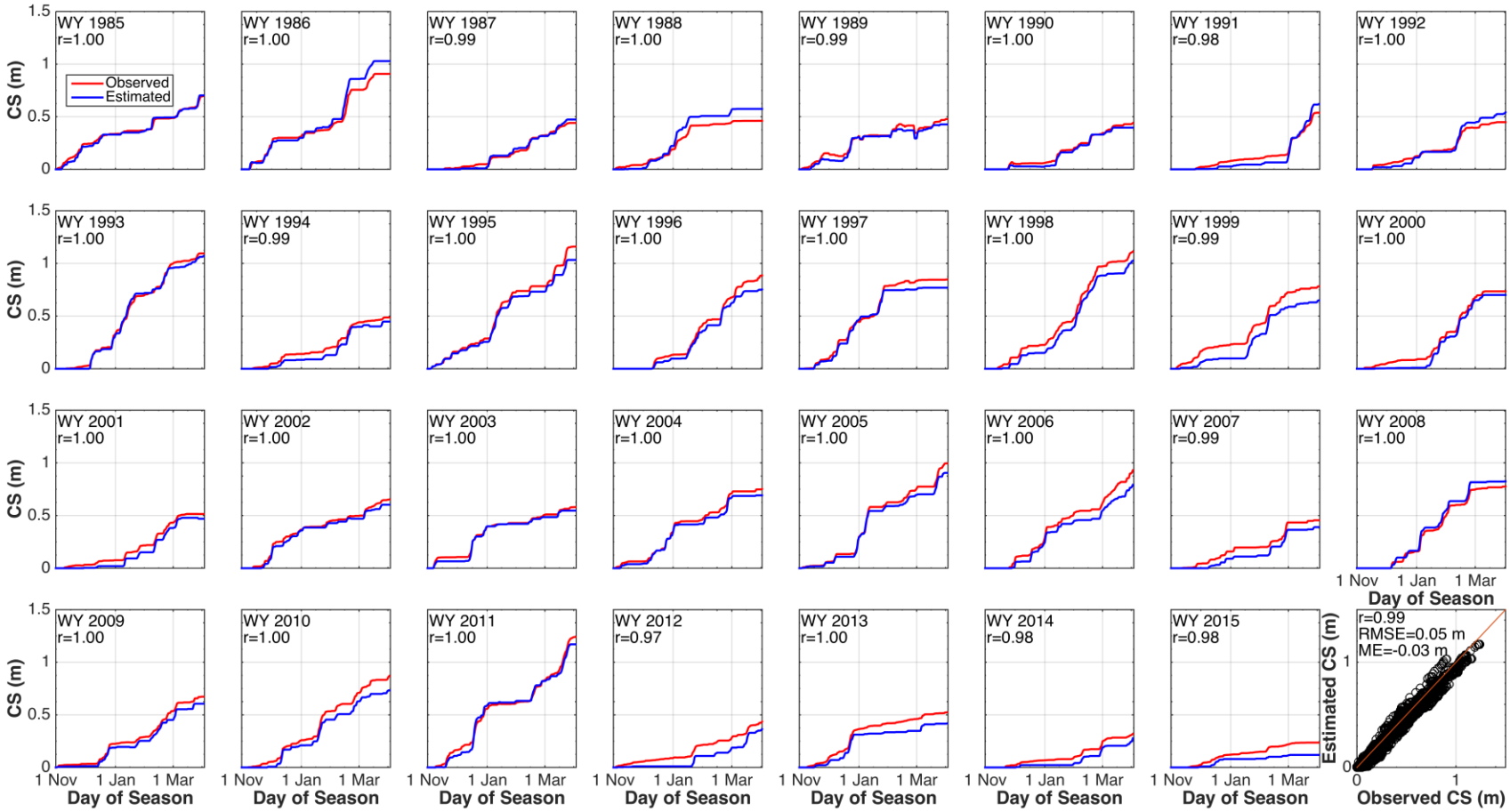

Figure 2.2. Median CS time series for observations (red) at snow pillows and estimates (blue) from the (posterior) SWE reanalysis for 31 accumulation seasons (1 November-1 April). Bottom right: Comparison of daily median estimated and observed CS for 31 seasons. The 1:1 line is shown in red. All correlations are statistically significant with $p = 0.00$.

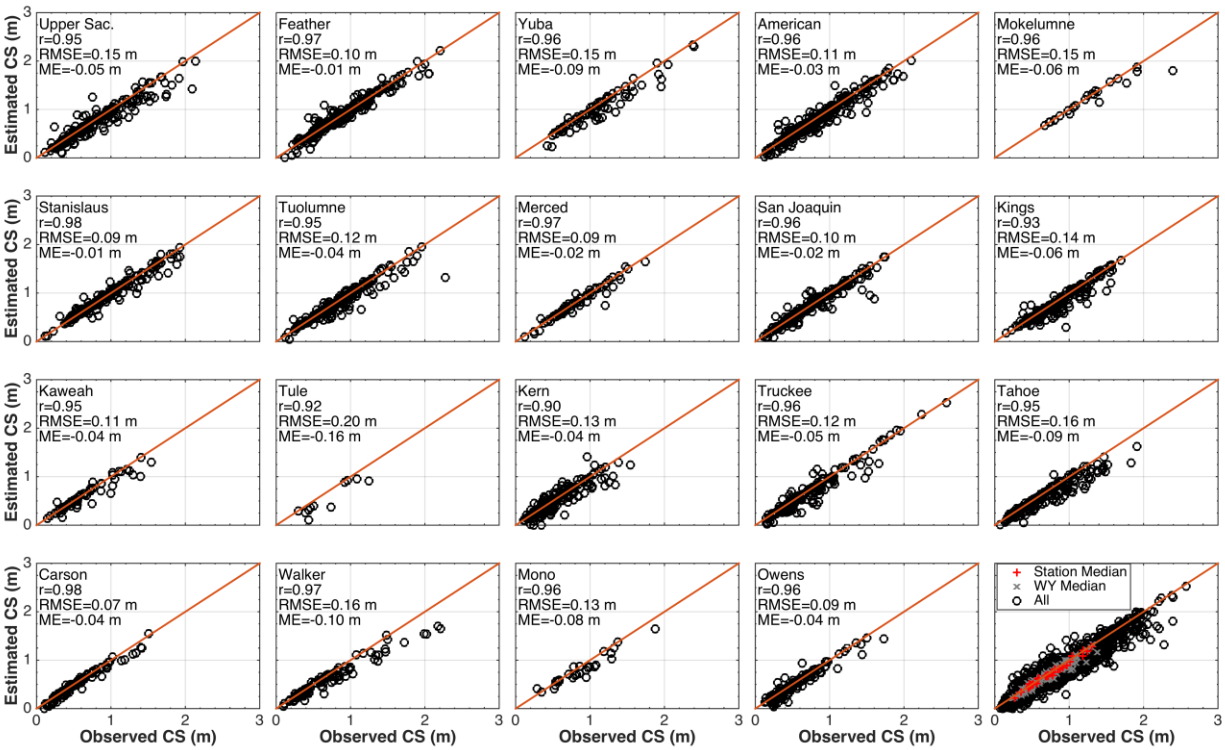

Figure 2.3. Comparison of estimated (reanalysis) and observed (snow pillows) CS on 1 April over the 31 years for each basin. Bottom right: Seasonal median CS over all stations for each year ('+' symbols), seasonal median CS over all years for each station ('×' symbols), and seasonal CS for all stations and years ('o' symbols) with correlation coefficients $r \geq 0.96$. The 1:1 line is shown in red. All correlations are statistically significant with $p = 0.00$.

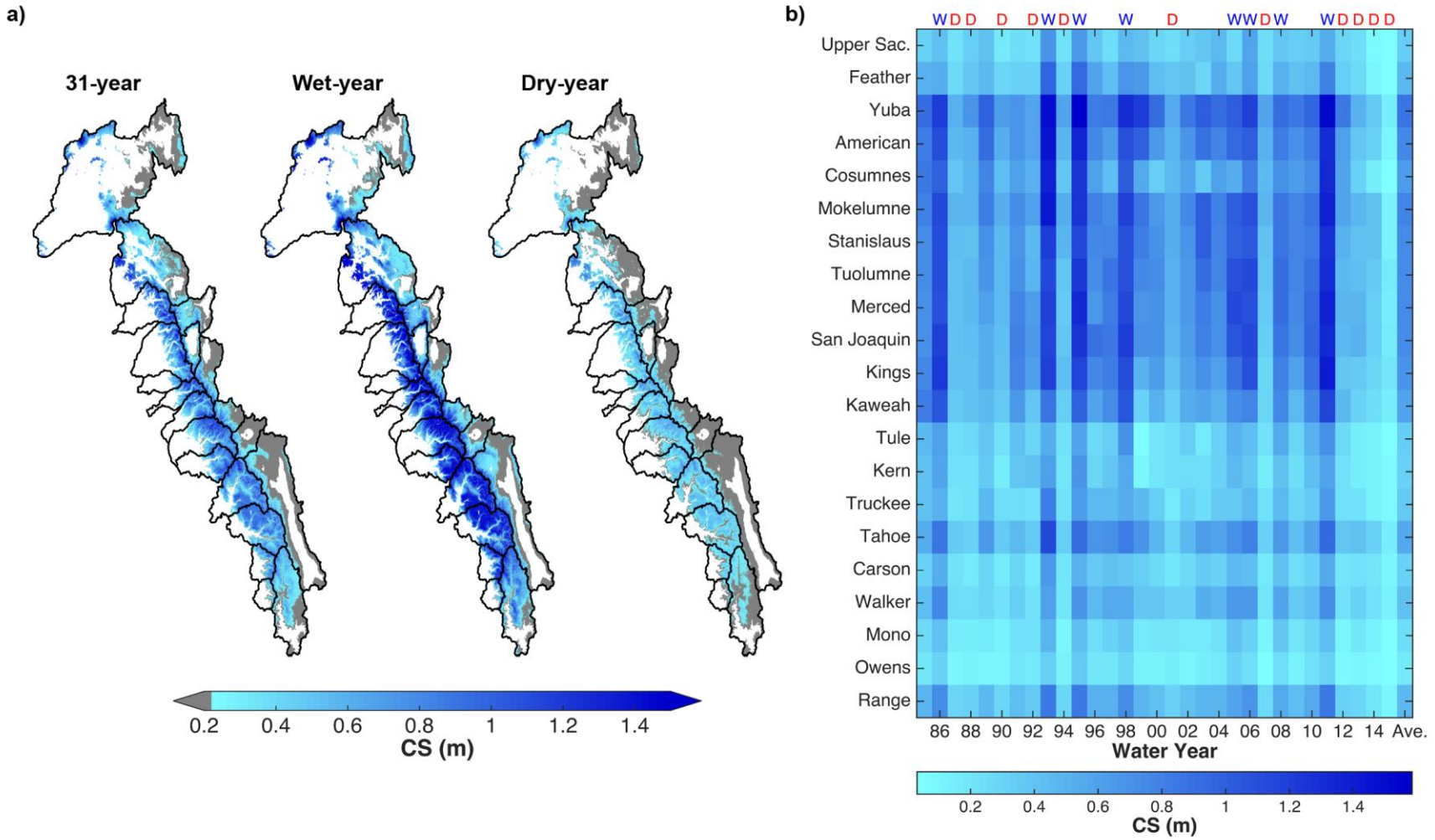

Figure 2.4. a) Thirty-one-year, wet-year, and dry-year average CS maps, respectively. b) Array of the average CS depth for each basin and the full mountain range over WYs 1985-2015. The rightmost column contains the 31-year average. Wet and dry years are denoted with ‘W’ and ‘D’, respectively.

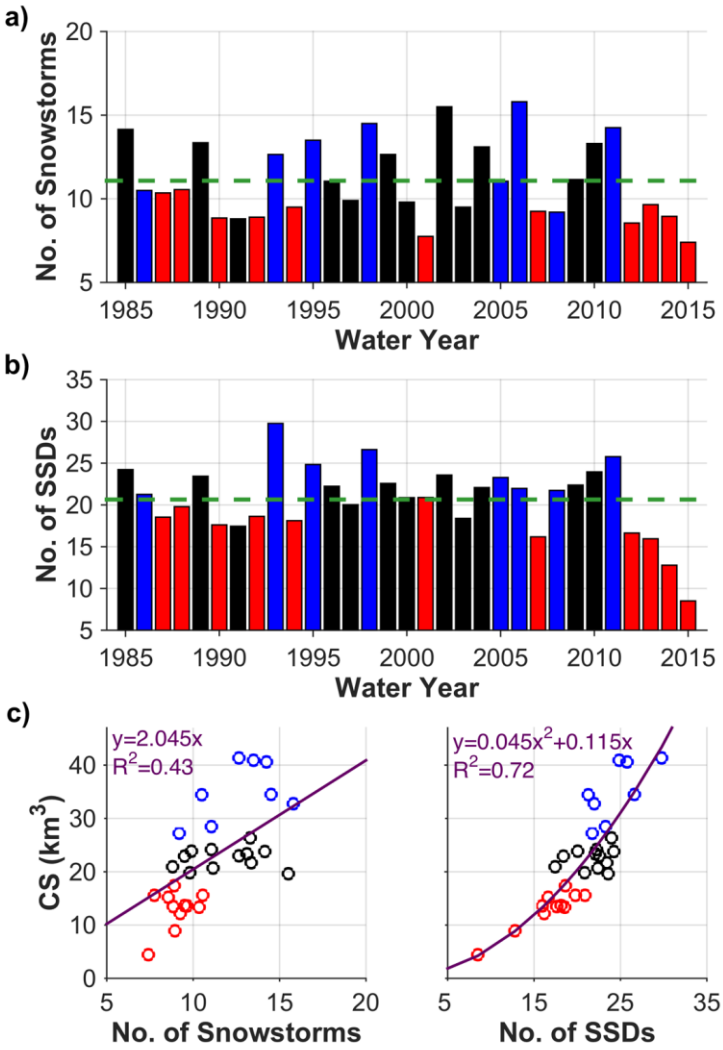

Figure 2.5. Time series of the average number of a) snowstorms and b) storm snow days ($SSDs$) across the Sierra Nevada. Dashed lines demarcate the 31-year average. c) Integrated CS volume over all basins and the average number of (left) snowstorms and (right) $SSDs$ for each of the 31 years. Each fit is statistically significant with $p = 0.00$. In all panels, wet years and dry years are colored blue and red, respectively.

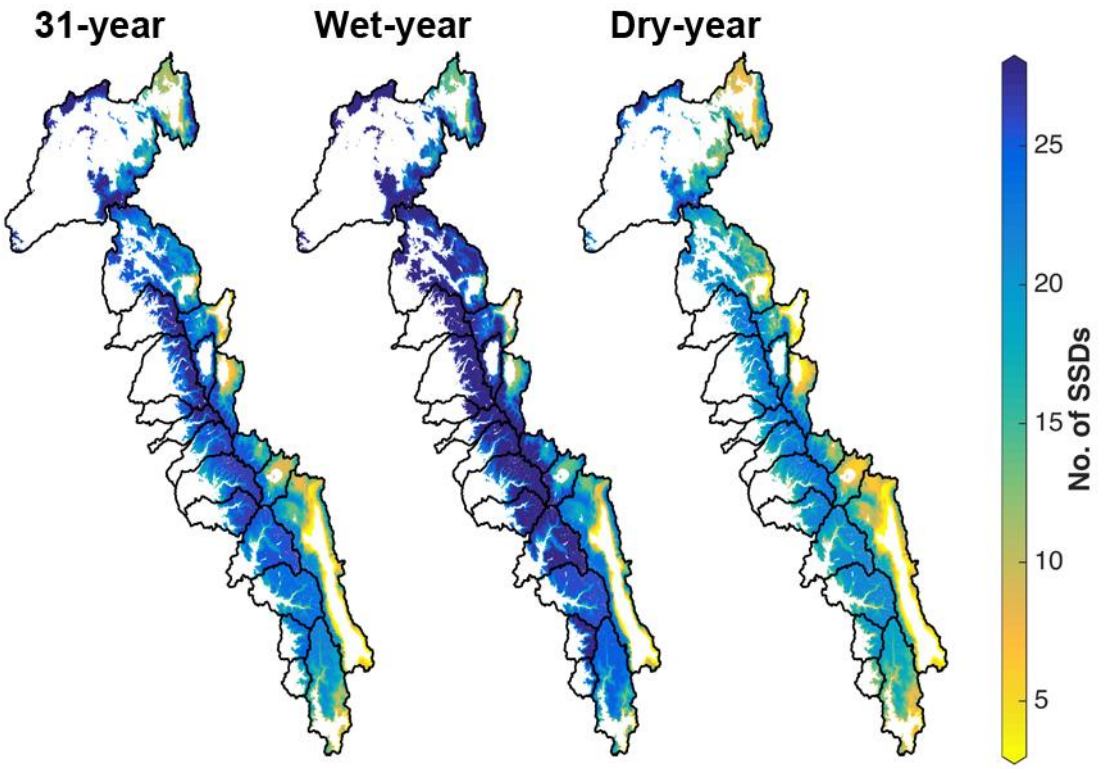

Figure 2.6. Thirty-one-year, wet-year, and dry-year averages of the total number of $SSDs$.

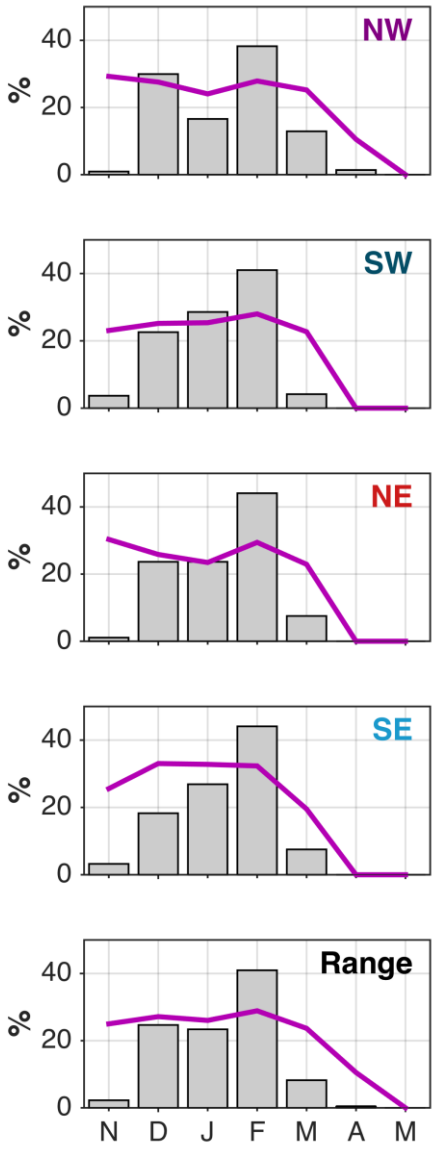

Figure 2.7. Seasonality of snowstorms. Bars indicate the frequency of the leading storm occurrence in a given month over the 31 seasons. Of those leading snowstorms, the curve indicates the average contribution leading storms made to the seasonal-integrated CS volume for each basin in the region.

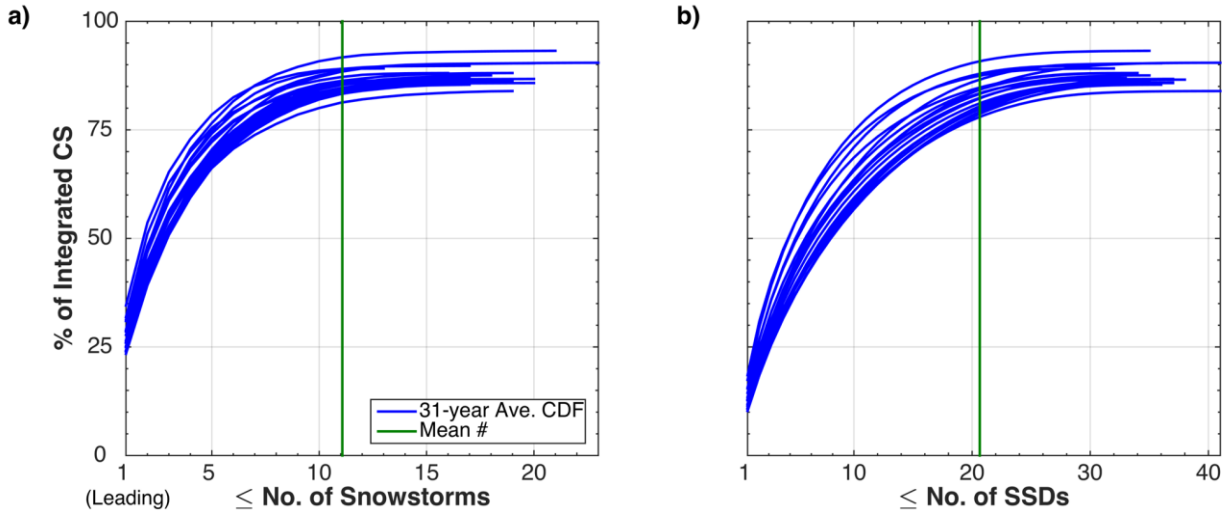

Figure 2.8. Thirty-one-year average cumulative distribution functions (CDFs) showing the contribution of (ranked) a) snowstorms and b) *SSDs* to the integrated CS for each basin. Individual basins were not identified by color since the CDFs are similar. Vertical green lines demarcate the range-wide mean number of snowstorms and *SSDs* in a) and b), respectively.

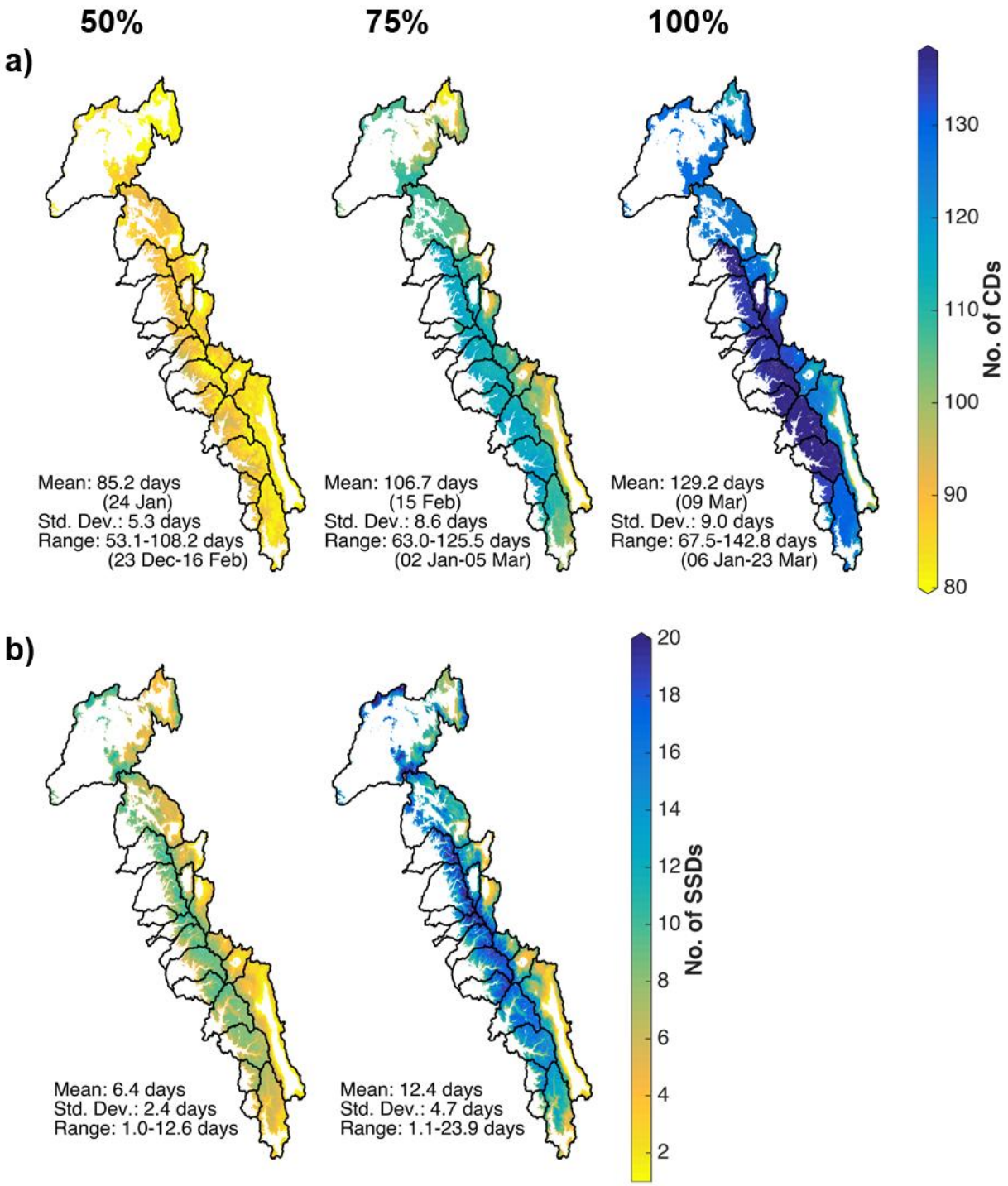

Figure 2.9. Thirty-one-year average number of a) *CDs* (chronological) and b) *SSDs* (ranked) to accumulate at least 50% (first column), 75%, and 100% (third column) of the CS, respectively. Refer to the text for the discussion explaining why the 100% maps were excluded from b). The (spatially-averaged) range-wide statistics are provided for each 31-year average map. Dates were rounded to the nearest day.

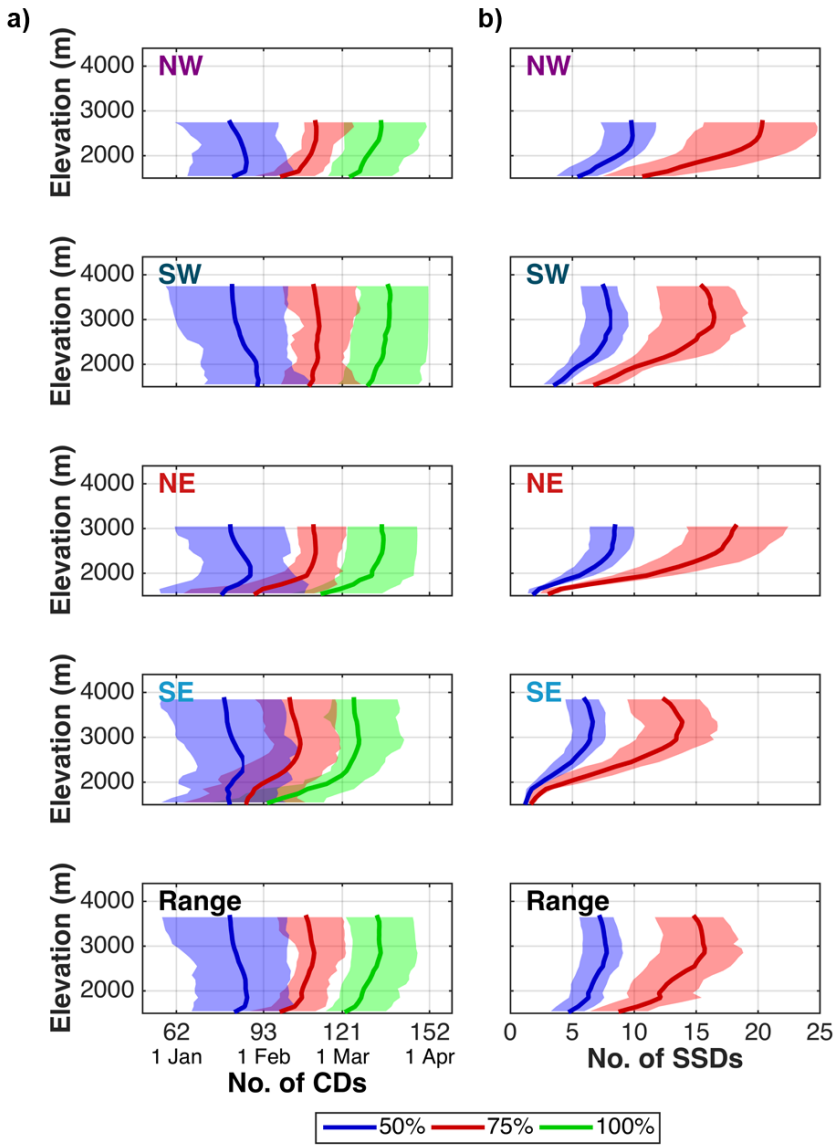

Figure 2.10. Elevational distribution of a) *CDs* and b) *SSDs* for the same percentages of CS shown in Figures 2.9a and 2.9b, respectively. Solid lines represent the 31-year average and shaded regions represent the interquartile range. Elevation bins with >0.5% of the regional area above 1500 m are shown following *Grünewald et al.* [2014] and *HM17*.

2.6 Bibliography

Bales, R., J. J. Battles, Y. Chen, M. H. Conklin, E. Holst, K. L. O'Hara, P. Saksa, and W. Stewart (2011), Forests and water in the Sierra Nevada: Sierra Nevada watershed ecosystem enhancement project, Sierra Nevada Research Institute, Report Number 11.1.

Cayan, D. R., M. D. Dettinger, K. T. Redmond, G. J. McCabe, N. Knowles, and D. H. Peterson (2003), The transboundary setting of California's water and hydropower systems: Linkages between the Sierra Nevada, Columbia River, and Colorado River hydroclimates, in *Climate and Water—Transboundary Challenges in the Americas*: Diaz, H.F., and B.J. Morehouse Eds., Kluwer Academic: Dordrecht, Netherlands, pp. 237-262.

Dettinger, M. D. (2013), Atmospheric rivers as drought busters on the U.S. West Coast, *J. Hydrometeorol.*, 14, 1721-1732, doi:10.1175/JHM-D-13-02.1.

Dettinger, M. D. (2016), Historical and future relations between large storms and droughts in California, *San Franc. Estuary Watershed Sci.*, 14(2), 1-21, doi:10.15447/sfews.2016v14iss2art1.

Dettinger, M. D., and D. R. Cayan (2014), Drought and the California Delta—A matter of extremes, *San Franc. Estuary Watershed Sci.*, 12(2), 1-6, doi:10.15447/sfews.2014v12iss2art4.

Dettinger, M. D., F. M. Ralph, T. Das, P. J. Neiman, and D. R. Cayan (2011), Atmospheric rivers, floods and the water resources of California, *Water*, 3, 445-478, doi:10.3390/w3020445.

Dettinger, M. D., K. Redmond, and D. Cayan (2004), Winter orographic precipitation ratios in the Sierra Nevada – Large-scale atmospheric circulations and hydrologic consequences, *J. Hydrometeor.*, 5, 1102-1116.

Downing, J. (2015), Forest thinning may increase water yield from the Sierra Nevada, *Calif. Agr.*, 69(1), 10-11.

Dozier, J. (2011), Mountain hydrology, snow color, and the fourth paradigm, *EOS Trans. AGU*, 29(43), 373-374.

Dozier, J., E. H. Bair, and R. E. Davis (2016), Estimating the spatial distribution of snow water equivalent in the world's mountains, *WIREs Water*, 3, 461-474, doi:10.1002/wat2.1140.

Grubišić, V., R. K. Vellore, and A. W. Huggins (2005), Quantitative precipitation forecasting of wintertime storms in the Sierra Nevada: Sensitivity to the microphysical parameterizations and horizontal resolution, *Mon. Wea. Rev.*, 133, 2834-2859.

Grünewald, T., Y. Buhler, and M. Lehning (2014), Elevation dependency of mountain snow depth, *Cryosphere*, 8, 2381-2394, doi:10.5194/tc-8-2381-2014.

Guan, B., N. P. Molotch, D. E. Waliser, E. J. Fetzer, and P. J. Neiman (2010), Extreme snowfall events linked to atmospheric rivers and surface air temperature via satellite measurements, *Geophys. Res. Lett.*, 37, L20401, doi:10.1029/2010GL044696.

Guan, B., N. P. Molotch, D. E. Waliser, S. M. Jepsen, T. H. Painter, and J. Dozier (2013), Snow water equivalent in the Sierra Nevada: Blending snow sensor observations with snowmelt model simulations, *Water Resour. Res.*, 49, 5029-5046, doi:10.1002/wrcr.20387.

Huning, L. S., and S. A. Margulis (2017), Investigating the variability of high-elevation seasonal orographic snowfall enhancement and its drivers across Sierra Nevada, California, *J. Hydrometeor.*, in review.

Kirchner, P. B., R. C. Bales, N. P. Molotch, J. Flanagan, and Q. Guo (2014), LiDAR measurement of seasonal snow accumulation along an elevation gradient in the southern Sierra Nevada, California, *Hydrol. Earth Syst. Sc.*, 18, 4261-4275, doi:10.5194/hess-18-4261-2014.

Lundquist, J., M. Hughes, B. Henn, E. Gutmann, B. Livenh, J. Dozier, and P. Neiman (2015), High-elevation precipitation patterns: Using snow measurements to assess daily gridded datasets across the Sierra Nevada, California, *J. Hydrometeor.*, 16, 1773-1792 doi:10.1175/JHM-D-15-0019.1.

Lundquist, J. D., J. R. Minder, P. J. Neiman, E. Sukovich (2010), Relationships between barrier jet heights, orographic precipitation gradients, and streamflow in the Northern Sierra Nevada, *J. Hydrometeor.*, 11, 1141-1156, doi:10.1175/2010JHM1264.1.

Margulis, S., G. Cortés, M. Girotto, and M. Durand (2016a), A Landsat-era Sierra Nevada (USA) snow reanalysis (1985-2015), *J. Hydrometeor.*, 17, 1203-1221, doi:10.1175/JHM-D-15-0177.1.

Margulis, S. A., G. Cortés, M. Girotto, L. S. Huning, D. Li, and M. Durand (2016b), Characterizing the extreme 2015 snowpack deficit in the Sierra Nevada (USA) and the implications for drought recovery, *Geophys. Res. Lett.*, 43, 6341-6349, doi:10.1002/2016GL068520.

Montoya, E. L., J. Dozier, and W. Meiring (2014), Biases of April 1 snow water equivalent records in the Sierra Nevada and their associations with large-scale climate indices, *Geophys. Res. Lett.*, 41, 5912-5918, doi:10.1002/2014GL060588.

Mote, P. W., A. F. Hamlet, M. P. Clark, and D. Lettenmaier (2005), Declining mountain snowpack in Western North American, *Bull. Amer. Meteor. Soc.*, 86(1), 39-49.

O'Hara, B. F., M. L. Kaplan, and S. J. Underwood (2009), Synoptic climatology analyses of extreme snowfalls in the Sierra Nevada, *Wea. Forecasting*, 24, 1610-1624, doi:10.1175/2009WAF2222249.1.

Rice, R., R. C. Bales, T. H. Painter, and J. Dozier (2011), Snow water equivalent along elevation gradients in the Merced and Tuolumne River basins of the Sierra Nevada, *Water Resour. Res.*, 47, W08515, doi:10.1029/2010WR009278.

Rosenthal, W., and J. Dozier (1996), Automated mapping of montane snow cover at subpixel resolution from the Landsat Thematic Mapper, *Water Resour. Res.*, 32, 115-130, doi:10.1029/95WR02718.

Seager, R., M. Hoerling, S. Schubert, H. Wang, B. Lyon, A. Kumar, J. Nakamura, and N. Henderson (2015), Causes of the 2011-14 California drought, *J. Climate*, 28, 6997-7024, doi:10.1175/JCLI-D-14-00860.1.

Serreze, M. C., M. P. Clark, and A. Frei (2001), Characteristics of large snowfall events in the montane western United States as examined using snowpack telemetry (SNOTEL) data, *Water Resour. Res.*, 37(3), 675-688.

Swain, D. L., M. Tsiang, M. Haugen, D. Singh, A. Charland, B. Rajaratnam, and N. S. Diffenbaugh (2014), The extraordinary California drought of 2013/2014: Character, context, and the role of climate change, [in "Explaining extremes of 2013 from a climate perspective"], *Bull. Amer. Meteor. Soc.*, 95(9), S3-S7.

Trujillo, E., and N. Molotch (2014), Snowpack regimes of the western United States, *Water Resour. Res.*, 50, doi:10.1002/2013WR014753.

Chapter 3: Investigating the Variability of High-elevation Seasonal Orographic Snowfall Enhancement and its Drivers across Sierra Nevada, California

3.1 Introduction

Wintertime orographic precipitation is an important process controlling the accumulation and distribution of the snowpack in high-elevation montane watersheds. Orographic precipitation results from the forced ascent of moist air over a mountain barrier. While orographic precipitation is known to be an important process in mountainous terrain [e.g. *Barros and Lettenmaier,* 1994; *Roe,* 2005; *Houze,* 2012], an accurate assessment of high-elevation gradients in total precipitation and snowfall across montane regions is still missing [*Lehning,* 2013]. Limited in situ measurements generally inhibit a full spatiotemporal characterization of orographic precipitation from the basin to mountain range scales [*Kirchner et al.,* 2014]. Without a more complete understanding of where water is stored across mountain ranges and the rate of increase in snowfall and snow water equivalent (SWE) accumulation with elevation, vital water resources are more challenging to quantify, predict, and manage.

Due to the high variability of the topography and surface characteristics in complex mountainous regions, there is often significant variability in the spatial patterns of snow accumulation resulting from localized orographic effects and atmospheric circulations [*Dettinger et al.,* 2004; *Lundquist et al.,* 2010]. When compared to high-resolution distributed snow depth measurements, *Kirchner et al.* [2014] found that point-scale snow pillow observations were not representative of the spatial variability of the montane snowpack. Many prior studies have utilized point-scale in situ measurements [e.g. *Aguado,* 1990; *Dettinger et al.,* 2004; *Lundquist et*

al., 2015], which can provide relatively long temporal records, but spatially incomplete characterizations of orographic processes. Furthermore when gridded datasets have been used, they were generally temporally sparse and/or (spatially) coarse: a single high-resolution snapshot in time over a limited domain [e.g. *Kirchner et al.,* 2014], coarse-resolution (several kilometers) gridded datasets and climate models [e.g. *Colle,* 2004; *Galewsky and Sobel,* 2005], etc. Coarse resolutions smooth out the heterogeneities (e.g. elevation) that control the variability of snowfall, snow states, and orographic processes over complex terrain [*Leung and Ghan,* 1995; *Cayan et al.,* 2008]. Hence coarse resolutions, point-scale measurements, and temporal sparseness can result in an incomplete picture of the high spatiotemporal variability of montane snowfall.

To overcome these limitations, we used a new multi-decadal, high-resolution distributed SWE reanalysis over the western Sierra Nevada [*Margulis et al.,* 2016] to yield better insight into orographic enhancement, the inter-annual variability of orographically-driven cumulative snowfall (CS) gradients, and the drivers of orographic processes in cold-season snowfall accumulation. Previous studies have not been able to capture the inter-annual variability of orographic snowfall at the basin-scale across an entire mountain range (due to limitations in data and resolution) nor have they concentrated on a thorough comparison of snowfall gradients among all windward basins in the Sierra Nevada (Figure 3.1a). A detailed climatology of orographic CS gradients does not currently exist at the range-scale nor have wet-year/dry-year implications in CS gradients been explored. Herein, the CS was defined as the integrated amount of snowfall occurring over the course of the accumulation season.

This paper therefore extends previous work to better understand the inter-annual and spatial variability of orographically-driven snowfall gradients at high-elevations across the Sierra Nevada by answering the following questions: 1) How is orographically-driven snowfall manifested across the windward (western) side of the Sierra Nevada? 2) How can the shapes of

the cumulative snowfall versus elevation curves be characterized (e.g. slope, maximum, etc.) and what factors influence their shapes? 3) How and to what extent do orographic gradients vary spatially and inter-annually? 4) What characterizes a "wet" versus "dry" year in the Sierra Nevada in terms of orographically-driven cumulative snowfall?

3.2 Wintertime Atmospheric Conditions Driving Orographic Enhancement

The Sierra Nevada receives the majority of its seasonal snowfall from a few large snowstorms each year, leading to high inter-annual variability in CS and SWE across the range [*O'Hara et al.*, 2009; *Lundquist et al.*, 2015; *Huning and Margulis*, in review, hereafter *HM17*]. With the rapid snowfall accumulation rates over the Sierra Nevada [*Serreze et al.*, 2001; *Lundquist et al.*, 2015; *HM17*], the heavy reliance on snowmelt across California [*Bales et al.*, 2011; *Downing*, 2015; *Rosenthal and Dozier*, 1996; etc.], and shifts in peak streamflow/melt due to climate change [*Cayan et al.*, 2001; *Mote et al.*, 2005; *Barnett et al.*, 2005; *Kapnick and Hall*, 2010], it is important to investigate the processes that lead to the wintertime snowfall accumulation across the Sierra Nevada, and in particular, how orography enhances snowfall accumulation.

Figure 3.2 presents a simplified picture of factors that tend to favor orographic enhancement during the wintertime. Moisture must be available for orographic precipitation to occur (Figure 3.2a). Even if all other factors promote orographic enhancement, without moisture, clouds will not form and precipitation will not be generated. Higher wind speeds promote greater orographic enhancement [*Luce et al.*, 2013] because they result in larger vertical uplift velocities when encountering an obstacle (Figure 3.2b). Mountains with higher peak altitudes are more favorable for enhancement than lower mountains or hills because greater uplift is possible

(Figure 3.2c). For the highest mountains, the elevation corresponding to the maximum CS ($z_{CS\max}$) is typically reached before the mountain peak ($z_{\max}$). In lower ranges however, this elevation may occur at the peak or on the leeward side of the mountain due to spillover. While steeper slopes force uplift at a greater rate than a gradual slope, there is also greater potential for gravitational redistribution of the snow (e.g. avalanching, *Grünewald et al.,* 2014) causing lower enhancement to be observed as depicted in Figure 3.2d. Also, terrain aspects facing into the prevailing wind tend to be more favorable for orographic enhancement than hillslopes oriented away from the prevailing wind (Figure 3.2e).

The Sierra Nevada provides a suitable domain for studying orographic enhancement because the (western) basin-average aspects generally face into the wind with minimal upwind obstacles (Figure 3.1a; *Grubišić et al.,* 2005). Previous studies have shown the importance of atmospheric rivers (e.g. *Ralph et al.,* 2006; *Guan et al.,* 2010) and the Sierra Barrier Jet (SBJ; e.g. *Lundquist et al.,* 2010; *Hughes et al.,* 2009, 2012) in determining the precipitation/snowfall patterns across the Sierra Nevada. Long, narrow, moisture-rich low-level jets known as atmospheric rivers (ARs) promote orographic precipitation when they interact with topography. On average, ARs yield an estimated 30-40% of the CS across the Sierra Nevada annually [*Guan et al.,* 2010]. SBJs are also low-level jets that form parallel to the western side of the range (Figure 3.2f). They transport moisture northward, impacting the distribution of precipitation across the Sierra Nevada when stable air masses slow and cannot ascend the western slope (blocking) [e.g. *Lundquist et al.,* 2010; *Neiman et al.,* 2013]. Precipitation can also result from enhanced vertical uplift of air masses that are capable of ascending the terrain/barrier. Nonetheless, we do not focus on specific storm mechanisms or meteorological events because this paper provides a seasonal study as opposed to an event-based analysis. Therefore, our analysis considers all storm mechanisms (e.g. frontal systems, ARs, etc.) that yield snowfall

across the Sierra Nevada. Herein, we analyze atmospheric quantities such as integrated vapor transport (IVT), integrated water vapor (IWV), etc. during storm periods and ARs, SBJs, etc. are implicit in the moisture and wind fields to the extent that the atmospheric regional reanalysis (described below) represents these events.

Previous studies utilizing precipitation information from in situ observations [*Pandey et al.,* 1999; *Dettinger et al.,* 2004; *Lundquist et al*,. 2015] found that southwesterly winds tend to correspond to the largest storm events over the Sierra Nevada, while westerly/northwesterly winds generally yield greater orographic enhancement. *Lundquist et al.* [2015] showed that the heightened enhancement observed during northwesterly winds results from snow pillows recording increases in SWE while only minimal increases were recorded at precipitation gauges. They found that this could result in up to six times more mountain precipitation than valley precipitation with northwesterly winds as opposed to ~2-3 times more with southwesterlies. Since climatologies in California tend to be dominated by more total precipitation during southwesterlies, this can impact the accuracy of datasets that are trained on climatologies (Lundquist et al. 2015). The snowfall dataset used herein was not conditioned on climatologies and thus should yield robust estimates of orographic gradients via a probabilistic snow reanalysis framework (Margulis et al. 2016).

3.3 Data and Methods

3.3.1 Snowfall Dataset

For the 14 study basins along the windward side of the Sierra Nevada (Figure 3.1a), snowfall was defined as increases in the 90-m daily SWE fields derived from the snow reanalysis [*Margulis et al.,* 2016]. This SWE reanalysis was generated using the process briefly described here and extensively documented in *Margulis et al.* [2015]. An ensemble of meteorological

forcings derived from the National Land Data Assimilation (NLDAS-2, Xia et al. 2012) dataset was used to drive a snow model and generate prior state estimates. These estimates were seasonally conditioned on Landsat fractional snow covered area images within a Bayesian data assimilation framework to yield posterior estimates such as daily, 90-m SWE fields.

The land surface model used within this framework utilized a fixed air temperature threshold of 2°C [*Lundquist et al.,* 2008] to classify precipitation as either rain or snow at a given time. This simplification would likely have the largest impact on lower elevations that are more prone to experiencing a mixture of rain and snow during a storm due to their warmer temperatures. Given this framework and that the analysis herein focuses on snowfall gradients, not rainfall or total precipitation gradients, an air temperature dependence is removed during snowstorms when only considering air temperatures that yield snowfall and not melt or rainfall.

The SWE reanalysis was extensively verified for CS over 31 accumulation seasons in the Sierra Nevada with more than 2600 station years of snow pillow observations [*HM17*] and for peak SWE over the same time period [*Margulis et al.,* 2016]. *HM17* demonstrated that the SWE reanalysis could be utilized to examine snowfall accumulation across the Sierra Nevada by verifying the seasonal CS and snowfall timing with observations over the range. They found a root-mean-square error (RMSE) and mean error (ME) of 4 cm and -2 cm, respectively, for the median seasonal CS across all stations relative to observations. A negative ME indicates an underestimation of CS relative to observed. As expected, when all stations and years were considered, the RMSE and ME were larger (12 cm and -4 cm, respectively). Although the ME indicates a negative bias, the bias is minimal over the course of a season and differences between the 90-m CS and point-scale observations are expected due to spatial disparities and representativeness issues [*HM17*].

3.3.2 Orographic Gradients

The orographic gradient (β) was defined as the rate of increase in CS with elevation. Gradients serve as robust metrics for quantifying orographic distributions of CS since they not only quantify the difference in magnitude of CS, but they also account for elevational differences. Unlike an orographic ratio [e.g. *Lundquist et al.*, 2015] of CS at higher elevations to that observed at lower elevations, β does not vary depending on which two points are selected along an elevational transect. Two locations separated by a smaller elevational difference would likely yield significantly different orographic ratios than two separated by a larger elevational difference. However, a single orographic gradient, β, governs the CS across all of these locations. Gradients fully leverage the spatial nature of the underlying CS information to explicitly and robustly describe the distribution of CS across a watershed.

It is important to emphasize that herein snowfall is described in units of equivalent water depth and should not be confused with snow depth. Moreover CS, as opposed to SWE on the ground at a specified time, is used throughout this paper to prevent the introduction of artificially large gradients if lower elevations have undergone ablation when higher elevations are continuing to accumulate SWE at a given time. This study was constructed to minimize the air temperature impact on orographic CS gradients by eliminating intermittent melt effects during the accumulation season. Rather than assuming that the peak SWE field was representative of the total accumulated winter snowfall, CS was computed by integrating snowfall accumulated throughout the season similar to *HM17*. Although *HM17* quantified CS over the entire Sierra Nevada, they focused on accumulation rates, while herein we investigate orographic CS gradients and enhancement across the windward basins.

3.3.2.1 Construction of Orographic CS Curves

A minimum daily snowfall (S) of 0.254 cm [*Serreze et al.,* 2001] was used herein to remove negligible increases in SWE (i.e. $S = \Delta SWE \geq 0.254\text{cm}$). Moreover, to prevent exaggerating orographic gradients with the inclusion of pixels with very low or no seasonal snowfall accumulation, we only considered pixels j that received at least 2 cm of CS by the end of a given season as defined by:

$$CS_j = \sum_{t=1\,Nov}^{DOP} S_j(t) \geq 2\text{cm} \tag{3.1}$$

Analysis was performed at high-elevations (above the average 1500 m snow line) during the cold season, November through the basin-average day-of-peak (DOP) SWE (as denoted in Eq. (3.1)), for each watershed over 31 water years (WYs; 1 October-30 September) 1985-2015. As shown in Figure 3.1, we divided the Sierra Nevada into the northwest (NW) and southwest (SW) to elucidate the distinct precipitation regimes of the northern Sierra Nevada (which tends to receive more precipitation) and the higher elevation southern Sierra Nevada. All land pixels in the western (W) basins (Figure 3.1a) were considered herein. The gridded data was divided into 100-m elevation bins where bins with <0.5% of the total number of pixels in the basin (above 1500 m) were neglected to remove the potential for relatively few pixels dictating orographic relationships [*Grünewald et al.,* 2014]. Based on the combination of the seasonal CS and elevation bin criteria above, different numbers of pixels and bins were used annually in computations to account for fluctuations in the snow line.

Since a single linear fit does not necessarily describe the orographic snowfall accumulation observed across different regimes [*Grünewald et al.,* 2014], herein a piece-wise least squares regression, using a maximum of three line segments, was applied to the CS-elevation curves. These elevational relationships for each basin were derived using mean values

within each bin. The segments were fit to the data between: 1) the lowest elevation and ~2500 m, 2) ~2500 m and the elevation corresponding to the 31-year average maximum CS ($\overline{z}_{CS\max}$), and 3) $\overline{z}_{CS\max}$ and the maximum elevation ($z_{\max}$). Not all three segments (within elevation zones EZ_i , where $i = 1\text{-}3$) exist for each basin; however where possible, the 31-year average orographic CS gradient is denoted as $\overline{\beta}(EZ_i)$. The approximate upper bound of 2500 m was chosen for EZ_1 because it captures the linear relationship at the lowest elevations considered. While nearly all basins span these elevations, some do not have a noticeable fraction of area above 2500 m (based on the 0.5% threshold described above). Therefore, the elevation of the binned data with a mean value closest to 2500 m was used as the upper bound of EZ_1. Figure 3.1b shows the spatial distribution of the elevation zones. Elevation maps (Figure 3.1) and other physiographic characteristics were derived from *Margulis et al.* [2016].

3.3.3 Wet and Dry Year Selection

An important missing piece in understanding the inter-annual variability of CS is a thorough assessment of wet-year and dry-year orographic CS and how synoptic atmospheric conditions in the Sierra Nevada contribute to orographic enhancement at the basin-scale. To examine the potential drivers of orographic enhancement (e.g. moisture transport, wind speed/direction, etc.) and understand the inter-annual variability of orographically-driven snowfall, the 31 years were sub-divided into wet and dry years following *HM17*, and the same years were analyzed herein. Wet years include WYs 1986, 1993, 1995, 1998, 2005, 2006, 2008, and 2011 and dry years include WYs 1987, 1988, 1990, 1992, 1994, 2001, 2007, and 2012-2015. The classifications were defined based on the integrated basin-averaged CS across the range for consistency across all basins. Although the number of wet years (eight) and dry years (eleven)

differ, the orographic features remain similar to when an equal number of wet and dry years are analyzed.

3.3.4 Orographic Enhancement

Throughout this paper, we investigate the distribution of CS with elevation and how CS varies spatially and inter-annually across the range. As such, we defined "orographic enhancement" corresponding to conditions where there were increases in CS with elevation or conditions where higher values of the CS gradients were observed relative to lower ones. This latter form of the definition can therefore be applied to specific years, elevation zones, or regions. Furthermore for each EZ, the degree of orographic enhancement exhibited during wet years relative to dry years was defined as the ratio $\overline{\beta}_w / \overline{\beta}_d$, where $\overline{\beta}_w$ and $\overline{\beta}_d$ are the average wet-year and dry-year gradients, respectively.

3.3.5 Snowstorm Conditions

3.3.5.1 Snowstorm Characterization

We used the basin-wide snowstorms that were identified in *HM17* to investigate potential controls on the inter-annual variability of orographic snowfall processes. Using the SWE reanalysis, *HM17* defined snowstorms to be those days during the accumulation season that contributed at least 1% of the integrated seasonal CS volume across a basin at the highest elevations (i.e. elevations above the 75^{th}-percentile). Consecutive days satisfying this condition were grouped into a single event. Their approach was designed to capture the largest events of the season that most-significantly drive CS. Those same snowstorm periods were used herein to assess the synoptic storm features that lead to differences in orographic enhancement and characterize wet versus dry years throughout the domain. As noted by *HM17*, basin-wide snowstorms were identified to account for differences in storm track location/timing and local

interactions. We defined the "leading event" for a given year as the snowstorm that yielded the largest integrated CS volume over a basin.

3.3.5.2 Synoptic Atmospheric Conditions

Synoptic atmospheric conditions during snowstorm events were diagnosed with the North American Regional Reanalysis (NARR; *Mesinger et al.*, 2006). NARR was selected for its relatively high resolution (3-hourly, 32-km) and its connection to the near-surface fields used to force the land surface model in *Margulis et al.* [2016] (i.e. NLDAS-2). It is important to emphasize that the SWE reanalysis was forced by precipitation derived from NLDAS-2 (which was derived from observational data via the Climate Prediction Center (CPC) precipitation gauge network). NARR was used herein to diagnose atmospheric fields such as IVT, etc.; however, as shown in *Hughes et al.* [2012], NARR may not be able to fully represent features such as the SBJ.

NARR grid cells overlapping each watershed were identified and atmospheric variables were averaged to characterize basin-wide atmospheric dynamics. IVT, which accounts for both the wind field (direction and speed) and humidity in the overlying atmosphere, was computed from the surface to 100 hPa to characterize typical snowstorm conditions. Based on *Lavers et al.* [2012], the magnitude of the IVT vector is given by:

$$IVT\left[\text{kgm}^{-1}\text{s}^{-1}\right] = \sqrt{\left(\frac{1}{g}\int_{p_{sfc}}^{10{,}000\,\text{Pa}} qu\,dp\right)^2 + \left(\frac{1}{g}\int_{p_{sfc}}^{10{,}000\,\text{Pa}} qv\,dp\right)^2} \tag{3.2}$$

where g is the acceleration due to gravity in m s^{-2}, p_{sfc} is the surface pressure in Pa, q is the specific humidity in kg kg^{-1}, u and v are the zonal and meridional wind in m s^{-1}, and p is the pressure. The direction of the IVT vector is determined using geometric relationships. The magnitude of the horizontal vapor transport along an atmospheric profile is defined as:

$$VT\left[\mathrm{kg\,kg^{-1}\,m\,s^{-1}}\right]=\sqrt{\left(\frac{1}{g}qu\right)^2+\left(\frac{1}{g}qv\right)^2} \tag{3.3}$$

We computed the IWV between the same levels used for IVT from NARR as follows:

$$IWV\left[\mathrm{mm}\right]=\frac{1000\,\mathrm{mm\,m^{-1}}}{\rho_w g}\int_{p_{sfc}}^{10{,}000\,\mathrm{Pa}} q\,dp \tag{3.4}$$

where ρ_w is the density of water in kg m^{-3}. Zonal winds at 700 hPa (u_{700}) were also obtained from NARR.

3.4 Results and Discussion

3.4.1 Shape of Orographic CS Curves

To characterize the general shape of the CS-elevation curves, we first focus on the 31-year average (black curve) for each of the basins (Figure 3.3). For reference, the histogram indicates the (static) elevational distribution of area within each basin. As demonstrated in Figure 3.3, NW basins are characterized by increasing orographic curves that reach their maximum in their highest elevation bin. They do not exhibit a negative slope after a maximum is reached like the majority of higher elevation SW basins. Only American, Mokelumne, and Stanislaus in the NW extend beyond EZ_1 and into EZ_2 (Figures 3.1b and 3.3). At the lowest elevations, every basin has a strong linearly increasing CS-elevation relationship. By definition, CS continues to increase linearly with elevation for each of the basins in EZ_2 (shaded gray, Figure 3.3). Only six SW basins have orographic curves that extend into EZ_3 (Figures 3.1b and 3.3) where each exhibits a negative slope. As such, the basin-wide shapes of the climatological CS-elevation curves found in the Sierra Nevada can be classified into two groups: 1) increasing and 2) increasing to a maximum and then decreasing.

As demonstrated in Figure 3.3, the elevation of the (31-year) maximum CS occurs at the highest elevations for all NW basins and Merced. Consequently, the elevation of $\bar{z}_{CS\max}$ for the remaining six SW basins is governed by other physical processes that dominate the higher elevations. In these six SW basins, $\bar{z}_{CS\max}$ ranges from ~2850 m (Tule) to 3650 m (Kern), which is similar to values found in literature (e.g. 3300 m, *Kirchner et al.,* 2014; ~2000-3000 m (sub-catchment scale) and up to ~3400 m (transect-scale), *Grünewald et al.,* 2014). Although values of $z_{CS\max}$ have been theoretically estimated [e.g. *Alpert,* 1986] or observed, previous studies have not shown whether these elevations were relatively constant for basins over long records (i.e. multiple decades) as shown here in Figure 3.4. For a given basin, $z_{CS\max}$ has low inter-annual variability and is confined to relatively few elevation bins concentrated around $\bar{z}_{CS\max}$. Figure 3.4 indicates that given the geometry of a basin, $z_{CS\max}$ is relatively constant at the seasonal-scale. We hypothesize that a combination of factors dictate $z_{CS\max}$, including: A limited moisture holding capacity at high altitudes that reduces the amount of snowfall that occurs (i.e. atmospheric moisture is exhausted, e.g. *Kirchner et al.,* 2014). Gravitational processes [*Grünewald et al.,* 2014] and wind redistribution also contribute to negative slopes in EZ_3 across these highest elevations that are more exposed and less vegetated [*Margulis et al.,* 2016]. Since the gradients observed in EZ_3 were constructed with fewer pixels, primary focus is on EZ_1 and EZ_2 below.

3.4.2 Characterization of Orographic Gradients and Enhancement

3.4.2.1 Long-term Average Orographic Gradients

Overall, the largest orographic gradients occur in EZ_1 across the Sierra Nevada (Table 3.1 and Figure 3.3). Table 3.1 indicates that five basins have 31-year averaged gradients ≥7.0 cm

SWE/100 m elevation in EZ_1, with the steepest gradient found in Cosumnes (7.5 cm/100 m). Tuolumne and Kings display the smallest 31-year average gradients in EZ_2 of ~1.1-1.4 cm/100 m. Although the orographic curves continue to increase from EZ_1 to EZ_2, a reduction in the rate of orographic enhancement (i.e. $\bar{\beta}(EZ_2) < \bar{\beta}(EZ_1)$) is observed. $\bar{\beta}(EZ_1)$ is ~1.3 (Tule) to 6.5 (Tuolumne) times larger than $\bar{\beta}(EZ_2)$. On average, this ratio is ~2.5. The 31-year average gradients in EZ_3 range from -0.3 (Kaweah) to -2.8 cm/100 m (Tule).

Based on the 31-year averages in EZ_1 and EZ_2 in Table 3.1, the NW exhibits greater orographic enhancement than the SW basins by ~1 cm/100 m. However when comparing individual basins in the two regions, $\bar{\beta}(EZ_1)$ can differ on the order of 4 cm/100 m. The negative slopes in EZ_3 observed in the SW have the smallest absolute values of all gradients. The magnitudes of the orographic gradients tend to decrease with elevation from EZ_1 to EZ_3. Note that this does not always hold for an individual year (Figure 3.5).

3.4.2.2 Inter-annual Variability of Orographic Gradients

Over the 31 years of orographic gradients presented in Figure 3.5, negative slopes did not occur at the lowest elevations (Figure 3.5a). Although uncommon, some basins/years did exhibit small negative gradients in EZ_2 (Figure 3.5b) as well as positive gradients in EZ_3 (Figure 3.5c). Across all years in Figure 3.5, the steepest (magnitude) gradient for each basin ranged from 8.8 (Feather, WY 2006) to 15.0 cm/100 m (Cosumnes, WY 1986) in EZ_1, 5.6 (Kings, WY 1986) to 15.2 cm/100 m (Tule, WY 1986) in EZ_2, and -2.7 (San Joaquin, WY 1995) to -7.6 cm/100 m (Tule, WY 2010) in EZ_3. Out of the steepest gradients for each basin across EZ_1 and EZ_2, ~58% of these gradients exceeded 10 cm/100 m. About 63% of the gradients with the smallest magnitude for each basin in these two zones had magnitudes <1 cm/100 m (Figures 3.5a-b).

Further discussion of the wet-year and dry-year gradients and their ratios (i.e. $\overline{\beta}_w / \overline{\beta}_d$) is presented below.

3.4.3 What Makes a Wet Versus Dry Year in the Sierra Nevada?

HM17 showed that, on average, 11 snowstorms occur annually in the Sierra Nevada with dry years experiencing approximately four fewer snowstorms and roughly 30% fewer storm snow days than wet years. They determined that, on average, large snowstorms contribute ~83-93% of the seasonal CS within a basin. Hence, we used the snowstorm periods from *HM17* to examine synoptic drivers of elevational gradients in CS and understand how synoptic features impact wet-year and dry-year orographic CS accumulation.

3.4.3.1 Representative Average Snowstorm Conditions

Figure 3.6 compares the seasonal and average snowstorm characteristics of two representative basins, Mokelumne (NW) and Kaweah (SW), during WY 1986 and 2015. The basins exhibit the typical CS-elevation relationships and snowstorm characteristics observed in the NW and SW. These two years generally represent those with the greatest and least orographic enhancement (i.e. highest/lowest gradients) over the range in EZ_1 (Figure 3.5a) and correspond to a wet and dry year, respectively. Figure 3.6a depicts the elevational variation of CS during WYs 1986 (blue) and 2015 (red) for both basins and indicates that a stark contrast between wet-year and dry-year orographic CS gradients exists. WY 1986 yielded orographic gradients of 14.5 (Mokelumne) and 11.4 cm/100 m (Kaweah) in EZ_1 (as shown in Figures 3.5a and 3.6a) while WY 2015 only yielded 2.7 (Mokelumne) and 1.4 cm/100 m (Kaweah). Hence, WY 1986 had orographic gradients ~5.4 and 8.5 times larger than during 2015 for Mokelumne and Kaweah, respectively. Inter-annual variability of orographic CS gradients is further examined below.

Synoptic features (i.e. u_{700}, IVT, and IWV) are presented in Figures 3.6b-d for the average snowstorm and leading snowstorm conditions during WY 1986 and 2015 across Mokelumne and Kaweah. Although there is variability between the synoptic conditions associated with each basin, the differences between a year with strong vs. weak orographic enhancement are highlighted. The zonal wind speeds are higher in both basins averaged across storms (i.e. seasonal-scale) and at the leading snowstorm-scale during the wet year (Figure 3.6b). Similarly IVT is larger in 1986 than in 2015 (Figure 3.6c) for both basins. While u_{700} and IVT are generally larger during wet years than dry years, Figure 3.6d suggests that IWV is not necessarily as strong of an indicator of wet-year enhancement as the other two synoptic variables. Not only does IWV show minimal variability between years, the IWV is actually larger for both the average and leading snowstorm conditions in Mokelumne during 2015. The opposite is observed in Kaweah. Furthermore across the Sierra Nevada, stronger and statistically significant correlations between β and IVT were observed as opposed to correlations between β and IWV (not shown), which often were not statistically different from zero since $p > 0.05$. Rutz et al. (2014) similarly found precipitation to be more strongly correlated to IVT than to IWV over the mountainous western U.S. during the cold season. Hence, further quantification of synoptic conditions focuses on u_{700} and IVT is expanded to each watershed below.

3.4.3.2 Wet-year and Dry-year Orographically-driven CS

Figure 3.7 extends the analysis of orographic CS to all wet and dry years across the 14 basins and demonstrates how the snowstorm characteristics discussed above manifest themselves in wet-year and dry-year orographic enhancement. Wet years are more orographically enhanced than dry years, which is evidenced by the lack of a simple vertical translation in the CS-elevation curve between wet and dry years (Figure 3.7). In other words, Figure 3.7 demonstrates that the

average dry-year curve (red) is not simply shifted upward along the y-axis because the snowfall distribution varies between wet and dry years. If such a shift/translation took place, this would preserve the slope or orographic gradient of the dry-year curve while yielding the average wet-year curve (blue) with a higher CS. Rather, there is an increase in $\bar{\beta}_w$ that may be considered a "scaling" or "stretching" of the dry-year curve because the orographic distribution of CS highly varies inter-annually. As shown in Figure 3.7, the greater orographic enhancement occurring during wet years can be represented by the relative rate of enhancement or the ratio of the wet to dry year gradients exceeding unity (Table 3.1). This is observed across all basins (except Tuolumne) in both EZ_1 and EZ_2.

As summarized in Table 3.1, the largest values of $\bar{\beta}_w$ and $\bar{\beta}_d$ in EZ_1 were observed to be 11.8 (Tuolumne) and 5.5 cm/100 m (Cosumnes), respectively. The SW has larger orographic gradients than the NW Sierra Nevada in EZ_1 during wet years; however, this is reversed in the next elevation zone and during dry years. The relative rate of enhancement (i.e. $\bar{\beta}_w / \bar{\beta}_d$) in the SW is ~3.1 and 2.1 in the first two zones whereas values of 2.0 and 2.4 occur, respectively, in the NW. Thus the degree of wet-year enhancement varies by region and elevation zone. Overall, the western Sierra Nevada experiences roughly twice as much enhancement during wet years as in dry years in EZ_1 and EZ_2. The rate of decline in CS is ~10 times larger during wet years in EZ_3 in the SW. However, neglecting the extremely large ratio (Kern) and negative ratio (Kaweah) in Table 3.1, the average ratio is ~3.1. At the individual basin scale, the relative rate of enhancement is generally lower in EZ_2 than EZ_1 indicating that elevations below ~2500 m tend to be relatively more orographically enhanced.

In Figures 3.5a-b and 3.7, wet years dominate the largest orographic gradients observed in EZ_1 and EZ_2 across all watersheds. Considering the largest gradient for each basin in these

two elevation zones, WY 1986 produced ~67% of the largest gradients. Overall, wet years yielded ~87% of the steepest gradients and they produced all but one of the steepest gradients in EZ_1 and EZ_2. Similarly, dry years make up the largest fraction of years with the most gradual CS-elevation increases for each basin (Figure 3.5). They account for well over the majority of these gradients across elevation zones with WYs 2001 and 2015 accounting for the largest number of dry years. Dry years did not produce any of the steepest gradients and only once did a wet year yield one of the smallest magnitude slopes for a basin (American in WY 2008, Figure 3.5b).

3.4.4 Attribution of Orographic Enhancement

3.4.4.1 Horizontal Moisture Transport and Wind Patterns

Large-scale moisture transport and wind predominantly come from the southwest and west during snowstorms across the Sierra Nevada (Figure 3.8). The basin-average terrain aspect of the majority of basins corresponds to southwest/west-facing terrain (dashed line in Figure 3.8), while Kern and Feather have south-facing basin-average terrain aspects. Therefore, 12 of the 14 basins have average terrain aspects that are more prone to being aligned with the dominant winds that transport moisture to this range (i.e. facing into the wind). Note that while the basin-average terrain aspect of the Upper Sacramento is similar to the other basins, its overall configuration is different (Figure 3.1a). Lower elevations (in particular) in both Kern and Feather tend to be more sheltered or obstructed by terrain such that localized rain shadows can form. This is manifested by these two basins having the lowest orographic gradients in EZ_1 over each averaging period (Table 3.1). Furthermore Figure 3.5a shows that at these lowest elevations, both basins have the smallest maximum gradients out of all basins at 8.8-9.0 cm/100 m. While alignment between the prevailing wind direction and the terrain aspect would be expected to

provide the greatest orographic enhancement (Figure 3.2e), there tends to be a relatively narrow range of prevailing IVT directions during the snowstorms analyzed herein (Figure 3.8). Thus, "perfect" alignment is not necessarily achieved across basins; however, the basin-average terrain aspects generally face into the prevailing wind field, which promotes orographic enhancement.

Figure 3.8 presents the distribution of prevailing transport directions during all snowstorms in a basin for wet and dry years in lighter shades of blue and red, respectively. It indicates that the percent of storms from the SW is often greater during wet years; however, directions do not greatly vary between years. While the IVT directions may be similar, the IVT magnitudes (and inherently wind speeds) can greatly differ between storms and years, leading to differences in orographic enhancement as shown in Figures 3.3 and 3.5-3.7 and further discussed below. Figure 3.8 also demonstrates that the predominant direction that leading snowstorms (darker/thicker curves) originate from is the same direction as when all snowstorms (lighter/thinner curves) are considered; however, a larger percentage of the leading snowstorms tend to originate from these prevailing directions than when all storms are considered. Since the snowstorm definition [*HM17*] targeted the largest snowstorms of the season, it is not surprising that southwesterly winds dominate the snowstorm record, given previous literature [e.g. *Lundquist et al.,* 2015]. Overall, transport from the SW yields the largest snowstorms of the season that have high water vapor and favorable alignment with the terrain aspect, and thereby promote orographic enhancement.

Maps of average IVT conditions during snowstorms over the range are presented in Figure 3.9. They depict both the magnitude and direction of IVT ranging from multi-year composites of average storm conditions in Figure 3.9a to single events in Figure 3.9d. Across each set of percent difference maps (rightmost maps in Figures 3.9a-d), wet years and their leading snowstorms have higher IVT than dry years with large relative differences observed

along the western basins. Although the directions of the vectors are markedly similar between the leading storm composites in Figure 3.9b, the percent differences relative to the dry years are large (32.7-104.4%). The greatest relative differences between wet and dry years are evident at the leading storm-scale with a maximum difference of 219.4% (Figure 3.9d). Even when the IVT vectors are similar in the northernmost basins in WY 1986 and 2015 (Figure 3.9c), the storm conditions still indicate higher overall IVT during the wet year, which had more storms (and longer integrated storm duration) than 2015 (HM17). Therefore, while these maps (near/over the western basins) are consistent with the dominant transport directions identified in Figure 3.8, they provide additional information about the variability of IVT magnitudes and storm directions across the range within the broader context of California.

3.4.4.2 Atmospheric Synoptic Features and Orographic CS Gradients

Of the average synoptic snowstorm conditions considered above (i.e. u_{700}, IVT, and IWV), u_{700} wind speeds and IVT magnitudes are further investigated to better understand the drivers of orographic enhancement and how these synoptic features impact the inter-annual variability of orographic gradients across the Sierra Nevada. The above discussion and Figures 3.2, 3.6, and 3.9 suggest strong correlations between orographic gradients and both IVT and u_{700}. For the abovementioned reasons, our primary focus is on both EZ_1 and EZ_2, which make up the largest fraction of the area among basins.

Table 3.2 shows the correlation coefficients between seasonal orographic CS gradients in each elevation zone and u_{700} and IVT for the 14 basins. The stronger correlations overall (boldface) generally occur between the orographic gradients and IVT, with higher correlations most evident in EZ_2. Roughly half of the largest correlation coefficients in EZ_1 are split between β and u_{700} (column a) and β and IVT (column b). In the northernmost (Feather, Yuba,

and American) and southernmost (Kings, Kaweah, and Tule) basins in EZ_1, correlations between β and u_{700} are larger than those between β and IVT, while the opposite is generally observed in the central Sierra Nevada. The correlations in Table 3.2 are statistically significant, with only two basins (Cosumnes and Kern) having weak (statistically insignificant) correlations in EZ_1. The weakest correlations found in EZ_1 were in Kern, which likely resulted from its North-South orientation that largely shelters the lowest elevations from the prevailing wind. In addition, the complex terrain upwind of Kern (e.g. Kaweah and Tule basins to the west of Kern, etc.) may also impact the correlations observed for Kern. Both Cosumnes and Kern have the weakest correlations between CS and slope (not shown), which may contribute to the correlations between the synoptic features and CS gradients not being statistically different from zero in Table 3.2. On average, the β and IVT correlations are larger in EZ_2 than those associated with u_{700}.

The combination of higher wind speeds and higher precipitable water leads to increased IVT, which enhances orographic CS gradients (Table 3.2). To illustrate this, Figure 3.10 shows the average wet-year (blue line), dry-year (red line), and 31-year (dashed line) snowstorm horizontal vapor transport profiles above the surface for each basin. The inter-annual variability in the wet-year and dry-year profiles is demarcated by the shaded regions in their respective colors. These profiles represent average atmospheric profiles during a broadly defined set of snowstorms. While the snowstorms considered herein would include specific atmospheric structures such as precipitation-intensive AR events, our analysis more generally considers both small/weak and large/intense snowfall events.

As shown in Figure 3.10, higher vapor transport occurs near or above the highest elevations in the Sierra Nevada. Moving upslope within a watershed, vapor transport “builds up”

with elevation leading to greater potential enhancement. In other words, both wind and moisture at downwind locations can have a cumulative (integrated) effect with elevation and promote orographically-enhanced CS at higher elevations. Stronger overall correlations between β and IVT are therefore observed in EZ_2 as opposed to EZ_1. In addition, we hypothesize that higher correlations are observed in EZ_2 because of the presence of the SBJ that influences the atmospheric controlling layer during the season [*Neiman et al.*, 2013]. The SW basins that have larger correlations in EZ_1 between β and u_{700} than between β and IVT (Table 3.2) tend to have lower vapor transport values than in other basins at the lowest elevations (Figure 3.10). In addition, there is often significant overlap between the wet-year and dry-year interquartile ranges for these basins (e.g. Kings, Kaweah, and Tule). Along with Feather and Yuba, they also have lower inter-annual variability in the vapor transport at these altitudes. Basins in the central Sierra Nevada exhibit the largest inter-annual variability and the strongest correlations overall (Table 3.2). The profiles in Figure 3.10 therefore explain the relationships exemplified in Table 3.2. Both moisture and sufficient wind speeds (i.e. transport mechanisms) should exist at a given location or downslope for orographic precipitation to occur.

Furthermore, humidity profiles decrease with altitude (Figure 3.11, dotted line). While the vapor transport (Figure 3.10) and wind speed profiles (Figure 3.11, blue and red) tend to exhibit a noticeable difference (or separation) between the profiles in wet and dry years, this is typically not observed in the humidity profiles (Figure 3.11, cyan and magenta), which have low inter-annual variability. Although lower elevations tend to have higher humidity, high moisture does not necessarily indicate that orographic enhancement will occur without sufficient wind speeds. This explains why IVT and u_{700} display a stronger relationship with orographic gradients than IWV. While 700 hPa corresponds to a geopotential height of roughly 3000 m,

higher u_{700} winds are generally indicative of higher zonal winds at all altitudes since wind speeds typically increase with altitude (Figure 3.11) and the westerlies are strong across California. Higher wind speeds favoring orographic enhancement were often observed during snowstorms in wet years (Figure 3.11), which supports the presence of positive correlations between u_{700} and β even at lower elevations.

Not only do these findings explain the wet-year enhancement exemplified in Figures 3.5-3.7, but also the correlations presented in Table 3.2. Thus, while wind speed and moisture are both important components in the generation of orographically-driven CS, wind speeds are more important in the Sierra Nevada. At elevations with a higher cumulative vapor transport effect (e.g. EZ_2), β tends to be more highly correlated to IVT than u_{700}. When transport is lower (Figure 3.10), the u_{700} correlations dominate in the case of the lowest elevations (Table 3.2). While Figure 3.2 depicts higher wind speed as a factor promoting orographic enhancement, IVT exerts a more complex control on orographic enhancement because it combines moisture availability (Figure 3.2a) with wind fields (Figure 3.2b). Other ranges similar to the Sierra Nevada are expected to respond likewise to higher IVT and u_{700}, which promote greater orographic enhancement and lead to wet years displaying greater enhancement than dry years.

Stronger correlations in the Sierra Nevada are generally found between the orographic gradients and u_{700} at higher elevations (i.e. EZ_2 vs. EZ_1), which is similar to *Luce et al.* [2013] who found stronger correlations between cumulative precipitation and u_{700} at higher elevations in the Pacific Northwest. As demonstrated here, higher wind speeds promote orographic enhancement at higher elevations where it can be more pronounced. At the lowest elevations, the prevailing wind has the greatest probability of being obstructed by the terrain or features such as the SBJ, which would result in localized wind patterns at these elevations that differ more from

the large-scale wind (taken as u_{700}). However as noted above, higher u_{700} is often indicative of higher wind speeds even at lower altitudes.

3.5 Conclusion

This paper utilized a high-resolution spatially-distributed snowfall dataset to investigate 31 years of orographically-driven CS gradients across 14 windward basins in the western Sierra Nevada. It provided a more comprehensive analysis of the inter-annual variability of orographically-enhanced CS, wet-year vs. dry-year enhancement, and the key drivers of enhancement than previously available for high-elevation mountain ranges. Variability in orographic gradients indicates changes in the elevational distribution of CS, which has water resources and climate change implications [*Pavelsky et al.*, 2012].

An important implication of higher wind speeds and IVT observed during wet years is that while windy conditions promote enhancement, these are the same conditions that often lead to increased under-catch by gauges/sensors [*Rasmussen et al.*, 2012]. Thus, such conditions would likely result in misrepresentations of orographic snowfall distributions that may be exacerbated by the general under-sampling of high elevations by in situ measurements. Furthermore, a warmer climate will allow the atmosphere to hold more water vapor. As a result, IVT is projected to increase in the future in the mid-latitudes along the west coast of North America [*Lavers et al.*, 2015]. *Lavers et al.* [2015] found that a potential increase in IVT of ~20-40% may occur in the wintertime, which thereby could increase orographic gradients. Our findings show that future modulation of IVT fields would have significant implications across the Sierra Nevada, altering the distribution of CS and orographic enhancement. These findings are likely extensible to other similar mountain ranges.

Insights presented herein could be used to evaluate the ability of climate models to accurately diagnose high-elevation CS gradients and distributions in montane regions. Since climate models often struggle with the representation of orographic snowfall processes, results could also be used to develop parameterizations that leverage the resolved synoptic atmospheric features in climate models (i.e. IVT and u_{700}) and their strong relationships to orographic CS gradients to better predict future orographic CS distributions across mountain ranges. Such parameterizations may also be utilized in downscaling applications from sparse station data and/or coarse gridded precipitation information to improve climate studies.

3.6 Tables

Table 3.1. Thirty-one-year, wet-year, and dry-year averaged orographic gradients ($\overline{\beta}$, $\overline{\beta}_w$, and $\overline{\beta}_d$, respectively) and the relative orographic enhancement ($\overline{\beta}_w / \overline{\beta}_d$) for each basin and elevation zone (EZ). Regional/range averages were computed using the tabulated basin values. Values in EZ_3 are the same for the SW and W since NW basins do not extend into this zone.

	$\overline{\beta}$ (cm/100 m)			$\overline{\beta}_w$ (cm/100 m)			$\overline{\beta}_d$ (cm/100 m)			$\overline{\beta}_w / \overline{\beta}_d$ (-)		
Basin	EZ_1	EZ_2	EZ_3	EZ_1	EZ_2	EZ_3	EZ_1	EZ_2	EZ_3	EZ_1	EZ_2	EZ_3
Upper Sac.	6.5	-	-	8.6	-	-	4.5	-	-	1.9	-	-
Feather	4.6	-	-	5.4	-	-	3.2	-	-	1.7	-	-
Yuba	7.0	-	-	8.5	-	-	4.9	-	-	1.7	-	-
American	7.0	3.5	-	9.4	5.3	-	4.5	2.5	-	2.1	2.1	-
Cosumnes	7.5	-	-	9.2	-	-	5.5	-	-	1.7	-	-
Mokelumne	7.0	3.8	-	9.7	5.6	-	4.6	2.0	-	2.1	2.8	-
Stanislaus	6.2	3.1	-	9.1	4.4	-	3.5	1.9	-	2.6	2.3	-
Tuolumne	7.4	1.1	-2.6	11.8	0.8	-3.5	3.7	1.3	-1.2	3.2	0.6	2.9
Merced	6.4	3.3	-	10.0	4.1	-	3.6	2.5	-	2.8	1.7	-
San Joaquin	5.6	2.2	-0.8	8.6	3.5	-1.2	3.2	1.4	-0.7	2.7	2.5	1.6
Kings	5.6	1.4	-2.3	9.3	2.1	-3.8	2.9	0.9	-0.9	3.2	2.4	4.1
Kaweah	5.9	3.0	-0.3	9.7	4.3	-0.4	3.1	2.2	0.7	3.1	1.9	-0.5
Tule	5.8	4.5	-2.8	10.3	6.6	-4.3	3.0	2.6	-1.2	3.5	2.5	3.7
Kern	3.3	2.5	-1.6	6.0	4.2	-3.4	1.9	1.4	-0.1	3.2	3.0	49.0
NW Average	6.6	3.4	-	8.6	5.1	-	4.4	2.1	-	2.0	2.4	-
SW Average	5.7	2.6	-1.7	9.4	3.7	-2.8	3.1	1.8	-0.6	3.1	2.1	10.1
W Average	6.1	2.9	-1.7	9.0	4.1	-2.8	3.7	1.9	-0.6	2.5	2.2	10.1

Table 3.2. Correlation coefficients between the seasonal orographic gradients (β) in each elevation zone and average snowstorm a) u_{700} and b) IVT in each basin. All correlations are statistically significant ($p \leq 0.05$), except where indicated. Strongest statistically significant correlations for each basin and EZ are in bold.

	a) β and u_{700}			**b) β and IVT**		
Basin	EZ_1	EZ_2	EZ_3	EZ_1	EZ_2	EZ_3
Upper Sac.	0.49	-	-	**0.52**	-	-
Feather	**0.52**	-	-	0.43	-	-
Yuba	**0.64**	-	-	0.61	-	-
American	**0.56**	**0.68**	-	0.52	0.66	-
Cosumnes	0.34[a]	-	-	0.28[a]	-	-
Mokelumne	0.64	0.77	-	**0.65**	**0.80**	-
Stanislaus	0.55	0.60	-	**0.67**	**0.72**	-
Tuolumne	0.40	0.50	**-0.52**	**0.42**	**0.68**	-0.49
Merced	**0.48**	0.67	-	0.43	**0.84**	-
San Joaquin	0.45	0.40	0.01[a]	**0.46**	**0.62**	-0.04[a]
Kings	**0.44**	0.36	**-0.58**	0.43	**0.54**	-0.51
Kaweah	**0.66**	0.45	0.04[a]	0.55	**0.54**	-0.07[a]
Tule	**0.53**	**0.59**[b]	**-0.39**	0.37	**0.59**[b]	-0.30[a]
Kern	0.25[a]	0.57	**-0.54**[b]	0.18[a]	**0.65**	**-0.54**[b]

[a] Not statistically significant ($p > 0.05$)

[b] Strongest statistically significant correlations appear in both (a) and (b) (i.e. the absolute value of the difference in correlation coefficients between column (a) and column (b) is negligible)

3.7 Figures

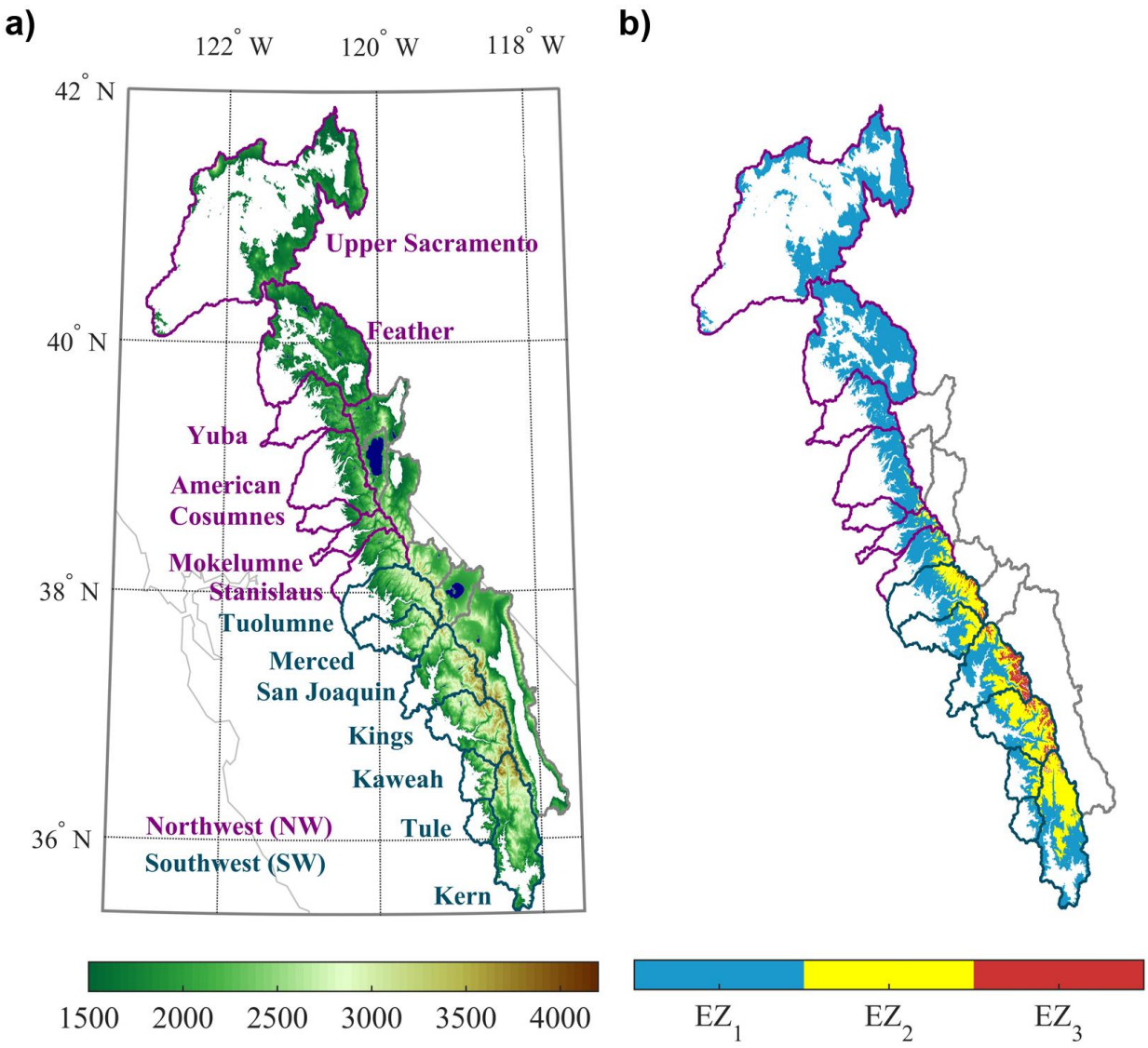

Figure 3.1. a) Elevation map (in meters) over the Sierra Nevada for elevations above 1500 m and b) distribution of the three elevation zones (EZ_i) over the western basins. Basins in the northwest and southwest are identified.

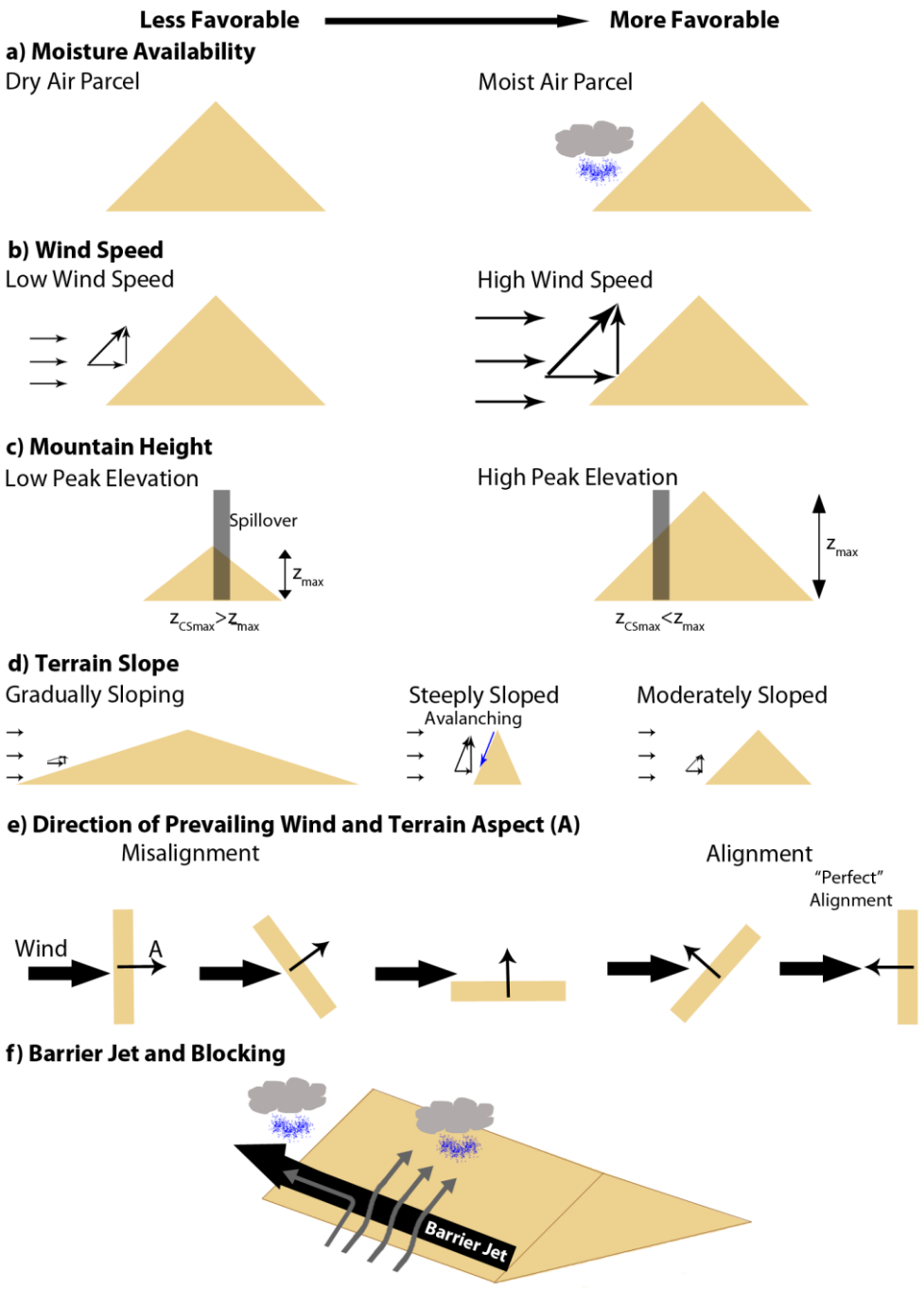

Figure 3.2. Wintertime conditions promoting orographic enhancement: a) moisture availability, b) wind speed, c) mountain height, d) terrain slope, and e) direction of prevailing wind relative to terrain aspect. z_{max} is the ridge height and $z_{CS\,max}$ is the elevation of maximum CS. More favorable conditions for orographic enhancement are presented moving toward the right. The terrain configuration is shown in brown. A vertical reflection of the terrain orientations in e) would result in the same relationships as depicted here. Configurations where the aspect of the terrain points away from the prevailing direction likely result in equally unfavorable conditions for enhancement. f) Barrier jet and blocking redistribute moisture.

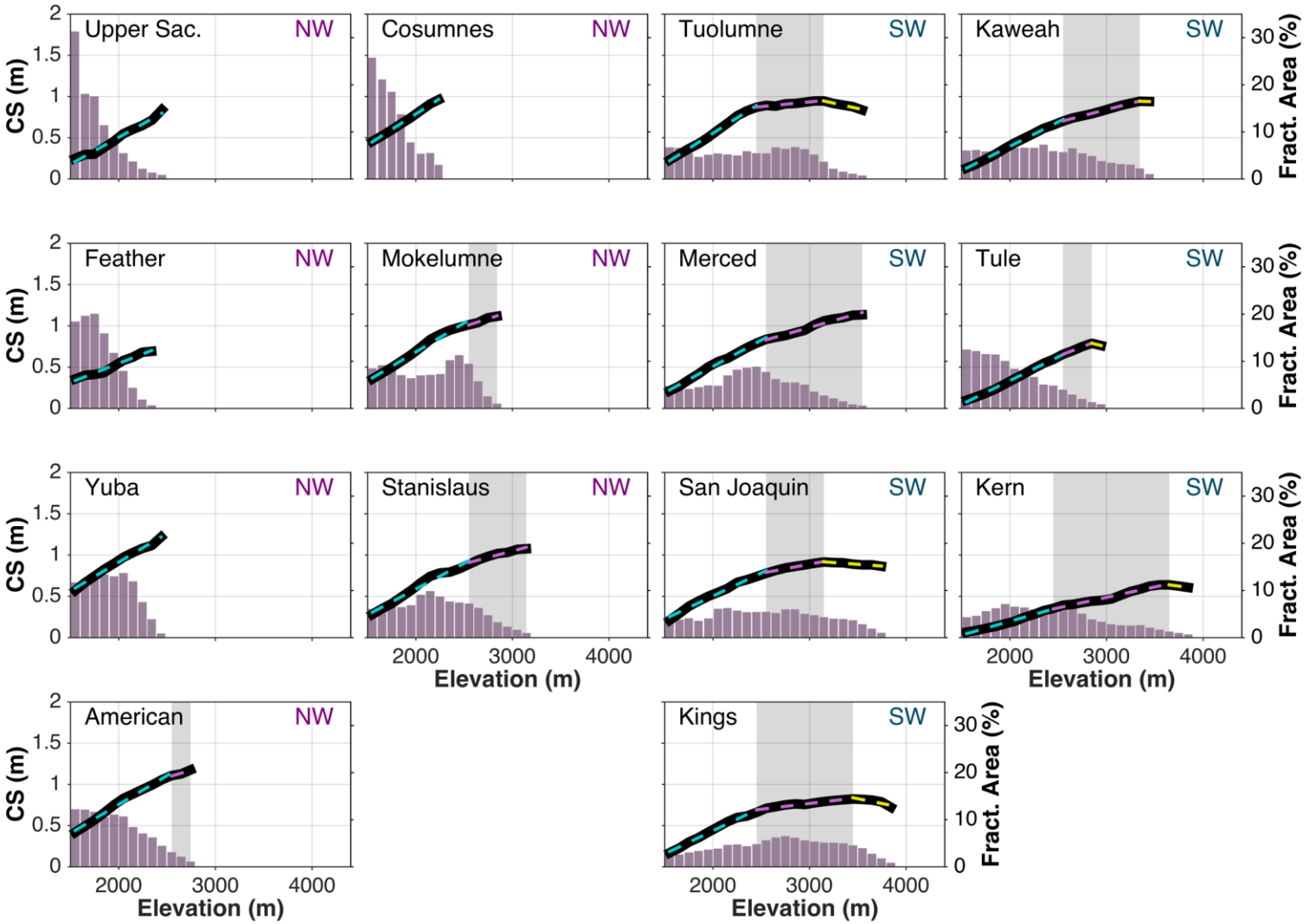

Figure 3.3. Elevational distribution of CS where the solid line indicates the 31-year average and the dashed lines correspond to the lines of best fit for each elevation zone. The histogram displays the (static) elevational distribution of pixels as a fraction of the total area above 1500 m. Each bar represents >0.5% of the total area. EZ_2 is shaded in gray.

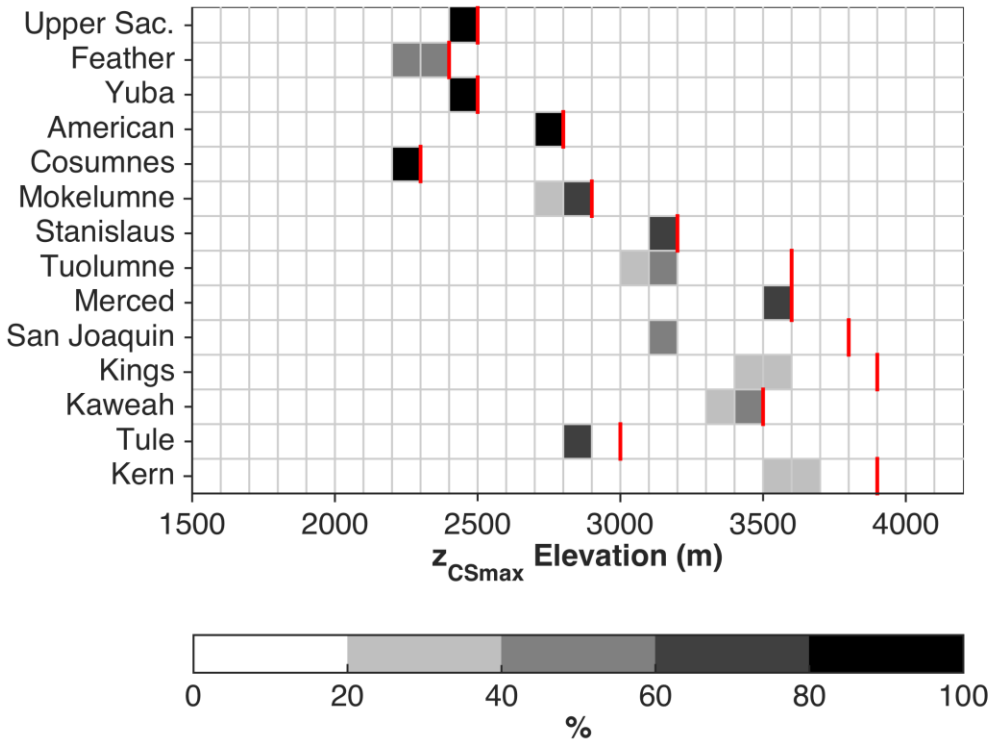

Figure 3.4. Percentage of the 31 years that $z_{CS\max}$ was located within 100-m elevation bins for each basin. Red lines demarcate the upper bound of the bin containing the maximum elevation, $z_{\max}$, for each basin.

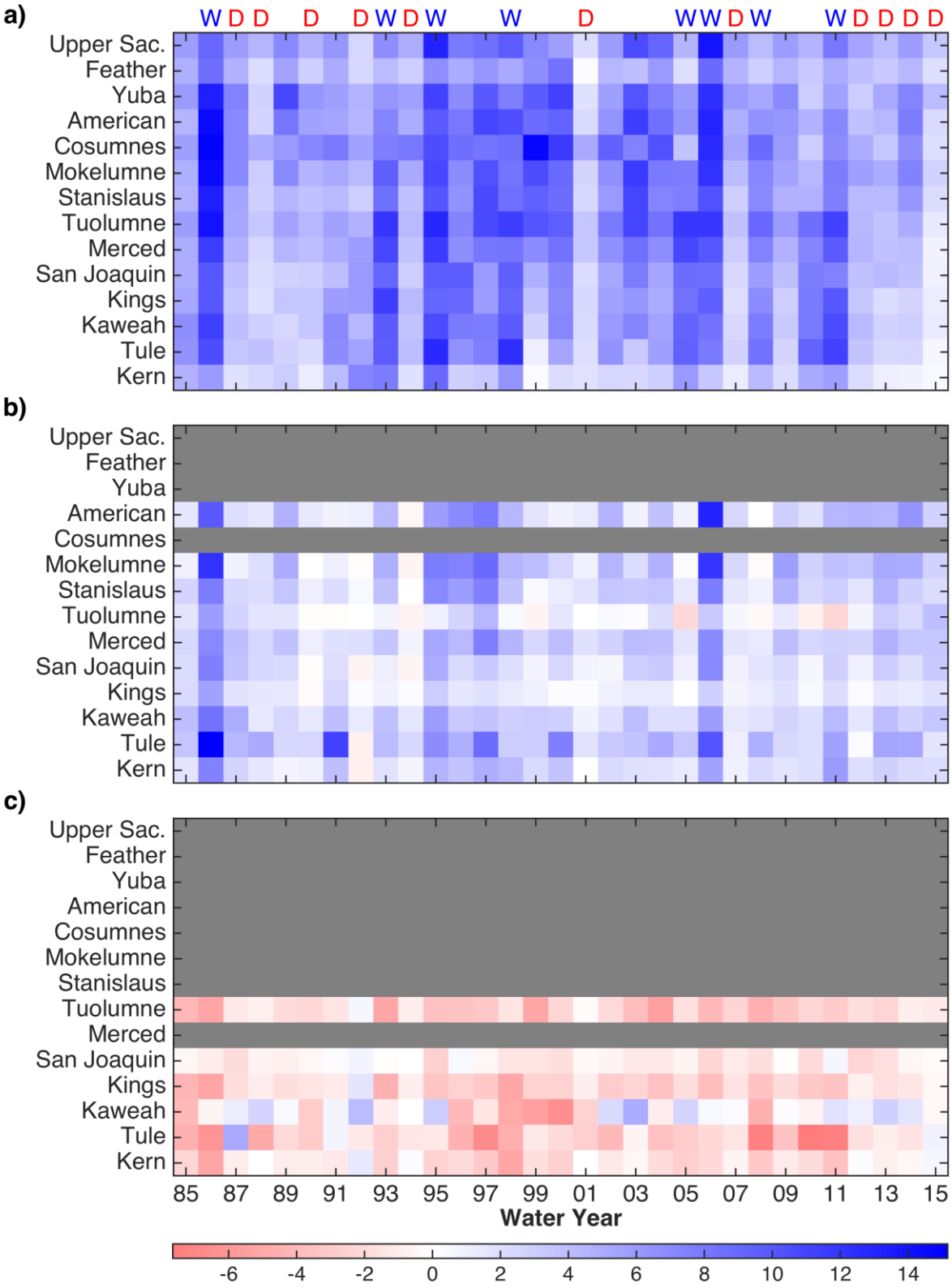

Figure 3.5. Basin-wide CS gradients (in cm/100 m) for a) EZ_1, b) EZ_2, and c) EZ_3 over the 31 years. Wet and dry years are denoted with 'W' and 'D', respectively.

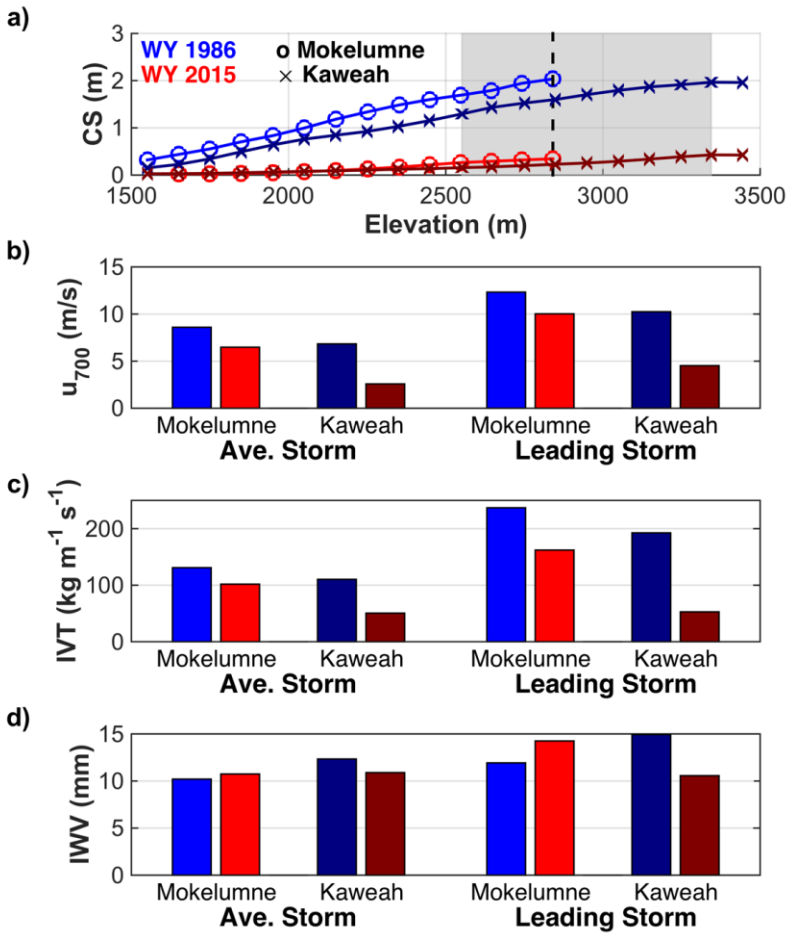

Figure 3.6. Seasonal and snowstorm characteristics for Mokelumne and Kaweah during WYs 1986 (blue) and 2015 (red). a) Seasonal orographic CS curves, where 'o' and '×' symbols represent Mokelumne and Kaweah, respectively. EZ_2 is shaded gray. It spans the entire shaded region for Kaweah, but the dashed line demarcates the upper bound of EZ_2 for Mokelumne. Average synoptic snowstorm and leading storm b) u_{700}, c) IVT, and d) IWV. Lighter shades of blue/red correspond to Mokelumne, while darker shades correspond to Kaweah in all panels.

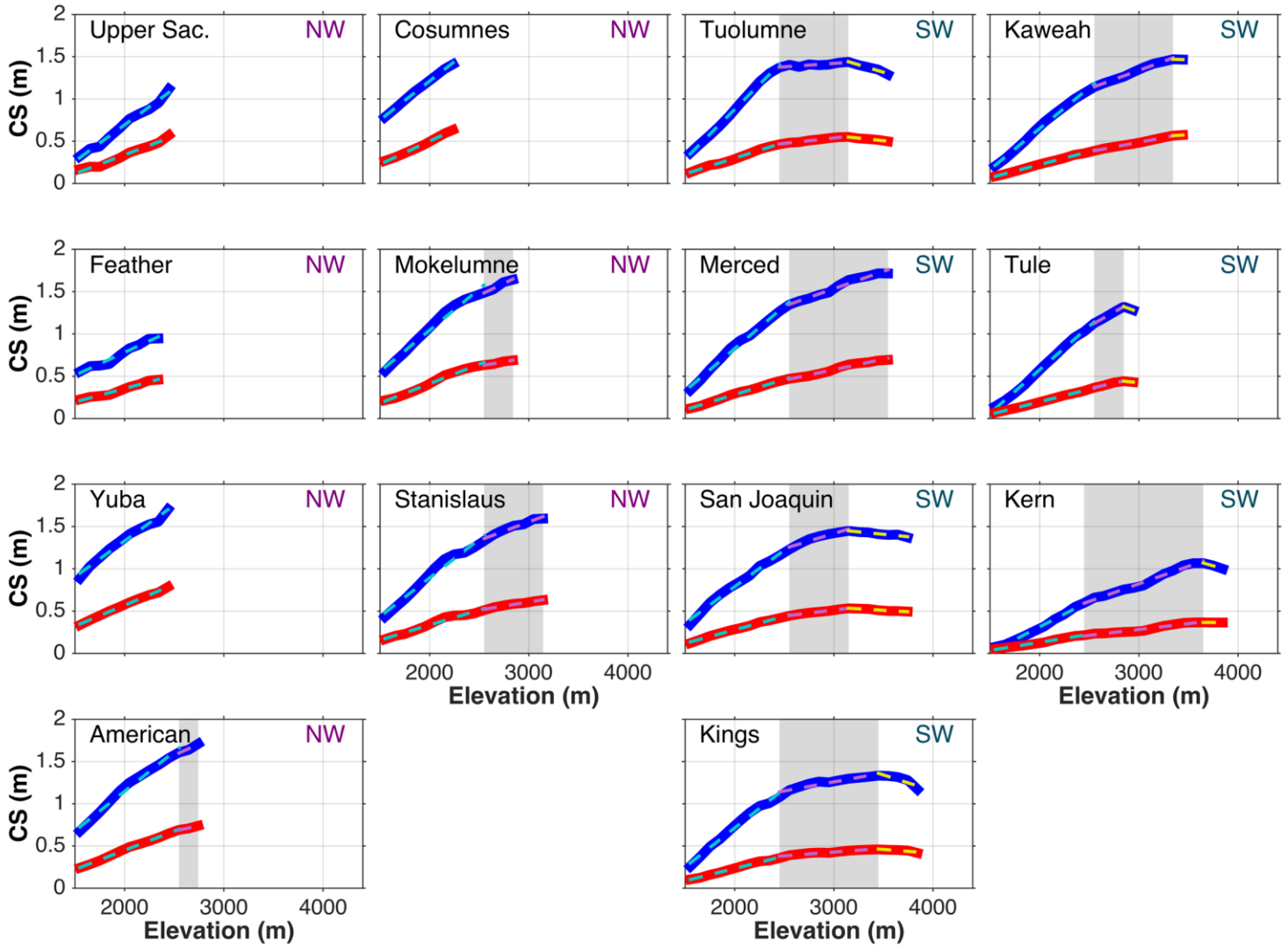

Figure 3.7. Elevational distribution of CS where solid lines indicate the wet-year (blue) and dry-year (red) averages. Dashed lines correspond to the lines of best fit for each elevation zone. EZ_2 is shaded in gray.

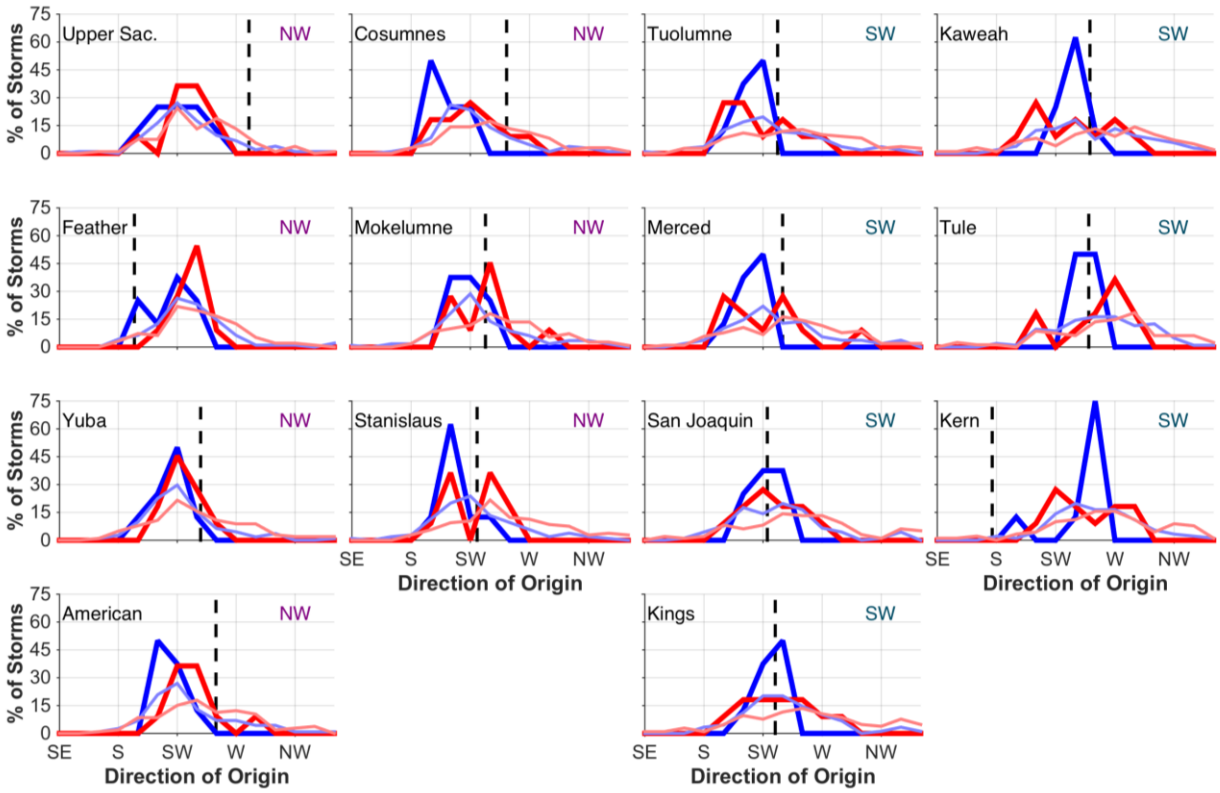

Figure 3.8. IVT direction of origin as a percent of the total number of snowstorms over all wet (blue) and dry (red) years for each basin using 15°-bins. Lighter and darker lines represent all snowstorms and leading snowstorms, respectively. Dashed lines demarcate the basin-average terrain aspect values. Negligible fractions of storms originated outside of those directions shown.

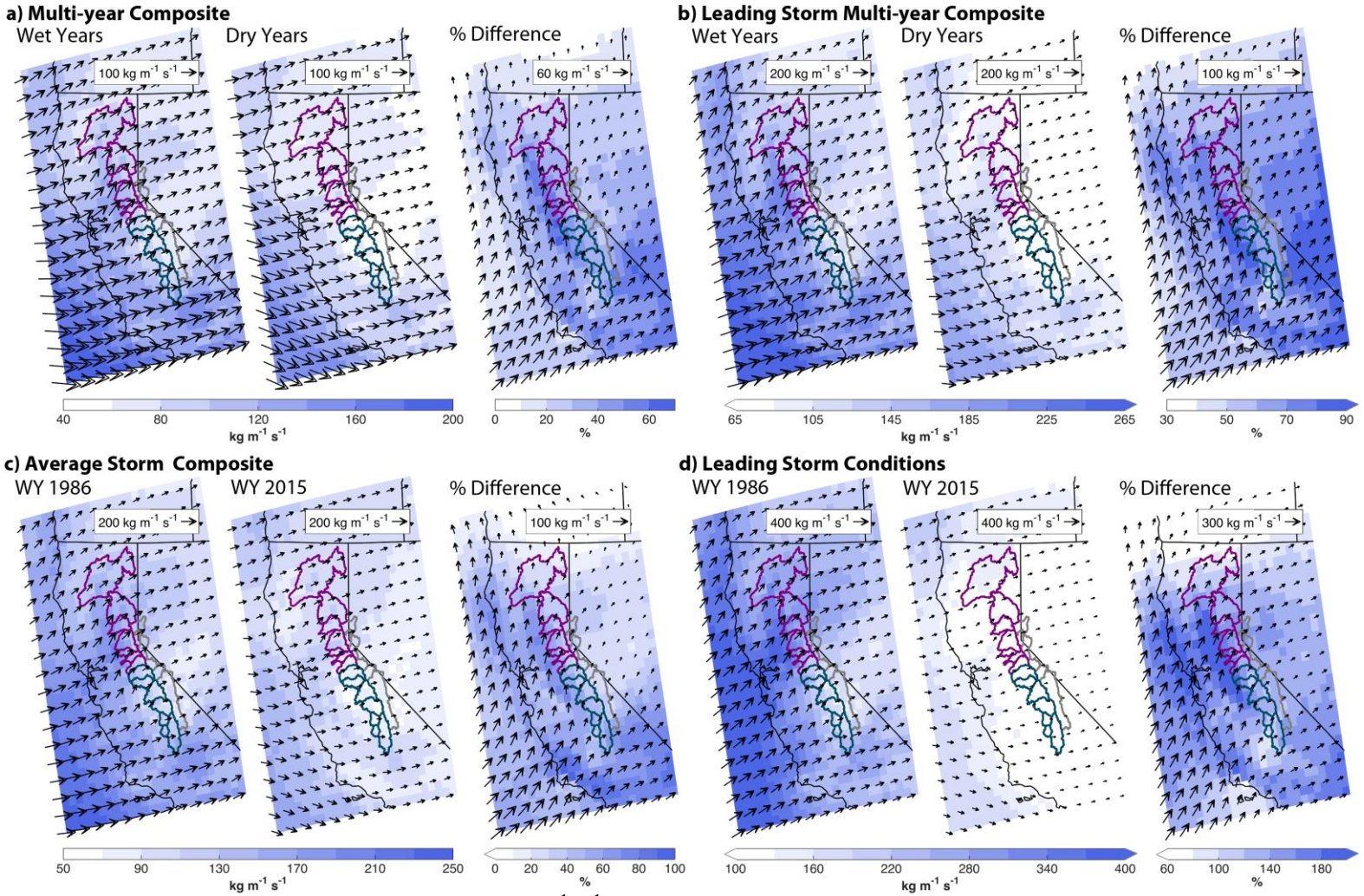

Figure 3.9. a)-d) (first two maps) Average IVT (in kg m^{-1} s^{-1}) across all storms in a) wet and dry years and c) WY 1986 and 2015 and leading storms in b) wet and dry years and d) WY 1986 and 2015, respectively. (third map) Arrows denote IVT vector difference (first minus second vector fields) and shading indicates percent difference given by $\%\,\text{difference} = \left(\left|IVT_1\right| - \left|IVT_2\right|\right) / \left|IVT_2\right| \cdot 100\%$, where $\left|IVT_1\right|$ and $\left|IVT_2\right|$ are the magnitudes of the first and second IVT maps in each set, respectively.

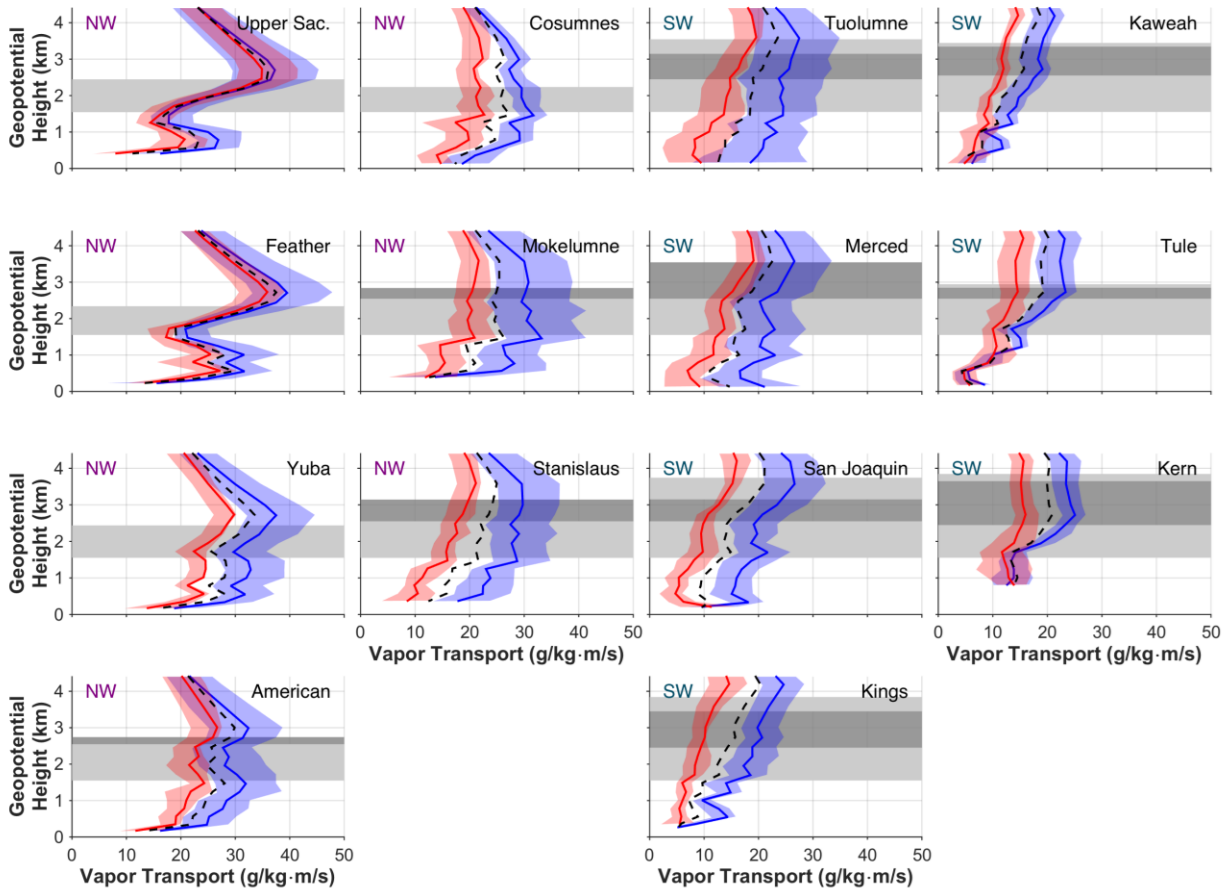

Figure 3.10. Wet-year (blue line), dry-year (red line), and 31-year average (dashed line) horizontal vapor transport profiles. Interquartile ranges for wet and dry years are shaded in their respective colors. Elevation zones are shaded in light gray (EZ_1 and EZ_3) and dark gray (EZ_2), where appropriate.

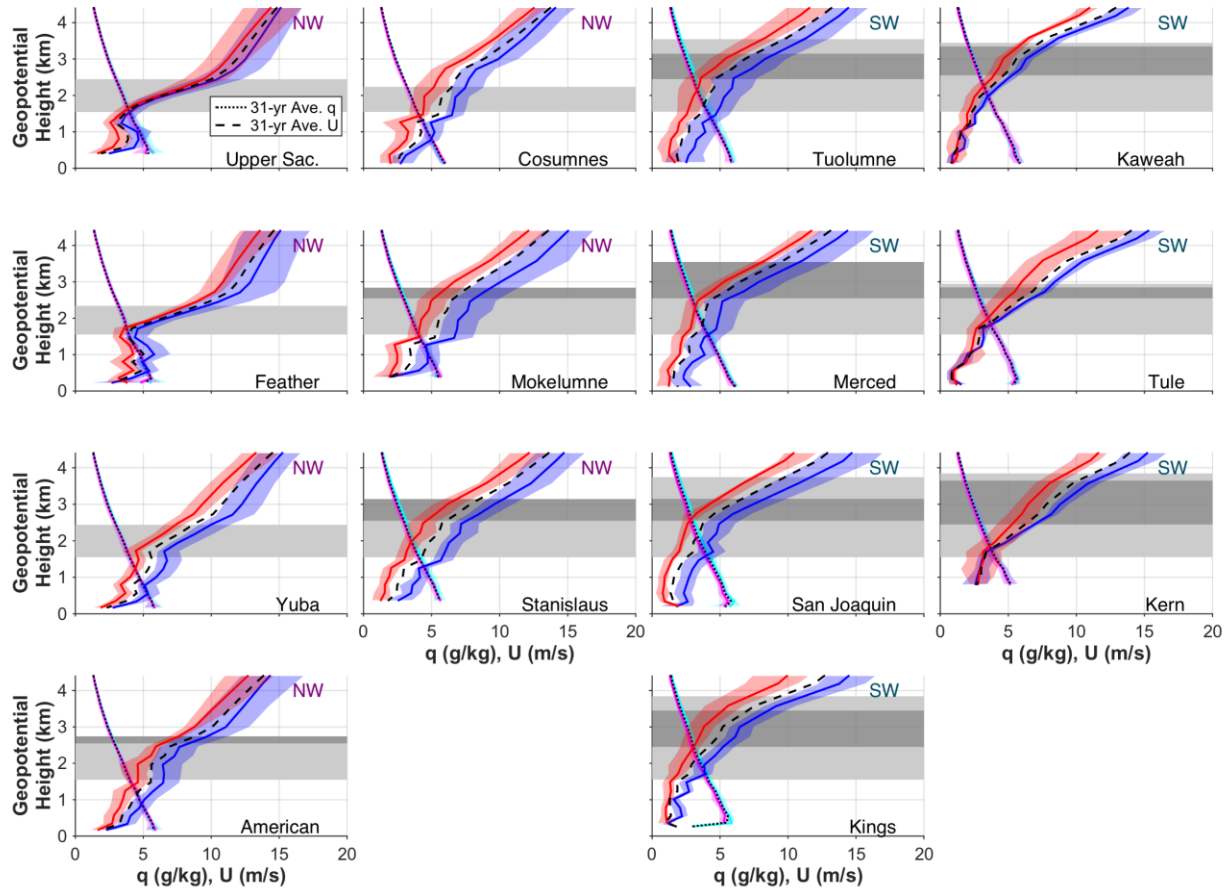

Figure 3.11. Same as Figure 10, except the wet-year/dry-year profiles are shown in cyan/magenta for specific humidity (q) and blue/red for wind speed (U), respectively.

3.8 Bibliography

Aguado, E. (1990), Elevational and latitudinal patterns of snow accumulation departures from normal in the Sierra Nevada, *Theor. Appl. Climatol.*, 42, 177-185.

Alpert, P. (1986), Mesoscale indexing of the distribution of orographic precipitation over high mountains, *J. Clim. Appl. Meteor.*, 532-545.

Bales, R., J. J. Battles, Y. Chen, M. H. Conklin, E. Holst, K. L. O'Hara, P. Saksa, and W. Stewart (2011), Forests and water in the Sierra Nevada: Sierra Nevada watershed ecosystem enhancement project, Sierra Nevada Research Institute, Report Number 11.1.

Barnett, T. P., J. C. Adam, and D. P. Lettenmaier (2005), Potential impacts of a warming climate on water availability in snow-dominated regions, *Nature*, 438(5866), doi:10.1038/nature04141.

Barros, A. P., and D. P. Lettenmaier (1994), Dynamic modeling of orographically induced precipitation, *Rev. Geophys.*, 32, 265-284.

Cayan, D. R., E. P. Mauere, M. D. Dettinger, M. Tyree, and K. Hayhoe (2008), Climate change scenarios for the California region, *Climatic Change*, 87, S21-S42.

Colle, B. A. (2004), Sensitivity of orographic precipitation to changing ambient conditions and terrain geometries: An idealized modeling perspective, *J. Atmos. Sci.*, 61, 588-606.

Dettinger, M. D., K. Redmond, and D. Cayan (2004), Winter orographic precipitation ratios in the Sierra Nevada – Large-scale atmospheric circulations and hydrologic consequences, *J. Hydrometeor.*, 5, 1102-1116.

Downing, J. (2015), Forest thinning may increase water yield from the Sierra Nevada, *Calif. Agr.*, 69(1), 10-11.

Galewsky, J., and A. Sobel (2005), Moist dynamics and orographic precipitation in northern and central California during the New Year's Flood 1997, *Mon. Wea. Rev.*, 133, 1594-1612.

Grubišić, V., R. K. Vellore, and A. W. Huggins (2005), Quantitative precipitation forecasting of wintertime storms in the Sierra Nevada: Sensitivity to the microphysical parameterizations and horizontal resolution, *Mon. Wea. Rev.*, 133, 2834-2859.

Grünewald, T., Y. Buhler, and M. Lehning (2014), Elevation dependency of mountain snow depth, *Cryosphere*, 8, 2381-2394, doi:10.5194/tc-8-2381-2014.

Guan, B., N. P. Molotch, D. E. Waliser, E. J. Fetzer, and P. J. Neiman (2010), Extreme snowfall events linked to atmospheric rivers and surface air temperature via satellite measurements, *Geophys. Res. Lett.*, 37, L20401, doi:10.1029/2010GL044696.

Houze Jr., R. A. (2012), Orographic effects on precipitating clouds, *Rev. Geophys.*, 50, RG1001, doi:10.1029/2011RG00365.

Hughes, M., A. Hall, and R. G. Fovell (2009), Blocking in areas of complex topography, and its influence on rainfall distribution, *J. Atmos. Sci.*, 66, 508-518, doi:10.1175/2008JAS2689.1.

Hughes, M., P. J. Neiman, E. Sukovich, and M. Ralph (2012), Representation of the Sierra Barrier Jet in 11 years of a high-resolution dynamical reanalysis downscaling compared with long-term wind profiler observations, *J. Geophys. Res.*, 117, D18116, doi:10.1029/2012JD017869.

Huning, L. S., and S. A. Margulis (2017), Climatology of seasonal snowfall accumulation across the Sierra Nevada (USA): Accumulation rates, distributions, and variability, *Water Resour. Res.*, in review.

Kapnick, S., and A. Hall (2010), Observed climate-snowpack relationships in California and their implications for the future, *J. Climate*, 23, 3446-3456, doi:10.1175/2010JCLI2903.1.

Kirchner, P. B., R. C. Bales, N. P. Molotch, J. Flanagan, and Q. Guo (2014), LiDAR measurement of seasonal snow accumulation along an elevation gradient in the southern Sierra Nevada, California, *Hydrol. Earth Syst. Sc.*, 18, 4261-4275, doi:10.5194/hess-18-4261-2014.

Lavers, D. A., F. M. Ralph, D. E. Waliser, A. Gershunov, and M. D. Dettinger (2015), Climate change intensification of horizontal water vapor transport in CMIP5. *Geophys. Res. Lett.*, 42, doi:10.1002/2015GL064672.

Lavers, D. A., G. Villarini, R. A. Allan, E. F. Wood, and A. J. Wade (2012), The detection of atmospheric rivers in atmospheric reanalyses and their links to British winter floods and the large-scale climatic circulation. *J. Geophys. Res.*, 117, D20106, doi:10.1002/2015GL064672.

Lehning, M. (2013), Snow-atmosphere interactions and hydrological consequences, *Adv. Water Resour.*, 55, 1-3, doi:10.1016/j.advwatres.2013.02.001.

Leung, L. R., and S. J. Ghan (1998), Parameterizing subgrid orographic precipitation and surface cover in climate models, *Mon. Wea. Rev.*, 126, 3271-3291.

Luce, C. H., J. T. Abatzoglou, and Z. A. Holden (2013), The missing mountain water: Slower westerlies decrease orographic enhancement in the Pacific Northwest USA, *Science*, 342, 1360-1364, doi:10.1126/science.1242335.

Lundquist, J., M. Hughes, B. Henn, E. Gutmann, B. Livenh, J. Dozier, and P. Neiman (2015), High-elevation precipitation patterns: Using snow measurements to assess daily gridded datasets across the Sierra Nevada, California, *J. Hydrometeor.*, 16, 1773-1792 doi:10.1175/JHM-D-15-0019.1.

Lundquist, J. D., J. R. Minder, P. J. Neiman, E. Sukovich (2010), Relationships between barrier jet heights, orographic precipitation gradients, and streamflow in the Northern Sierra Nevada, *J. Hydrometeor.*, 11, 1141-1156, doi:10.1175/2010JHM1264.1.

Lundquist, J. D., P. J. Neiman, B. Martner, A. B. White, D. J. Gottas, and F. M. Ralph (2008), Rain versus snow in the Sierra Nevada, California: Comparing Doppler profiling radar observations of melting level, *J. Hydrometeor.*, 9, 194-211, doi:10.1175/2007/JHM853.1.

Margulis, S., G. Cortés, M. Girotto, and M. Durand (2016), A Landsat-era Sierra Nevada (USA) snow reanalysis (1985-2015), *J. Hydrometeor.*, 17, 1203-1221, doi:10.1175/JHM-D-15-0177.1.

Mesinger, F., and Coauthors (2006), North American Regional Reanalysis, *Bull. Amer. Meteor. Soc.*, 87, 343-360, doi:10.1175/BAMS-87-3-343.

Mote, P. W., A. F. Hamlet, M. P. Clark, and D. Lettenmaier (2005), Declining mountain snowpack in Western North American, *Bull. Amer. Meteor. Soc.*, 86(1), 39-49.

Neiman, P. J., M. Hughes, B. J. Moore, F. M. Ralph, and E. S. Sukovich (2013), Sierra barrier jets, atmospheric rivers, and precipitation characteristics in Northern California: A composite perspective based on a network of wind profilers. *Mon. Wea. Rev.*, 141, 4211-4233, doi:10.1175/MWR-D-13-00112.1.

Neiman, P. J., E. M. Sukovich, F. M. Ralph, and M. Hughes (2010), A seven-year wind profiler-based climatology of the windward barrier jet along California's Northern Sierra Nevada, *Mon. Wea. Rev.*, 138, 1206-1233, doi:10.1175/2009MWR3170.1.

O'Hara, B. F., M. L. Kaplan, and S. J. Underwood (2009), Synoptic climatology analyses of extreme snowfalls in the Sierra Nevada, *Wea. Forecasting*, 24, 1610-1624, doi:10.1175/2009WAF2222249.1.

Pandey, G. R., D. R. Cayan, and K. P. Georgakakos (1999), Precipitation structure in the Sierra Nevada of California during winter, *J. Geophys. Res.: Atmos.*, 104(D10), 12019-12030, doi:10.1029/1999JD900103.

Pavelsky, T. P., S. Sobolowski, S. B. Kapnick, and J. B. Barnes (2012), Changes in orographic precipitation patterns caused by a shift from snow to rain, *Geophys. Res. Lett.*, 39, L18706, doi:10.1029/2012GL052741.

Ralph, F. M., P. J. Neiman, G. A. Wick, S. I. Gutman, M. D. Dettinger, D. R. Cayan, and A. B. White (2006), Flooding on California's Russian River: Role of atmospheric rivers, *Geophys. Res. Lett.*, 33, L13801, doi:10.1029/2006GL026689.

Rasmussen, R., and Coauthors (2012), How well are we measuring snow? The NOAA/FAA/NCAR winter precipitation test bed, *Bull. Amer. Meteor. Soc.*, 811-829, doi:10.1175/BAMS-D-11-00052.1.

Roe, G. H. (2005), Orographic precipitation, *Annu. Rev. Earth Pl. Sc.*, 33, 645-671, doi:10.1146/annurev.earth.33.092203.122541.

Rosenthal, W., and J. Dozier (1996), Automated mapping of montane snow cover at subpixel resolution from the Landsat Thematic Mapper, *Water Resour. Res.*, 32, 115-130, doi:10.1029/95WR02718.

Rutz, J. J., W. J. Steenburgh, and F. M. Ralph (2014), Climatological characteristics of atmospheric rivers and their inland penetration over the Western United States, *Mon. Wea. Rev.*, 142, 905-921, doi:10.1175/MWR-D-13-00168.1.

Serreze, M. C., M. P. Clark, and A. Frei (2001), Characteristics of large snowfall events in the montane western United States as examined using snowpack telemetry (SNOTEL) data, *Water Resour. Res.*, 37(3), 675-688.

Xia, Y., and Coauthors (2012), Continental-scale water and energy flux analysis and validation for the North American Land Data Assimilation System project phase 2 (NLDAS-2): 1. Intercomparison and application of model products, *J. Geophys. Res.*, 117, D3, 1984-2012, doi:10.1029/2011JD016048.

Chapter 4: Implications of Atmospheric River Detection Methods on Characterizing Their Contribution to Seasonal Snowfall across the Sierra Nevada (USA)

4.1 Introduction

Long, narrow moisture-laden low-level jets, known as atmospheric rivers (ARs), play significant roles in the hydrology and water resources of the western United States. An estimated 20-50% of the precipitation across California is derived from ARs, on average [*Dettinger et al.,* 2011]. In northern California, *Ralph et al.* [2016] found that 92% of the days with extreme daily precipitation occurred on the day of or the day after an AR. When ARs interact with topography, their abundant moisture and strong vapor transport promote orographic precipitation. On average in the Sierra Nevada, ~30-40% of the seasonal snowfall has been attributed to ARs [*Guan et al.,* 2010]. With the intense precipitation that ARs deliver across regions such as California, they can beneficially fill reservoirs and increase the snowpack [e.g. *Guan et al.,* 2010, 2013a; *Rutz and Steenburgh,* 2012; *Rutz et al.,* 2014] and/or lead to destructive and costly flooding [e.g. *Ralph et al.,* 2006; *Dettinger et al.,* 2011].

Since ARs are often among the largest storms of a winter season in the Sierra Nevada, and the range accumulates a significant fraction of its snowfall during a few large snowstorms each year [*Serreze et al.,* 2001; *O'Hara et al.,* 2009; *Guan et al.,* 2010; *Huning and Margulis,* 2017a], it is important to accurately diagnose ARs over this hydrologically-relevant region (Figure B.1). ARs have been traditionally diagnosed using satellite-derived integrated water vapor (IWV) [e.g. *Ralph et al.,* 2004; *Neiman et al.,* 2008; *Ralph et al.,* 2016; etc.] and more recently using reanalysis-based integrated vapor transport (IVT) approaches [e.g. *Lavers et al.,*

2012; *Rutz et al.*, 2014; *Guan and Waliser*, 2015; etc.]. It is important to understand the potential implications of utilizing different AR detection algorithms to estimate AR-derived snowfall across mountainous terrain at climatological and annual scales.

Although *Huning and Margulis* [2017b] did not specifically focus on AR events, they found that stronger correlations existed between orographic cumulative snowfall (CS) gradients and IVT than between the orographic gradients and IWV across the Sierra Nevada. *Rutz et al.* [2014] similarly concluded that IVT was more strongly correlated to precipitation over the mountainous western U.S. *Guan and Waliser* [2015] also determined that IVT is a better indicator of enhanced precipitation along the western U.S. coastline. Such findings motivate this study and the driving question for this work: How does the selection of AR detection algorithms/methodologies, datasets, and physical quantities impact the understanding of the relative importance of ARs across the Sierra Nevada? Since the hydrologic implications of different AR diagnoses have not been previously explored, this study aims to fill this knowledge gap. To answer this question, two AR catalogs were selected to specifically investigate: 1) How much snowfall is delivered to the Sierra Nevada during AR events (e.g. full snowfall volume, snowfall distribution, snowfall at high elevations, etc.)? 2) Are there differences in orographic enhancement between AR and non-AR driven elevational snowfall distributions?

4.2 Data and Methods

Independent datasets were used to diagnose AR events and snowfall across 20 basins in the Sierra Nevada (Figure B.1). While all basins were used to quantify the range-wide CS volumes, only basins in the northwest (NW) and southwest (SW) were used to investigate orographic CS distributions along the windward (i.e. western) side of the range.

4.2.1 Atmospheric River Catalogs

AR occurrences were diagnosed using two AR catalogs derived from: 1) a satellite-based approach described in *Neiman et al.* [2008] and 2) an atmospheric reanalysis-based approach introduced in *Guan and Waliser* [2015]. They are among several AR catalogs that have been previously developed. It is worth emphasizing that all CS information was derived from the snowfall dataset described below and the AR catalogs were used solely to identify days on which ARs occurred (hereafter, AR days).

4.2.1.1 Satellite-based IWV AR Catalog

Using the Special Sensor Microwave Imager (SSM/I) and Special Sensor Microwave Imager Sounder (SSMIS), *Neiman et al.* [2008] identified landfalling ARs in western North America when at least 2 cm of IWV was observed over a contiguous region >~2000 km long and <1000 km wide. They cataloged AR landfall dates along the California coastline (32.5°N-41.0°N) during water years (WYs; 1 October-30 September) 1998-2005 when the above criteria were satisfied for two consecutive passes of the satellite (spanning at least 12 hours) on a calendar day. The record used herein was expanded through 2015 to include 18 years. Hereafter, this AR catalog is referred to as IWV_{N08}.

4.2.1.2 Atmospheric Reanalysis-based IVT AR Catalog

The second AR catalog utilized herein was derived using IVT from the 6-hourly, 1.5-degree atmospheric fields of the ECMWF Interim atmospheric reanalysis (ERA-Interim; *Dee et al.,* 2011). Among other observational information, clear-sky radiance from SSM/I was assimilated in ERA-Interim [*Dee et al.,* 2011]. The AR algorithm, described in detail in *Guan and Waliser* [2015], used an IVT intensity threshold (monthly, location-dependent 85th-percentile), IVT direction criteria (overall coherence in direction), and geometrical constraints

(length >2000 km and length-to-width ratio >2) to identify ARs every six hours globally. Hereafter, this catalog is referred to as IVT_{GW15}. For comparison with IWV_{N08}, an AR day from IVT_{GW15} was defined when at least three consecutive time steps (i.e. 18 hours) on a calendar day indicated that an AR structure occurred [*Guan and Waliser*, 2015] within the dashed region in Figure B.1. Note that the IVT threshold used in IVT_{GW15} accounts for seasonal and latitudinal variations in the atmospheric fields, whereas the 2 cm IWV threshold used in IWV_{N08} is invariant in space and time. Also, the horizontal resolution of IVT_{GW15} is roughly four times coarser than IWV_{N08}.

4.2.2 Snowfall Dataset

Previous studies that examined AR impacts on snowfall in the Sierra Nevada generally used point-scale in situ measurements [e.g. *Rutz and Steenburgh,* 2012; *Rutz et al.,* 2014; *Guan et al.,* 2012, 2016] while fewer studies utilized distributed snowfall products [*Guan et al.,* 2010, 2013a]. This is an important distinction because point-scale estimates are unable to capture the large heterogeneity of snowfall across the Sierra Nevada since they sample <1% of the snow-covered area and tend to be located at low/mid-elevations in flat clearings [*Guan et al.,* 2013b; *Margulis et al.,* 2016]. Point-scale observations alone cannot directly estimate the seasonal range-wide CS or AR-derived CS volumes as done herein, and previous studies using gridded snow information have not quantified the AR impact on the CS volume. This paper extends the work of previous studies such as *Guan et al.* [2010, 2013a] who suggested that a better understanding of the response of snow water equivalent (SWE) to ARs would benefit from more detailed and distributed snow information, which this study aims to provide.

The 90-m, daily Sierra Nevada snow reanalysis [*Margulis et al.,* 2016] provided the snowfall accumulation information (above 1500 m) used herein. As detailed in *Margulis et al.*

[2015], spatially-distributed SWE fields were derived within a Bayesian framework where Landsat fractional snow-covered area images were assimilated over the mountain range. *Huning and Margulis* [2017a] verified CS derived from this reanalysis with over 2600 station years of in situ observations. Relative to observations, they found root-mean-square and mean errors of seasonal CS to be 12 cm and -4 cm, respectively, demonstrating that the reanalysis could be utilized as an accurate snowfall dataset.

The CS was computed using daily increases in SWE [*Huning and Margulis*, 2017a,b] as given by:

$$CS = \sum_{t=1\,\mathrm{Nov}}^{1\,\mathrm{Apr}} S(t), \text{ for } S = \Delta SWE > 0 \tag{4.1}$$

where snowfall (S, quantified in units of equivalent water depth) is accumulated over the winter season, defined as 1 November-1 April herein. The high-resolution, distributed CS information allows for the examination of AR-derived CS (hereafter, AR CS) volumes, high-elevation AR CS, and the rate of change of AR CS with elevation compared to non-AR driven CS.

Following *Neiman et al.* [2008] and *Guan et al.* [2010, 2012, 2013a], AR CS was computed by considering the snowfall that occurred the day of an AR as well as one day before and one day after the AR event. An AR "event" was defined as a single, isolated AR day or a set of consecutive AR days. The ±1 day window accounts for potential lead- and lag-time response since analysis was performed on the daily time scale. Days included within this temporal window were defined as CS-contributing days and differ from the (diagnosed) AR days defined above. Snowfall that is not associated with an AR (hereafter, non-AR CS) is equal to the difference between the total (seasonal) CS and the AR CS. The fraction of the total CS that was derived from ARs is denoted as f_{AR}. The rates of change of AR and non-AR CS with elevation (z) are denoted as dCS_{AR}/dz and $dCS_{non\text{-}AR}/dz$, respectively.

4.2.3 AR Detection Statistics

The difference in the number of AR days between the two catalogs is examined below. AR days were used to compare the performance of AR detection from the two catalogs by counting the number of AR hits, false alarms, misses, and correct negatives (defined in Section B.2). To understand the relative performance of IWV_{N08} and IVT_{GW15} and expand upon *Guan and Waliser* [2015], the threat score, false alarm ratio (FAR), probability of detection (POD), and probability of false detection (POFD) were also computed following *Wilks* [2006] as defined in Section B.2. Two sets of statistics were produced by toggling the relative roles of the two catalogs between "reference" and "estimate" as presented below.

4.3 Results and Discussion

The total CS climatology over the Sierra Nevada (Figure B.2) results from the combination of AR-driven snowfall and other snowstorm-driven snowfall. Over the 18-year period, the range received an average 21.0 km^3 of CS or ~44 cm of CS annually. The distinct rain shadow effect is observable when comparing the CS on the windward (western) and leeward (eastern) sides of the Sierra Nevada. The climatology exhibits a distinct orographic CS signature where more CS occurs at high elevations [*Huning and Margulis,* 2017a,b]. The analysis below explores how the total CS (Figure B.2) is partitioned between AR and non-AR amounts depending on AR detection approaches.

4.3.1 AR Cumulative Snowfall Distribution

4.3.1.1 Satellite-based IWV AR Catalog (IWV_{N08})

The spatial patterns observed in the 18-year climatology of the IWV_{N08}-derived AR CS (Figure 4.1a, left) resemble those of the total CS climatology (Figure B.2). To examine orographically-driven CS, Figure 4.1a (middle and right) presents both the climatology and inter-

annual variability of the CS in the NW and SW regions as it is partitioned into the AR (blue) and non-AR (red) components. The middle panel demonstrates that for each elevation, the average AR and non-AR CS accumulation is larger in the NW than in the SW, likely due to a more persistent storm track farther north. The inter-annual variability increases with elevation in both regions. Across all elevations, the AR contribution to the total CS is greater in the NW than in the SW both in terms of the AR CS depth and f_{AR} (black). ARs contribute ~40% of the CS at the highest elevations (2700-2800 m) in the NW. In the SW, f_{AR} increases with elevation up to ~3000 m before f_{AR} becomes relatively constant at ~37% and the rate of change of CS with elevation becomes negative (i.e. $dCS/dz < 0$, due to atmospheric moisture depletion).

The rate of change of AR CS with elevation (blue) is greater in the NW than the SW (Figure 4.1a, right). While ARs are known to promote orographic enhancement, less is known about the degree to which ARs yield greater orographic enhancement relative to non-AR driven (red) mechanisms. Based on IWV_{N08}, AR CS is more orographically enhanced than non-AR CS above ~2100-2300 m, which is termed the "transition elevation" herein, in both the NW and SW (Figure 4.1a, right). In other words, AR CS changes faster with elevation than non-AR CS above the transition elevation. Neglecting negative rates of change, above the transition elevation AR CS consistently changes faster with elevation than non-AR CS and dCS_{AR}/dz can be as much as 2.1 to 2.3 times larger than $dCS_{non\text{-}AR}/dz$ in the NW and SW, respectively.

4.3.1.2 Reanalysis-based IVT AR Catalog (IVT_{GW15})

The effects of utilizing IVT_{GW15} to understand the spatial and elevational distribution of AR CS are similarly examined in Figure 4.1b. The 18-year average AR CS shows strong elevational dependence across the Sierra Nevada. On average in the SW, ARs contribute over half of the seasonal CS above ~2200 m, which increases to ~59% of the CS above ~2800 m

(Figure 4.1b, middle). All elevations in the NW receive over 47% of the seasonal CS from ARs and more than 60% above ~2400 m. Similar to Figure 4.1a (middle), Figure 4.1b (middle) indicates that at each elevation ARs contribute more CS in the NW than in the SW. The average f_{AR} increases by over 14% in the NW and 20% in the SW from the lowest to highest elevations using either AR catalog. The inter-annual variability of AR and non-AR CS tends to show greater elevational dependence than f_{AR}, which remains comparatively constant. Greater inter-annual variability is observed in the AR CS than non-AR CS at the highest elevations, indicating that the non-AR elevational distribution has a lower variance (Figure 4.1b, middle). This relationship is reversed in Figure 4.1a (middle).

Using IVT_{GW15}, Figure 4.1b (right) shows that AR CS exhibits greater orographic enhancement than non-AR CS. This was similarly demonstrated in Figure 4.1a (right); however, dCS_{AR} / dz is unconditionally larger than $dCS_{non\text{-}AR} / dz$ in Figure 4.1b (right). Again, only positive values were considered. Therefore, the transition elevation observed in Figure 4.1a (right) at ~2100-2300 m with IWV_{N08} is not present with IVT_{GW15}. The transition elevation results from differences in the methodologies between the two AR diagnoses with IWV vs. IVT likely playing an important role. Using IWV-based diagnostics, ARs have been found to be warmer storms than other wintertime storms, which would correspond to ARs having a higher snow line and accumulating less AR CS at lower elevations compared to colder non-AR events [*Neiman et al.,* 2008; *Guan et al.*, 2010, 2016; *Kim et al.,* 2013]. However it is hypothesized that since IVT_{GW15} identified more ARs (shown below), this AR catalog captured cooler ARs than IWV_{N08} resulting in a lower diagnosed snow line. Moreover, wind and moisture as opposed to only moisture (in the case of IWV_{N08}) play a role in the IVT_{GW15}-diagnosed ARs. Increasing air temperature allows more moisture to be held in air parcels and therefore is the key driver in the

IWV_{N08} algorithm, whereas having high wind speed/transport can result in an AR detected in IVT_{GW15} even with cooler air temperatures and lower IWV. Nonetheless, the general shapes of the curves in Figures 4.1a and 4.1b are similar between the IWV_{N08}- and IVT_{GW15}-partitioned CS.

Figure 4.1b (right) demonstrates that the AR CS changes up to 3.0 and 3.8 times faster with elevation than the non-AR CS in the NW and SW, respectively, at ~2500-2600 m. The largest 18-year average rates of change of AR CS are 6.6 cm SWE/100 m elevation in the NW at ~1900-2000 m and 3.9 cm/100 m in the SW at ~2000-2100 m. The corresponding ratios of dCS_{AR} / dz to $dCS_{non\text{-}AR} / dz$ at these elevations are 1.8 and 1.9, respectively. Below 3000 m, the AR CS derived from IVT_{GW15} consistently shows greater orographic enhancement than with IWV_{N08} and dCS_{AR} / dz relative to $dCS_{non\text{-}AR} / dz$ is larger when utilizing IVT_{GW15}. Using either AR catalog it can be concluded that, on average, ARs yield greater orographically-enhanced CS than non-AR mechanisms at the highest elevations across the western Sierra Nevada. Unconditional enhancement of AR CS is exhibited when diagnosed from IVT_{GW15}, whereas AR CS is only conditionally enhanced (i.e. above ~2100-2300 m) when diagnosed from IWV_{N08}. Moreover, the degree of enhancement shown in the right panel of Figures 4.1a and 4.1b greatly varies between catalogs. Overall, the understanding of the AR CS distribution and enhancement is tightly coupled to the AR detection method applied.

4.3.2 Inter-annual Variability

4.3.2.1 AR Cumulative Snowfall

Figure 4.2 quantifies the seasonal AR and non-AR CS volumes based on IWV_{N08} (top) and IVT_{GW15} (bottom). For a given year, the total CS (i.e. total height of the bar) in Figure 4.2 is equal in both panels; however, the partitioning between AR and non-AR CS is determined by the

AR detection method. Using IWV_{N08} (Figure 4.2, top), ARs yield ~6.8 km^3 of the 21.0 km^3 of total CS, on average, or ~32.5% of the CS annually. *Guan et al.* [2013a] characterized the seasonal AR CS depth using IWV_{N08} and in situ snow sensors over WYs 1998-2011. For 12 out of the 14 seasons in common with *Guan et al.* [2013a], lower f_{AR} values were estimated herein (Figure 4.2, top). Thus, the 14-year average f_{AR} value estimated herein is roughly 5% lower than their estimate of ~37%. Differences between these two studies should be expected because herein area-averaged 90-m CS was used to derive the CS volume, whereas *Guan et al.* [2013a] utilized point-scale CS depth observations. Therefore, the snowfall dataset used herein should provide a more robust representation of the range-wide impact of ARs than possible with point-scale observations. Using IWV_{N08} and a 1-km distributed SWE dataset, *Guan et al.* [2010] similarly estimated f_{AR} in the Sierra Nevada using CS depth during WYs 2004-2010. Each of their f_{AR} estimates was higher than herein, resulting in a 7-year average f_{AR} of 38.5% or ~9.4% more than estimated herein for those years. Although both studies used gridded snow datasets, a large scale disparity exists and the 90-m resolution framework can better represent the large heterogeneity of the snowfall that occurs within a 1-km grid.

Figure 4.2 demonstrates that ARs are important during both wet and dry years. The wettest year in the record was WY 2011 (40.6 km^3 of total CS), where ARs contributed an estimated 53.0% of the total CS based on IWV_{N08} (Figure 4.2, top). This corresponds to 21.6 km^3, or roughly equal to the 18-year average total CS, which clearly demonstrates that ARs contributed to making 2011 a very wet year. Interestingly, ARs contributed an estimated 63.1% of the total CS during WY 2015 (driest year) when only 5.1 km^3 of total CS occurred across the range. Moreover, without the occurrence of ARs, 2015 would have been an even drier year

receiving under 2 km^3 of CS. Similar relationships highlighting the importance of ARs are observed in Figure 4.2 (bottom) when IVT_{GW15} is examined.

Corresponding to the higher IVT_{GW15}-based AR CS depths in Figure 4.1b (left and middle), larger AR CS volumes are observed in Figure 4.2 (bottom) relative to IWV_{N08} (Figure 4.2, top). Based on IVT_{GW15} (Figure 4.2, bottom), the average seasonal AR CS is 11.9 km^3, which is ~1.8 times larger than estimated using IWV_{N08}. The AR CS ranged from 3.1 km^3 in WY 2015 to 23.0 km^3 in WY 2011. Although the AR catalogs yield relatively consistent f_{AR} values for these two years, the average f_{AR} values greatly differ between the catalogs: ~56.1% (IVT_{GW15}) vs. 32.5% (IWV_{N08}). ARs yielded a negligible contribution to the total CS in WY 2001 based on IWV_{N08}, whereas a contribution of ~35.8% was estimated using IVT_{GW15} for that year because winter storms were cool, having low IWV, but enhanced vapor transport. Both f_{AR} values were the lowest for each catalog. In both panels, the standard deviation of f_{AR} is large at 15.6% (IWV_{N08}) and 12.4% (IVT_{GW15}). When IVT_{GW15} is utilized, ~82% of the variance in the total CS is explained by the variability in AR CS. This is larger than the ~64% explained when IWV_{N08} is used. Overall, both catalogs indicate that ARs play an important role in driving the inter-annual variability of the total CS. Implications of using the CS-contributing days as opposed to the AR days when computing AR CS were examined in Section B.3 and Figures B.3-B.4.

4.3.2.2 Number of AR Days

While the contribution of ARs to the total CS is clearly significant, the attribution of CS to ARs greatly varies with the catalogs. Using IVT_{GW15}, ARs were estimated to contribute an average of 23.7% more of the seasonal CS. The main driver of the attribution difference is the number of AR days that each methodology identified (Figure 4.3, top). On average, IWV_{N08}

identified 10.1 AR days/year, while IVT_{GW15} identified over twice as many (21.7 AR days/year). Across the 18 winter seasons, ~6.6% and 14.2% of days were diagnosed as AR days by IWV_{N08} and IVT_{GW15}, respectively. Note that IWV is only available over the ocean from the SSM/I sensor and therefore, the length requirement used in IWV_{N08} is more restrictive than the same requirement when AR length can be computed over land and ocean.

Although IVT_{GW15} consistently identified more AR days than IWV_{N08}, the inter-annual variability shown in Figure 4.3 (top) is similar between approaches; there is a statistically significant correlation of 0.60 between the two time series ($p = 0.009$). It is not surprising to observe a difference in the number of AR days diagnosed by the two methods given differences in the physical variables, algorithms, and datasets/information (satellite vs. reanalysis) used to diagnose ARs. Previous studies [e.g. *Rutz et al.,* 2014; *Barth et al.,* 2017] have also shown that IVT methods tend to diagnose more AR days than with IWV across the western U.S.

4.3.3 Comparison of AR Dates Detected

Although Figure 4.3 (top) indicates that IWV_{N08} diagnosed fewer AR days than IVT_{GW15}, it does not provide insight into how frequently the catalogs identify the same AR days. For every day of the accumulation season across the 18 years, Figure 4.3 (bottom) shows when each method detected an AR. Using a ±1 day search window, *Guan and Waliser* [2015] found that 94% of the time that IWV_{N08} identified an AR day, IVT_{GW15} also identified an AR occurrence along western North America. Figure 4.3 (bottom) shows that although IVT_{GW15} often identified an AR when IWV_{N08} detected one, there were many ARs that IVT_{GW15} diagnosed that were not identified by IWV_{N08}. In total, IWV_{N08} diagnosed 182 AR days, which is 2.1 times fewer ARs than diagnosed by IVT_{GW15} (390 days). Based on IVT_{GW15}, the average duration of an AR event is

~1.7 days or only ~0.3 days longer than estimated by IWV_{N08}. It is important to recognize that these estimates were based on the presence of ARs across a region with a minimum duration of one day. This differs from other studies such as *Ralph et al.* [2013] who observed average AR duration at a fixed location to be sub-day.

Previous literature [e.g. *Lavers et al.*, 2012; *Guan and Waliser*, 2015; *Barth et al.*, 2017] has often taken IWV_{N08} to be the "reference" dataset even when IVT-based AR diagnoses were examined. Nonetheless, a similar question was asked herein: To what extent do the IVT_{GW15} detections agree with IWV_{N08}? However, the reverse was also posed herein to understand relative performance/agreement when each catalog was taken as the reference (defined in Section B.3). Hence, no assumption about whether one dataset is the "truth" was made.

Using Figure 4.3 (bottom), the number of hits, misses, false alarms, and correct negatives was tabulated in Table B.1. As shown in Table B.1, 63% of the time that IWV_{N08} detected an AR, IVT_{GW15} also detected one; however, only 29% of the time that IVT_{GW15} detected an AR did IWV_{N08} also diagnose the same AR day. The threat score indicates that 25% of the diagnosed ARs were detected by both datasets. Since IWV_{N08} diagnosed fewer ARs, its POFD was only 3% as opposed to 11% from IVT_{GW15}. As a result, the FAR of 71% for IVT_{GW15} was substantially higher than for IWV_{N08} (37%). While perfect agreement between datasets would mean that POD=1, POFD=0, and FAR=0, perfect agreement between approaches utilizing different physical quantities and detection considerations should not be expected. Therefore, open questions remain about how closely AR diagnoses should be expected to agree with one another when methodologies utilizing fundamentally different physical quantities and datasets are compared. Nonetheless, the two catalogs should be considered largely complementary to each other.

4.4 Conclusion

This study illustrates the importance of understanding the potential differences that the selection of an AR catalog can have on quantifying the AR CS over a region, such as the Sierra Nevada, where ARs deliver significant amounts of snowfall. Moreover, it indicates that open questions exist regarding the extent to which an AR identification methodology/catalog underestimates or overestimates a given process/mechanism. Although both catalogs used herein indicated that ARs were important for delivering CS to the mountain range, the relative contribution of ARs can be skewed by over 20% between the two methods. IVT_{GW15} diagnosed more AR days than IWV_{N08} and consequently its estimate of the AR contribution to the seasonal CS was larger. An average of 56% of the total range-wide CS was attributed to ARs when ARs were diagnosed from IVT_{GW15} vs. only 33% from IWV_{N08}. Regardless of the AR catalog used here, ARs were shown to yield greater orographic enhancement than non-AR mechanisms above ~2200 m across the windward side of the Sierra Nevada. However, AR CS consistently exhibited more enhancement across all elevations with IVT_{GW15} in both the NW and SW. Future studies should work toward a better understanding of how AR algorithms, datasets, and physical quantities (IWV vs. IVT) have implications on hydrological studies over a region. It is not only important to understand how ARs contribute to the snowfall accumulation, but also how they contribute to precipitation, streamflow, and flooding estimates given different AR diagnoses.

4.5 Figures

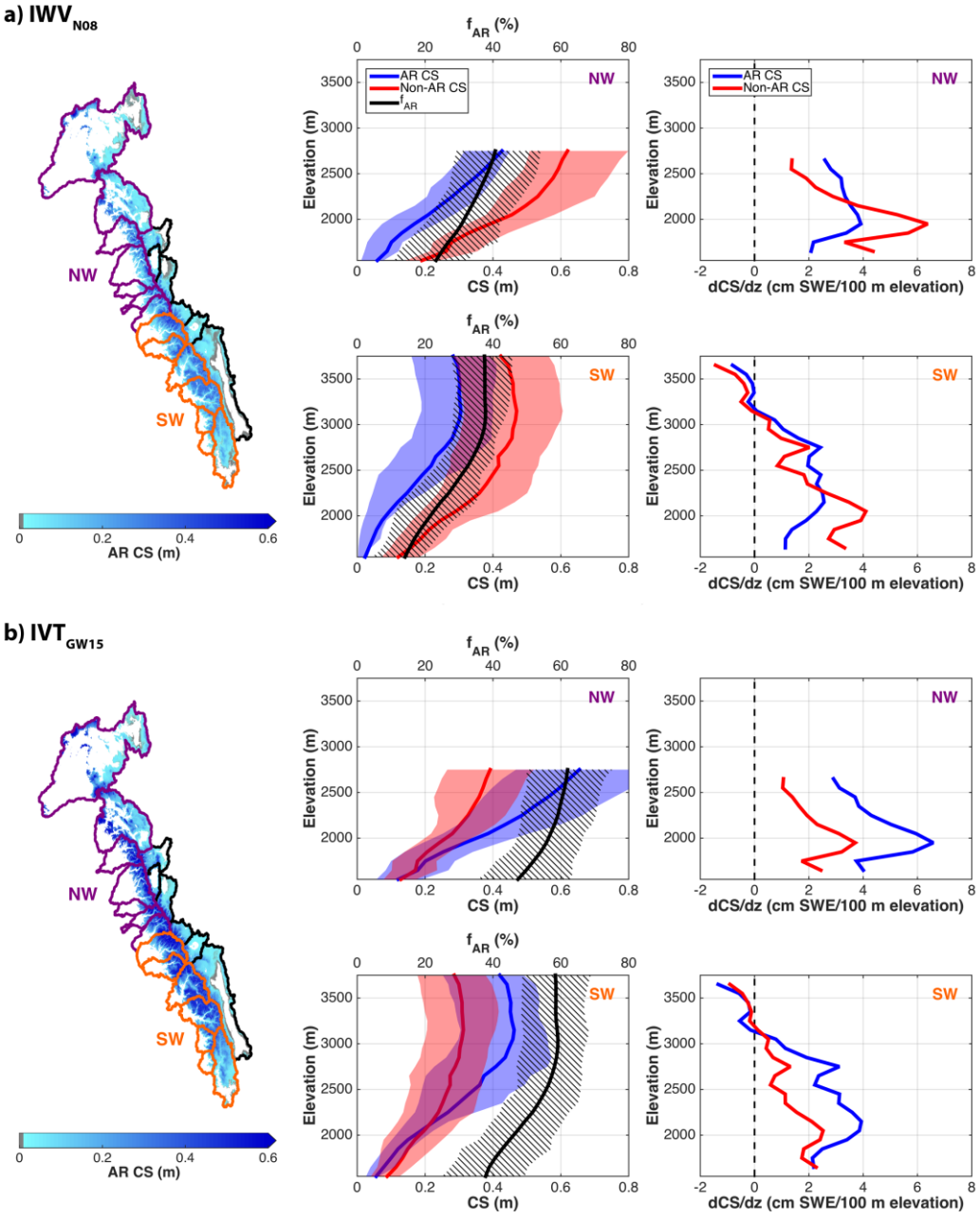

Figure 4.1. AR dates were derived from a) IWV_{N08} and b) IVT_{GW15} for: (left) Eighteen-year average AR CS distribution. (middle) Elevational distribution of AR (blue) and non-AR (red) CS using 100-m bins for NW and SW basins. Only bins representing over 0.5% of the area above 1500 m were considered [*Huning and Margulis*, 2017a,b]. The fraction of total CS derived from ARs (f_{AR}) is shown in black. Lines indicate the 18-year average. Shaded regions represent the interquartile range. (right) Rates of change of 18-year average AR and non-AR CS with elevation.

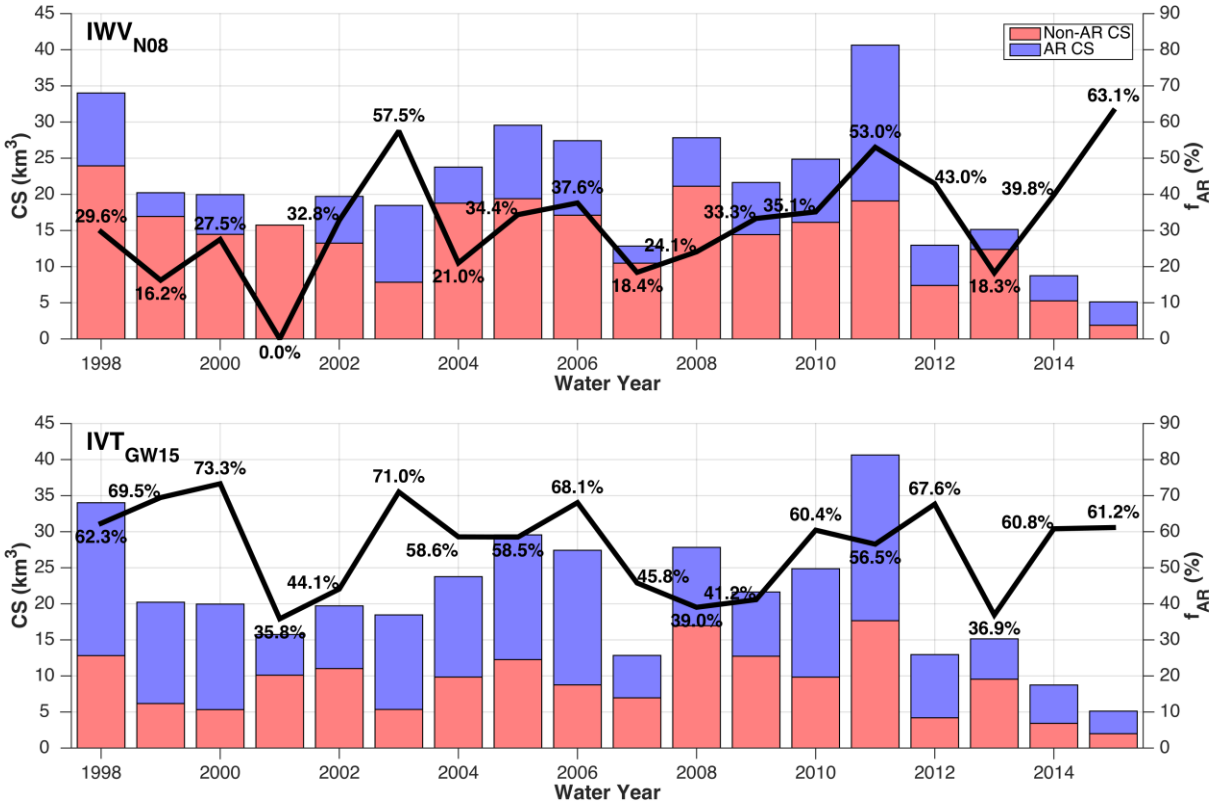

Figure 4.2. Range-wide CS time series (bars) with ARs derived from (top) IWV_{N08} and (bottom) IVT_{GW15}. Black curve denotes f_{AR}.

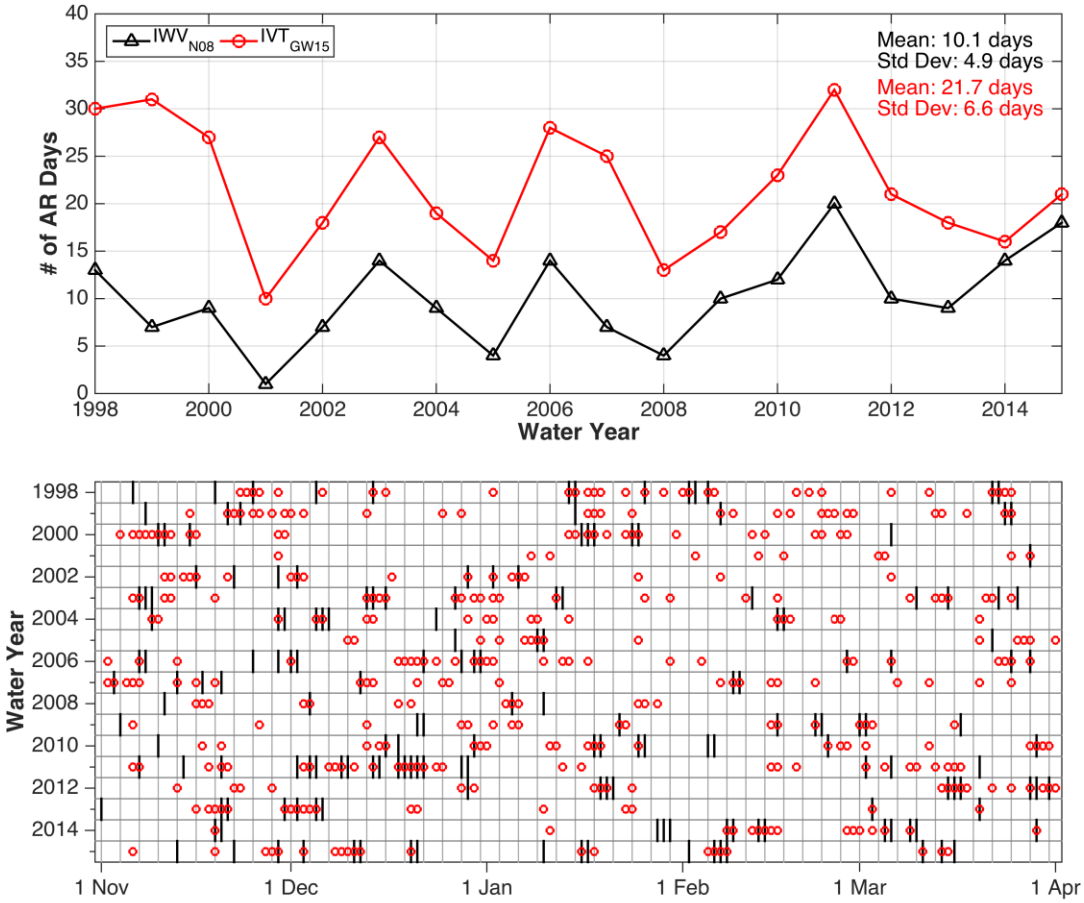

Figure 4.3. (top) Number of AR days diagnosed by IWV_{N08} (black) and IVT_{GW15} (red) during the winter season. (bottom) Time series showing the day an AR was identified with IWV_{N08} ('|' symbols) and IVT_{GW15} ('o' symbols), for each day of the winter season.

4.6 Bibliography

Barth, N. A., G. Villarini, M. A. Nayak, and K. White (2017), Mixed populations and annual flood frequency estimates in the western United States: The role of atmospheric rivers, *Water Resour. Res.*, 53, 257-269, doi:10.1002/2016WR019064.

Dee, D. P., and Coauthors (2011), The ERA-Interim reanalyses: Configuration and performance of the data assimilation system, *Q. J. Roy. Meteorol. Soc.*, 137, 553-597, doi:10.1002/qj.828.

Dettinger, M. D., F. M. Ralph, T. Das, P. J. Neiman, and D. R. Cayan (2011), Atmospheric rivers, floods and the water resources of California, *Water*, 3, 445-478, doi:10.3390/w3020445.

Guan, B., N. P. Molotch, D. E. Waliser, E. J. Fetzer, and P. J. Neiman (2010), Extreme snowfall events linked to atmospheric rivers and surface air temperature via satellite measurements, *Geophys. Res. Lett.*, 37, L20401, doi:10.1029/2010GL044696.

Guan, B., N. P. Molotch, D. E. Waliser, E. J. Fetzer, and P. J. Neiman (2013a), The 2010/2011 snow season in California's Sierra Nevada: Role of atmospheric rivers and modes of large-scale variability, *Water Resour. Res.*, 49, 6731-6743, doi:10.1002/wrcr.20537.

Guan, B., N. P. Molotch, D. E. Waliser, S. M. Jepsen, T. H. Painter, and J. Dozier (2013b), Snow water equivalent in the Sierra Nevada: Blending snow sensor observations with snowmelt model simulations, *Water Resour. Res.*, 49, 5029-5046, doi:10.1029/wrcr.20387.

Guan, B., and D. E. Waliser (2015), Detection of atmospheric rivers: Evaluation and application of an algorithm for global studies, *J. Geophys. Res. Atmos.*, 120, 12514-12535, doi:10.2002/2015JD024257.

Guan, B., D. E. Waliser, N. P. Molotch, E. J. Fetzer, and P. J. Neiman (2012), Does the Madden-Julian Oscillation influence wintertime atmospheric rivers and snowpack in the Sierra Nevada? *Mon. Wea. Rev.*, 140, 325–342, doi: 10.1175/MWR-D-11-00087.1.

Guan, B., D. E. Waliser, F. M. Ralph, E. J. Fetzer, and P. J. Neiman (2016), Hydrometeorological characteristics of rain-on-snow events associated with atmospheric rivers, *Geophys. Res. Lett.*, doi:10.1002/2016GL067978.

Huning, L. S., and S. A. Margulis (2017a), Investigating the variability of high-elevation seasonal orographic snowfall enhancement and its drivers across Sierra Nevada, California, *J. Hydrometeor.*, in review.

Huning, L. S., and S. A. Margulis (2017b), Climatology of seasonal snowfall accumulation across the Sierra Nevada (USA): Accumulation rates, distributions, and variability, *Water Resour. Res.*, in review.

Kim, J., D. E. Waliser, P. J. Neiman, B. Guan, J.-M. Ryoo, and G. A. Wick (2013), Effects of atmospheric river landfalls on the cold season, *Clim. Dyn.*, 40, 465-474, doi:10.1007/s00382-012-1322-3.

Lavers, D. A., G. Villarini, R. P. Allan, E. F. Wood, and A. J. Wade (2012), The detection of atmospheric rivers in atmospheric reanalyses and their links to British winter floods and the large-scale climatic circulation, *J. Geophys. Res.*, 117, D20106, doi:10.1029/2012JD018027.

Margulis, S., G. Cortés, M. Girotto, and M. Durand (2016), A Landsat-era Sierra Nevada (USA) snow reanalysis (1985-2015), *J. Hydrometeor.*, 17, 1203-1221, doi:10.1175/JHM-D-15-0177.1.

Margulis, S., M. Girotto, G. Cortés, and M. Durand (2015), A particle batch smoother approach to snow water equivalent estimation, *J. Hydrometeor.*, 16, 1752-1722, doi:10.1175/JHM-D-14-0177.1.

Neiman, P. J., F. M. Ralph, G. A. Wick, J. D. Lundquist, and M. D. Dettinger (2008), Meteorological characteristics and overland precipitation impacts of atmospheric rivers affecting the West Coast of North America based on eight years of SSM/I satellite observations, *J. Hydrometeor.*, 9, 22-47, doi:10.1175/2007JHM855.1.

O'Hara, B. F., M. L. Kaplan, and S. J. Underwood (2009), Synoptic climatology analyses of extreme snowfalls in the Sierra Nevada, *Wea. Forecasting*, 24, 1610-1624, doi:10.1175/2009WAF2222249.1.

Ralph, F. M., T. Coleman, P. J. Neiman, R. J. Zamora, and M. D. Dettinger (2013), Observed impacts of duration and seasonality of atmospheric-river landfalls on soil moisture and runoff in coastal Northern California, *J. Hydrometeor.*, 14, 443-459, doi:10.1175/JHM-D-076.1.

Ralph, F. M., J. M. Cordeira, P. J. Neiman, and M. Hughes (2016), Landfalling atmospheric rivers, the Sierra barrier jet, and extreme daily precipitation in northern California's Upper Sacramento River watershed, *J. Hydrometeor.*, 17, 1905-1914, doi:10.1175/JHM-D-15-0167.1.

Ralph, F. M., P. J. Neiman, G. A. Wick (2004), Satellite and CALJET aircraft observations of atmospheric rivers over the eastern north Pacific Ocean during the winter of 1997/98, *Mon. Wea. Rev.*, 132, 1721-1745.

Ralph, F. M., P. J. Neiman, G. A. Wick, S. I. Gutman, M. D. Dettinger, D. R. Cayan, and A. B. White (2006), Flooding on California's Russian River: Role of atmospheric rivers, *Geophys. Res. Lett.*, 33, L13801, doi:10.1029/2006GL026689.

Rutz, J. J., and W. J. Steenburgh (2012), Quantifying the role of atmospheric rivers in the interior western United States, *Atmos. Sci. Lett.*, 13, 257-261, doi:10.1002/asl.392.

Rutz, J. J., W. J. Steenburgh, and F. M. Ralph (2014), Climatological characteristics of atmospheric rivers and their inland penetration over the Western United States, *Mon. Wea. Rev.*, 142, 905-921, doi:10.1175/MWR-D-13-00168.1.

Serreze, M. C., M. P. Clark, and A. Frei (2001), Characteristics of large snowfall events in the montane western United States as examined using snowpack telemetry (SNOTEL) data, *Water Resour. Res.*, 37(3), 675-688.

Wilks, D. S. (2006), *Statistical methods in the atmospheric sciences*, 2nd ed., Academic Press, San Diego, CA, 627 pp.

Chapter 5: Conclusion and Future Work

5.1 Original Contributions and Notable Findings

The results from this dissertation provide improved characterizations of the montane snowfall accumulation that complement previous work across the Sierra Nevada and other snow-dominated mountain ranges. With the extensive validation of the cumulative snowfall (CS) dataset derived herein from the snow reanalysis [*Margulis et al.,* 2016], it was demonstrated that the reanalysis could be utilized as an accurate CS dataset. Thus, the potential utility of the snow reanalysis has been extended beyond its original peak snow water equivalent (SWE) applications. This is important because a high-resolution snowfall dataset provides different insight into snow processes that cannot be obtained by simply analyzing peak SWE. For example, understanding snowfall accumulation rates and distributions could be used to improve models and/or forecasts for water resources, weather, avalanches, climate, etc. applications in mountainous terrain. Moreover, its use in this dissertation enabled the seasonally-integrated CS volume to be characterized (inter-annual variability, climatology, etc.), which remained previously unquantified likely because it cannot be estimated with in situ measurements alone.

One of the overarching novelties of this work is the addition of the high-resolution spatial dimension of snowfall analysis across an entire mountain range, which has been utilized to yield in-depth insight into the snowfall climatology and inter-annual variability (including the CS volume), accumulation rates, orographic snowfall enhancement, atmospheric river (AR)-derived CS, etc. The results provided herein have thereby aided in developing a more complete picture of montane hydrometeorological processes. For instance, rather than using a range-wide approach to analyze snowstorm timing and seasonality as done in many previous studies, basin-wide snowstorms were examined in this study to better understand regional and basin responses. This

analysis was performed with a new approach allowing for the diagnosis of variable duration storms. A variable duration storm can better capture characteristics of the largest snowstorms (e.g. CS amount and storm duration) than a fixed duration (e.g. 3-day) storm, which may misrepresent CS amounts.

The degree to which the hydroclimatology of the Sierra Nevada is driven by extremes was not only demonstrated by comparing the differences in snowfall distributions and snowstorms, but also through specific investigations of wet-year and dry-year orographic CS gradients. This dissertation provides an unprecedented analysis and database of orographic snowfall gradients spanning over three decades across the entire windward side of a mountain range. The extent to which snowfall during wet years is more orographically enhanced than dry years was quantified in this study. Results revealed that CS during wet years is about twice as enhanced as during dry years due to differences in large-scale atmospheric drivers of the enhancement. Not only was the orographic CS curve as it varies across the entire western Sierra Nevada shown to take on two distinct shapes, but the elevation of the maximum CS that occurred for each basin, annually, was found to be relatively static over the 31 study years. Such findings indicate that there is potential for the development of orographic snowfall parameterizations and predictability.

Lastly, this dissertation investigated the extent to which the diagnosed contribution of ARs to the seasonal CS is related to the AR detection approach utilized. Not only can one method indicate that ARs are nearly twice as important as another method indicates, in terms of AR contributions to the seasonal CS, but results also show that the detection methods impact the understanding of the AR-driven orographic enhancement. The analysis and results presented above serve as a key step forward in understanding how a meteorological diagnosis can have implications in hydrological studies. It serves as a cautionary example of how the selection of

algorithms and datasets can skew and/or modulate the relative importance that is attributed to a given process. Overall, these findings are important for interpreting previous and future hydrological studies related to ARs and snowfall. While results confirm that ARs are significant drivers of snowfall across the Sierra Nevada, they also highlight future areas of research. The findings from this dissertation have the potential to inform AR tracking and detection algorithms that are used in applications including hydrology, water resources, weather forecasting, climate analysis, etc.

5.2 Future Work

This dissertation provides the foundation for several future investigations across snow-covered mountainous terrain. Some of these potential research directions are described below.

5.2.1 Near-term Extensions

In addition to increasing the amount of water stored in the snowpack, extreme weather events such as snowstorms can have significant economic and/or human effects, inhibit travel, etc. [*Grumm and Hart,* 2001; *O'Hara et al.,* 2009]. Therefore, it would be useful to examine extreme snowstorm events and understand the return periods of different sized storms. This is particularly timely for California given the many ARs that occurred during this winter, i.e. 2017, following the significant multi-year snowpack drought deficit 2012-2016 in the Sierra Nevada. Moreover, storm-scale analysis would provide a complement to the longer scales already examined herein. Orographic analysis at shorter scales (e.g. daily, multi-day storm) would provide sub-seasonal insight and a better understanding of the factors that contribute to the seasonal patterns discussed in this dissertation. This work could be extended to include analysis of rainfall and total precipitation distributions, rain-on-snow events, spatial patterns and temporal

trends, the influence of barrier jets on the precipitation distribution, etc. at sub-seasonal to climatological scales.

Utilizing insight into the relationship between atmospheric drivers of orographic enhancement and the CS gradients, orographic snowfall parameterizations could be derived from this dissertation. Such models could have several potential applications including: statistical downscaling, predicting future changes in orographic CS, estimating the snowfall distribution using point-scale in situ measurements, etc.

The two AR catalogs compared in Chapter 4 were chosen to represent both a traditional and more recent approach to diagnosing ARs while providing insight into how different diagnoses can influence snowfall attribution and hydrological analysis. Although this comparison provided meaningful insight, further evaluations and comparisons between AR catalogs are warranted. It is important not only to accurately diagnose atmospheric phenomena, but also to better understand how atmospheric/meteorological diagnoses impact hydrological studies. Similar evaluations to those provided above could be made between AR catalogs that utilize the same algorithm, but were derived from a variety of different atmospheric datasets.

5.2.2 Long-term Extensions

One overarching motivation of the analyses performed in this dissertation is to provide insight into the snowfall distribution that could be utilized by water resources managers. Hence, an extension of this dissertation could include integrating high-resolution snowfall information, orographic snowfall parameterizations, etc. with existing water management assessments and models. As shown above, models relating the number of snowstorms and snow storm days can be used to estimate the CS volume, which is generally difficult to quantify for the mountain range. Moreover, the findings provided herein could be combined with other datasets/data streams, e.g. satellite-based remote sensing, snow measurements from wireless in situ snow

networks, etc., to improve the spatial and temporal representation of snow processes and hydrometeorology across mountainous terrain and derive high-resolution, distributed, near-real time snowpack information for a variety of applications.

While orographically-driven snowfall distributions and orographic CS gradients were studied along the windward side of the Sierra Nevada, there is also value in understanding the extent to which the CS patterns on the leeward side may differ with those quantified on the windward side because basins on both sides of the mountain range supply water to large populations. Since storms generally move across California with the prevailing westerlies, it would be valuable to examine the predictability of precipitation patterns on the leeward side given upstream estimates of atmospheric fields that are more easily quantifiable and predictable along the windward side of the range.

Another major thrust of this dissertation was to enhance the current knowledge of snow hydrology (seasonality, inter-annual variability, elevational/spatial distribution) that is not well resolved at regional (or global) resolutions nor well represented at the point-scale. As a result, historical databases of orographic snowfall gradients, snowstorm characteristics, snowfall distributions, etc. were produced as part of this dissertation. These databases and corresponding insight could be utilized to evaluate cold season accumulation parameterizations and validate regional climate model (RCM) simulations. The findings herein would provide detailed pictures of snowfall occurring at the subgrid-scale of a RCM. Moreover, these datasets would provide a more robust validation approach for climate model output than the traditional verification, which verifies large-scale area-averaged quantities with point-scale measurements: fundamentally different quantities with a large spatial disparity. Ultimately extensions of this work should move toward not simply identifying climate model deficiencies, but rather also improving the representation of snowstorm frequency, duration, timing, and snowfall amounts as well as

snowfall patterns, orographic snowfall distributions/gradients, accumulation rates, and meteorological drivers of snowfall accumulation in climate models. Ultimately, novel parameterizations derived from this work (as described above) can be incorporated into regional and/or global climate models to improve their simulations over snow-dominated mountainous terrain.

While this dissertation focused on understanding snowfall processes and distributions during the accumulation season, it is important to understand how differences in the accumulation season manifest themselves in melt season variability. Thus paralleling the historical accumulation season analyses performed in this study, historical melt season analyses could similarly be performed to better characterize the ablation season as well as understand the connection between the accumulation and melt seasons and ultimately streamflow.

5.3 Bibliography

Grumm, R. H., and R. Hart (2001), Standardized anomalies applied to significant cold season weather events: Preliminary findings, *Wea. Forecasting*, 16, 736-754, doi:10.1175/1520-0434(2001)016<0736:SAATSC>2.0.CO;2.

Margulis, S., G. Cortés, M. Girotto, and M. Durand (2016), A Landsat-era Sierra Nevada (USA) snow reanalysis (1985-2015), *J. Hydrometeor.*, 17, 1203-1221, doi:10.1175/JHM-D-15-0177.1.

O'Hara, B. F., M. L. Kaplan, and S. J. Underwood (2009), Synoptic climatology analyses of extreme snowfalls in the Sierra Nevada, *Wea. Forecasting*, 24, 1610-1624, doi:10.1175/2009WAF2222249.1.

Appendix A: Supporting Information for Climatology of Seasonal Snowfall Accumulation across the Sierra Nevada (USA): Accumulation Rates, Distributions, and Variability

A.1 Introduction

This appendix provides supporting information for Chapter 2. It contains a map of the elevations across the Sierra Nevada study domain and the distribution of elevations across the study basins above 1500 m (Figure A.1). A description of the Sierra Nevada snow water equivalent (SWE) reanalysis and an explanation of the methods applied to quality control the snow pillow observations for the cumulative snowfall (CS) verification are provided in Sections A.2 and A.3, respectively. Figure A.2 provides information about the distribution of storm durations and sizes for all snowstorms and leading snowstorms identified across the 31 study years.

A.2 Sierra Nevada Snow Water Equivalent Reanalysis

The snow reanalysis was developed using a particle batch smoother data assimilation approach, which is detailed in *Margulis et al.* [2015] and briefly described here. Uncertainty was added to near-surface meteorological forcings (e.g. precipitation, humidity, air temperature, etc.) derived from the National Land Data Assimilation System phase 2 dataset (NLDAS-2, *Xia et al.*, 2012) to form an ensemble of meteorological inputs for a forward model run. Within a Bayesian framework, the ensemble of land surface estimates (i.e. the prior) was conditioned using Landsat fractional snow covered area (fSCA) images. It is important to note that although NLDAS-2 relies heavily on the North American Regional Reanalysis (NARR, *Mesinger et al.*, 2006) for many surface forcing variables, its precipitation fields are *not* derived from NARR. Rather, its

precipitation fields are derived from precipitation gauges in the NOAA Climate Prediction Center (CPC) network (i.e. observational data). Therefore, precipitation timing in the SWE reanalysis is implicitly derived from the CPC precipitation gauges.

The prior uncertainty in precipitation was represented by scaling NLDAS-2 precipitation by an ensemble of equally likely seasonally invariant multiplicative factors (drawn from a lognormal distribution) for each pixel. The posterior estimates were obtained via updated weights for each ensemble member derived using a likelihood function that assigned larger weights to ensemble predictions that were more likely, or closer to the observations, while reducing the weights for the predictions that were less probable, or farther from the observations. While this approach utilized information derived from the fSCA images (primarily during the ablation season), it yielded state estimates throughout the entire season. Due to the multiplicative nature of the scaling factors, only storms present in the prior (implicitly those observed in the CPC network) can be present in the posterior SWE reanalysis. Storm durations as estimated by the posterior SWE fields cannot exceed those present in the prior. Thus, snowfall timing cannot be adjusted (i.e. storms cannot be "created") and snowfall events can only be shortened, not extended in duration. In addition, a fixed air temperature threshold of 2°C [*Lundquist et al.*, 2008] was used to partition precipitation into rainfall or snowfall at a given time. The snow reanalysis provides estimates of the daily net effect of precipitation on the snowpack. It both downscales a coarse set of atmospheric forcings *and* bias corrects them.

A.3 Snow Pillow Quality Control Methods

Based on the techniques described in *Lundquist et al.* [2015], we applied quality control to the snow pillows at both the daily and seasonal time scales from 1 November-1 April as described below. Snowfall (S) was designated as missing on days for:

1) an unrealistic snowfall (i.e. $S > 140\,\text{mm}$) or

2) three sequential days with repeated snowfall values (i.e. $S(t) = S(t-1) = S(t-2)$).

Stations were excluded from the seasonal CS verification if:

1) no snowfall occurred by 1 April,

2) more than 30% of the days between 1 November and 1 April were excluded as missing data,

3) the station accumulated 100% of its season total CS prior to the median of the snow pillows achieving 40% of its season total CS, or

4) the station accumulated no snowfall by the day the median of the snow pillows accumulated 60% of the seasonal CS

because the sensor was assumed to have broken either during part of or throughout the entire season.

The representative pixel chosen for comparison used the same approach as in *Margulis et al.* [2016a] or *M16a*, which was utilized to account for uncertainties in geolocation and representativeness (i.e. physiographic characteristics, scale discrepancies, localized wind-blown effects, etc.). For consistency, days or years that were excluded from the snow pillow time series were also removed from the reanalysis time series. Daily accumulated snowfall values of less than 0.254 cm were removed from the snow reanalysis dataset to simulate the resolution of a sensor [*Serreze et al.*, 2001].

A.4 Figures

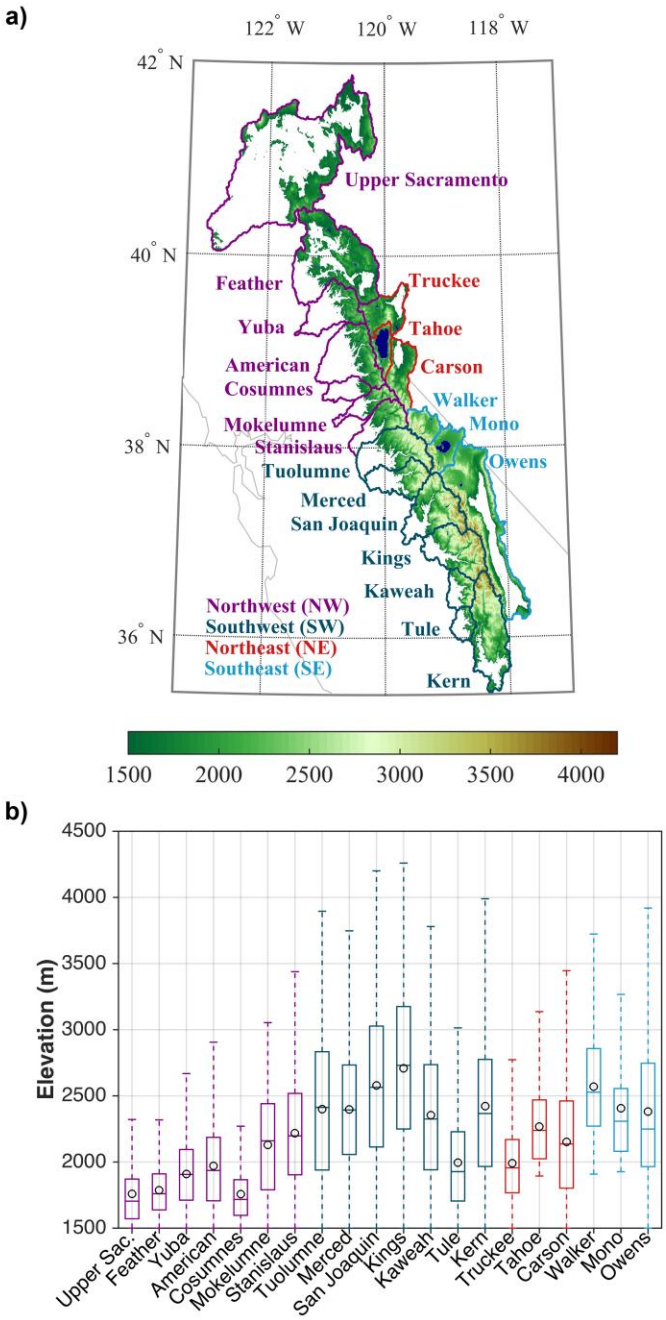

Figure A.1. a) Elevation map (in meters) over the Sierra Nevada (90-m resolution) where major watersheds are identified. Elevations at or below 1500 m and pixels outside of the study domain are colored white. b) Distribution of elevations for each basin above 1500 m. Dashed lines extend to the most extreme elevations not considering outliers (not shown). Black circles demarcate mean elevations. Color coding here designates regional information used in subsequent figures where basins have been grouped into the northwest (NW), southwest (SW), northeast (NE), and southeast (SE).

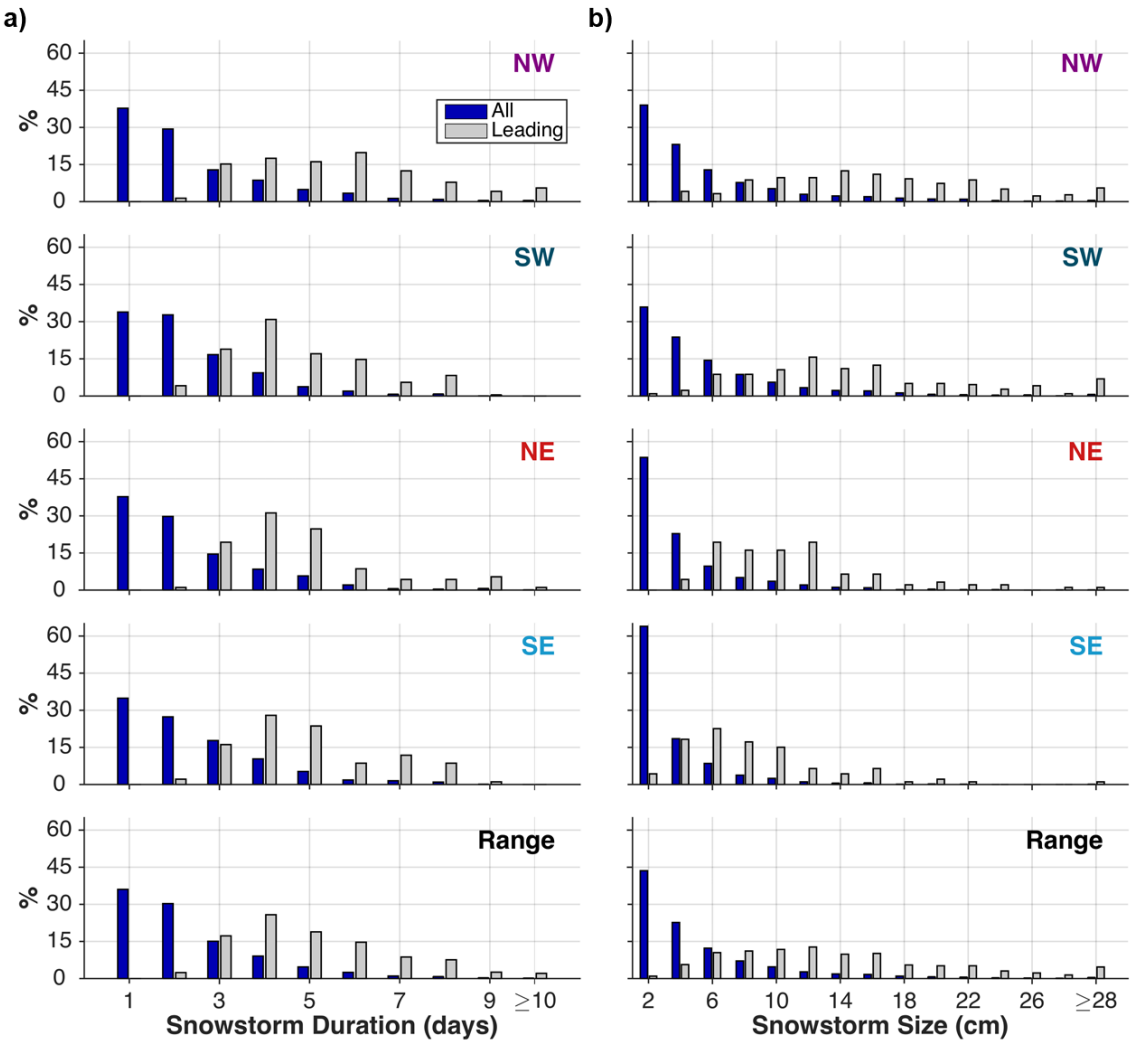

Figure A.2. Regional distribution of snowstorm a) duration and b) size for all basin-wide storms and leading storms over the 31 years. Daily bins were used for the durations in a). Snowstorm sizes were grouped in 2-cm bins in b), where the bars were centered on the upper limit of the bins (e.g. the first set of bars represents snowstorm sizes $0 \le x < 2\,\text{cm}$), except at the far right (i.e. $x \ge 28\,\text{cm}$). In each panel, blue and gray bars represent all basin-wide snowstorms and leading snowstorms over the 31 years, respectively.

A.5 Bibliography

Lundquist, J., M. Hughes, B. Henn, E. Gutmann, B. Livenh, J. Dozier, and P. Neiman (2015), High-elevation precipitation patterns: Using snow measurements to assess daily gridded datasets across the Sierra Nevada, California, *J. Hydrometeor.*, 16, 1773-1792 doi:10.1175/JHM-D-15-0019.1.

Lundquist, J. D., P. J. Neiman, B. Martner, A. B. White, D. J. Gottas, and F. M. Ralph (2008), Rain versus snow in the Sierra Nevada, California: Comparing Doppler profiling radar observations of melting level, *J. Hydrometeor.*, 9, 194-211, doi:10.1175/2007/JHM853.1.

Margulis, S., G. Cortés, M. Girotto, and M. Durand (2016a), A Landsat-era Sierra Nevada (USA) snow reanalysis (1985-2015), *J. Hydrometeor.*, 17, 1203-1221, doi:10.1175/JHM-D-15-0177.1.

Margulis, S. A., M. Girotto, G. Cortés, and M. Durand (2015), A particle batch smoother approach to snow water equivalent estimation, *J. Hydrometeor.*, 16, 1752-1722, doi:10.1175/JHM-D-14-0177.1.

Mesinger, F., and Coauthors (2006), North American Regional Reanalysis, *Bull. Amer. Meteor. Soc.*, 87, 343-360, doi:10.1175/BAMS-87-3-343.

Serreze, M. C., M. P. Clark, and A. Frei (2001), Characteristics of large snowfall events in the montane western United States as examined using snowpack telemetry (SNOTEL) data, *Water Resour. Res.*, 37(3), 675-688.

Xia, Y., and Coauthors (2012), Continental-scale water and energy flux analysis and validation for the North American Land Data Assimilation System project phase 2 (NLDAS-2): 1. Intercomparison and application of model products, *J. Geophys. Res.*, 117, D3, 1984-2012, doi:10.1029/2011JD016048.

Appendix B: Supporting Information for Implications of Atmospheric River Detection Methods on Characterizing Their Contribution to Seasonal Snowfall across the Sierra Nevada (USA)

B.1 Introduction

This appendix provides supporting information for Chapter 4. It contains an elevation map across the Sierra Nevada study domain (Figure B.1). Terminology used in the contingency table (Table B.1) and atmospheric river (AR) detection statistics is defined in Section B.2. Figure B.2 shows the 18-winter average total cumulative snowfall (CS) climatology across the range between water year (WY) 1998 and 2015, inclusive. Section B.3 explores the impact of utilizing one day before and one day after an AR event is detected on the amount of AR CS that is estimated. Figures B.3 and B.4 quantify the impact of the number of CS-contributing days on the AR CS estimates and the AR CS contribution to the total CS (f_{AR}), respectively. Table B.1 compares the number of AR hits, false alarms, misses, and correct negative diagnoses and corresponding detection statistics between the two AR catalogs (i.e. IWV_{N08} and IVT_{GW15}).

B.2 AR Detection Statistics

Following *Wilks* [2006], the relationship between ARs as diagnosed by IWV_{N08} and IVT_{GW15} was examined. Although contingency tables commonly use the term "observation", instead the term "reference" was used herein to refer to the AR catalog that is being compared to. Also, rather than using the term "forecast", the term "estimate" was used herein to refer to the second AR catalog since neither AR catalog is a forecast (i.e. satellite-derived and reanalysis-

derived diagnoses). Both the case where IWV_{N08} was taken to be the reference dataset as well as the case where IVT_{GW15} was taken to be the reference dataset were considered. A "false alarm" is defined as the number of days that an AR was estimated, but was not "observed" by the reference. Note that herein the term "observed" was used to refer to an AR that was detected or diagnosed by the reference, while the term "estimated" referred to the AR diagnosed by the second AR catalog. The false alarm ratio (FAR) is defined as the ratio of the number of false alarms to the number of total ARs estimated. Since throughout the year non-AR days (i.e. non-occurrences) are more common than AR days (i.e. occurrences), the threat score was used to quantify the number of correct ARs estimated (i.e. agreement on AR occurrence diagnoses or "hits") relative to the total number of times that an AR was estimated and/or observed. A "miss" is taken to be the number of times that an AR was observed, but not estimated. While a hit indicates that an AR was correctly estimated (i.e. it was also observed), a "correct negative" indicates that the estimate correctly diagnosed a non-AR day. The probability of detection (POD) is defined as the ratio of the number of correct AR estimates to the number of times that an AR day was observed. POD ranges from 0 to 1, where a value of unity indicates perfect agreement. The probability of false detection (POFD) is defined as the total number of false AR days relative to the total number of non-AR days observed. POFD ranges from 0 (perfect agreement) to 1.

B.3 Implications of Lead- and Lag-Time on AR CS Estimates

It is important to note that Figures 4.1-4.2 were generated using CS-contributing days, which follows the assumption that the ±1 day window should be utilized to account for lead- and lag-time differences between when an AR is diagnosed (Figure 4.3) and when snowfall occurs. Here, the extent to which the ±1 day window around an AR event impacts the amount of the

seasonal CS that is attributed to ARs at both the inter-annual and climatological scales was examined. The following terminology was defined to explore how the seasonal AR CS can be broken down into occurring on days when an AR was diagnosed vs. adjacent days in the larger window of time. The term "during" is used to refer to the day of the diagnosed AR (i.e. AR days shown in Figure 4.3). "Before" and "after" refer to the day before and the day after an AR event, respectively. A day classified as "overlap" is one that occurred the day after one AR event and the day before another AR event. Therefore, the overlapping day is the day that falls between two AR events that are separated by a single day. Days were not double counted. The designation of "all" days considers each day that falls into one of the abovementioned categories (i.e. before, during, and after an AR event and overlap).

Figure B.3 indicates that the largest amount of AR CS occurs during diagnosed AR events with an average of 3.7 km^3 (IWV_{N08}) and 7.0 km^3 (IVT_{GW15}) of AR CS accumulating on AR days each winter. While the number of CS-contributing days that occur before and after an AR event is equal, the amount of AR CS that occurs the day after an AR event tends to be greater than the amount that occurs the day before. This is observed using both AR catalogs. Over the course of a season, ~0.7 km^3 of AR CS occurs on days before the AR event, while ~2.2 km^3 tends to accumulate after the event when using IWV_{N08}. Using IVT_{GW15}, an average 1.2 km^3 and 3.1 km^3 of AR CS occurs before and after an AR event, respectively. The inclusion of these days (and the overlapping days) results in a larger contribution in terms of the AR CS volume based on IVT_{GW15} than with IWV_{N08}. About 2.6-2.9 times more AR CS occurs throughout a season on the day after than the day before, on average. On average, the inclusion of all CS-contributing days results in ~3.0 km^3 and 4.9 km^3 more AR CS annually than by only considering the (diagnosed) AR days for IWV_{N08} and IVT_{GW15}, respectively. Therefore including

the ±1 day window results in ~1.7-1.8 times more AR-derived CS than only considering the exact AR days shown in Figure 4.3.

Figure B.4 illustrates the extent that the inter-annual f_{AR} percentages are related to the ±1 day window. In Figure B.4 (top), the black (IWV_{N08}) and red (IVT_{GW15}) curves are the same as the f_{AR} time series provided in Figure 4.3 in the top and bottom panels, respectively. The gray and light red curves show the reduction in the total CS that is attributed to ARs for IWV_{N08} and IVT_{GW15}, respectively, when only the AR days were considered (i.e. not the CS-contributing days). This can result in a reduction of f_{AR} from 0.0-25.6% (IWV_{N08}) and 8.5-37.0% (IVT_{GW15}) for individual years. In this case, the average f_{AR} values are 17.8% and 32.5% using IWV_{N08} and IVT_{GW15}, respectively.

B.4 Tables

Table B.1. Contingency table and AR detection statistics (defined in Section B.2) for IWV_{N08} and IVT_{GW15}.

Reference	Estimate	Hits	False Alarms	Misses	Correct Negatives	Threat Score	FAR	POD	POFD
IWV_{N08}	IVT_{GW15}	114	276	68	2282	0.25	0.71	0.63	0.11
IVT_{GW15}	IWV_{N08}	114	68	276	2282	0.25	0.37	0.29	0.03

B.5 Figures

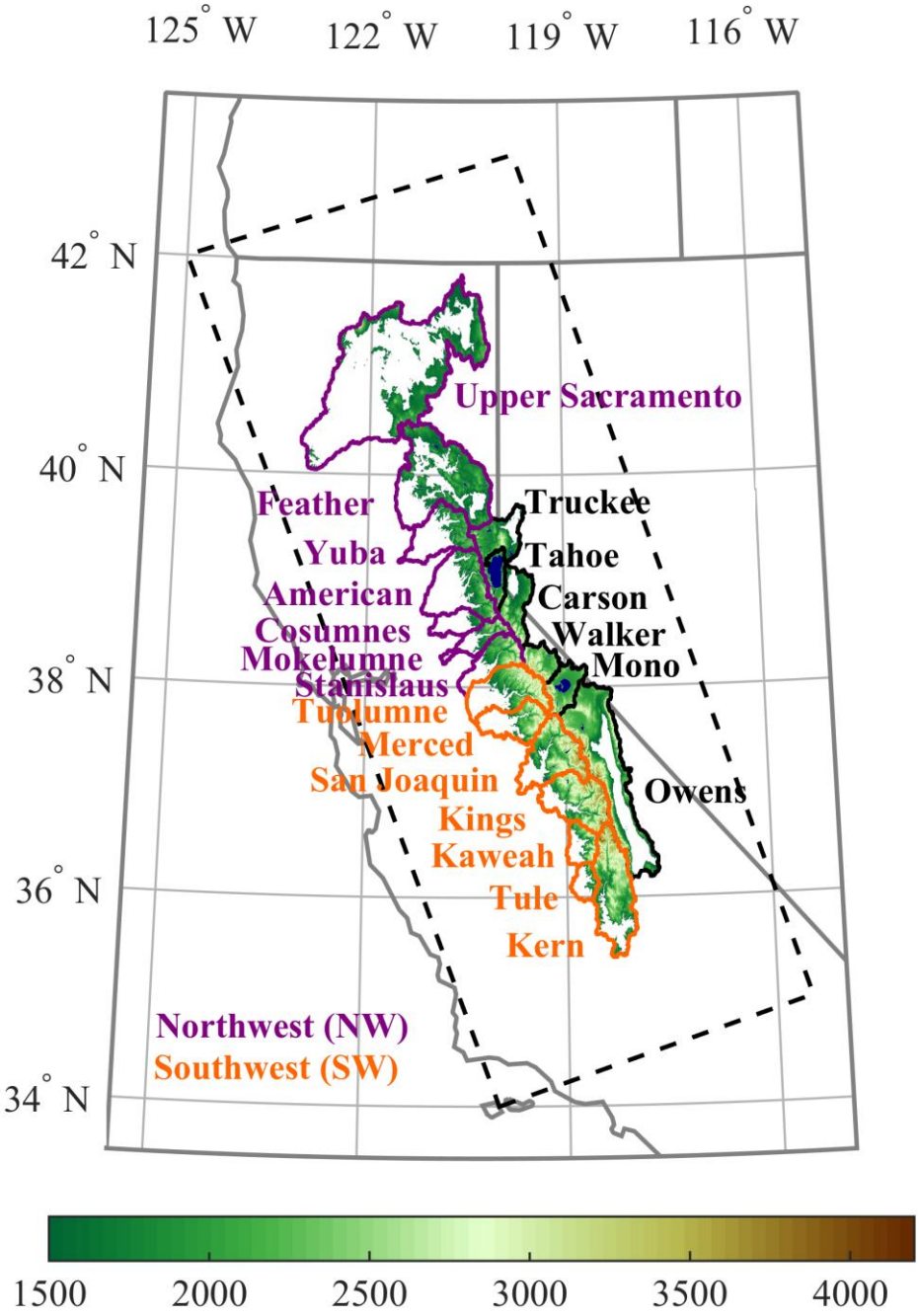

Figure B.1. Elevation map (in meters) identifying 20 major basins over the Sierra Nevada at 90-m resolution. Windward basins used in the orographic CS analysis are highlighted and grouped into the northwest (NW) and southwest (SW) regions. White regions represent pixels outside of the study domain or with elevations at or below 1500 m. Dashed lines demarcate the region used to identify AR occurrence from the IVT_{GW15} AR catalog used herein and defined later.

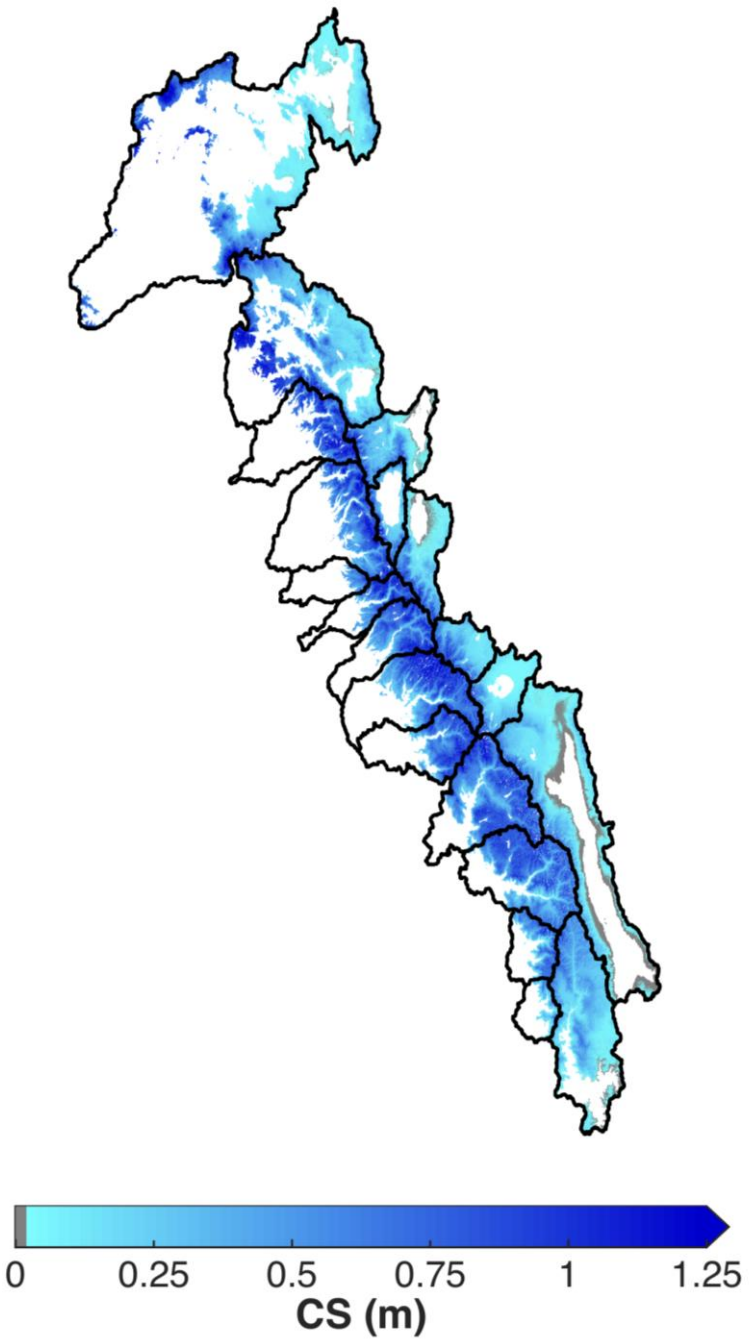

Figure B.2. Eighteen-year (WY 1998-2015) average total CS distribution. Total CS is the sum of the AR and non-AR contributions to CS during the winter.

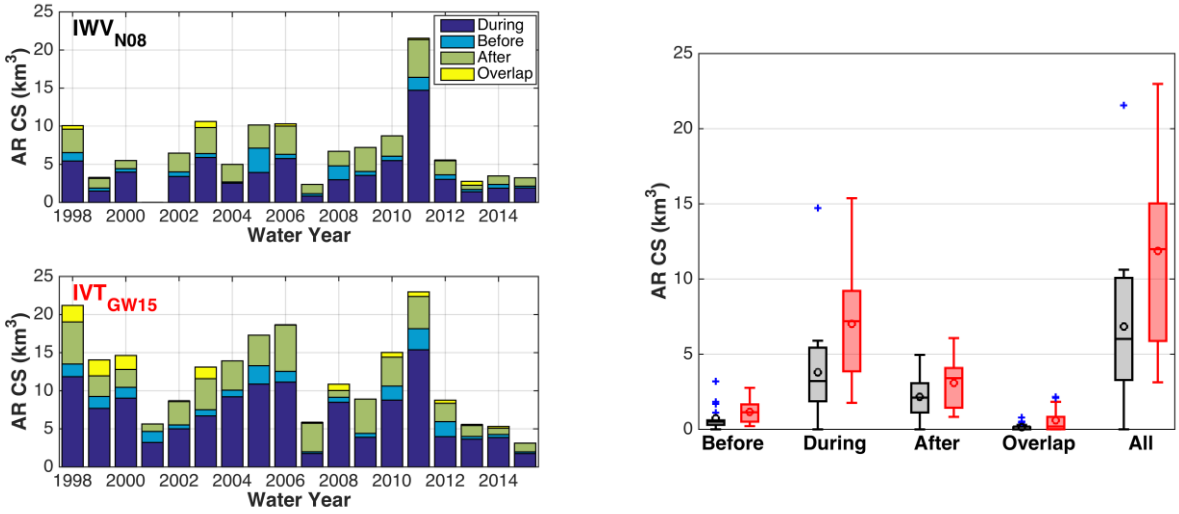

Figure B.3**.** Range-wide seasonal AR CS broken down into snowfall occurring on the day of and adjacent days of AR events as defined in Section B.3. The total length of the bars in the left panel correspond to the AR CS time series shown in Figure 4.2 (top) and (bottom), respectively. The mean and outlier seasonal AR CS values are demarcated with 'o' and '+' symbols, respectively, in the right panel. IWV_{N08} and IVT_{GW15} are colored black and red, respectively.

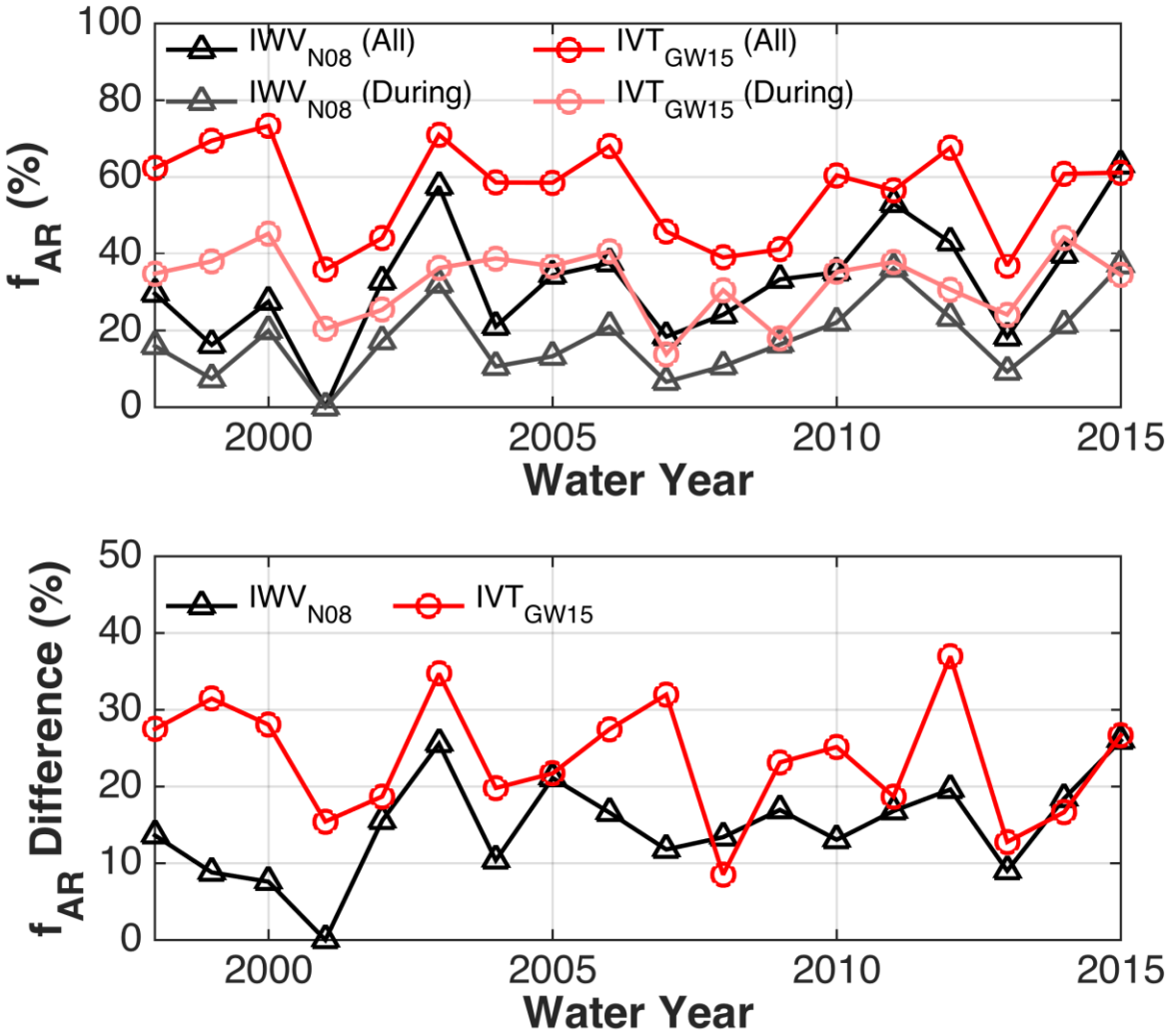

Figure B.4. (top) Comparison of the fraction of the total CS that was derived from ARs (f_{AR}) for all CS-contributing days ("all") and only the AR days ("during") for both IWV_{N08} and IVT_{GW15}. (bottom) Difference between the f_{AR} values estimated with and without the ±1 day window for IWV_{N08} and IVT_{GW15}.

B.6 Bibliography

Wilks, D. S. (2006), *Statistical methods in the atmospheric sciences*, 2nd ed., Academic Press, San Diego, CA, 627 pp.